LBL-5518
c.1

RADIATIVE DECAYS OF PSI(3684)

John Scott Whitaker
(Ph. D. thesis)

September 1976

Prepared for the U. S. Energy Research and
Development Administration under Contract W-7405-ENG-48

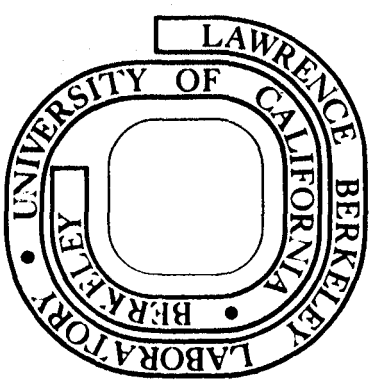

LBL-5518
c.1

DISCLAIMER

RADIATIVE DECAYS OF PSI(3684)

John Scott Whitaker

Abstract

Results of studies of radiative decays of $\psi(3684)$ are presented. The data for this work were obtained with the Magnetic Detector at the electron-positron storage ring SPEAR. These results indicate the existence of three states X, with masses 3415, 3500, and 3550 MeV, produced in radiative decays of ψ'. There is evidence for a fourth state with mass either 3340 or 3455 MeV. From study of the $\psi(3684)$ inclusive photon spectrum, the branching fraction for $\psi(3684) \rightarrow \gamma X(3415)$ has been determined to be $7.5 \pm 2.6\%$. Branching fraction upper limits of 1 - 4% at the 90% confidence level have been obtained for monochromatic photon production above 250 MeV by ψ or ψ'.

RADIATIVE DECAYS OF PSI(3684)

Contents

I. INTRODUCTION

The discovery of the narrow high-mass resonances $\psi(3095)$[1,2] and $\psi(3684)$[3] (ψ and ψ') initiated a period of great excitement and productivity in the study of particle physics. A vast multitude of theories have been proposed to explain the new particles; radiative decays of ψ' are particularly interesting because they may enable us to discriminate among theories which have predictive powers. This thesis will discuss experimental results on radiative decays of ψ' based on data obtained with the SLAC-LBL magnetic detector at SPEAR. Three lines of inquiry were pursued:

(1) a study of events $\psi' \to \gamma X$, $X \to$ charged particles, where the photon was inferred from the missing mass;

(2) a search for structure in the ψ' inclusive photon spectrum, using photons which converted in the material preceding the tracking chambers;

(3) a study of events $\psi' \to \gamma\gamma\psi$, where the ψ was detected by its lepton-pair decay and one of the photons converted.

The mesons ψ and ψ' are generally taken to be bound systems of heavy quarks with new quantum numbers -- the new quarks should be heavy to explain the high mass of ψ and ψ' and have new quantum numbers so that decay to normal hadrons is inhibited, explaining the small widths of ψ and ψ'. Inhibition of strong decays may mean that electromagnetic decays, particularly transitions to other bound states of the same quarks, may occur with appreciable branching fractions. The number of such additional states, their masses and quantum numbers, their production in ψ' decay and their possible decays (strong or electromagnetic -- possibly to $\gamma\psi$) provide stringent tests for conjectured theories.

The most detailed predictions have been made in the context of the

"standard" quark model. This model postulates the existence of three fractionally charged quarks, called u, d, and s for up, down, and strange. The u and d quarks are an isodoublet; the s quark is an isosinglet. Each quark comes in three colors, and all observed particles are color singlets. Mesons are composed of a quark-antiquark pair in this model. In particular, the vector mesons ρ and ω are taken to be the isospin-one and isospin-zero projections of the u and d quarks and antiquarks in an $L = 0$, $S = 1$ orbital, and the φ meson is the $s\bar{s}$ system. This model has been spectacularly successful in ordering particles and resonant states. It has been somewhat less successful in predicting partial widths, couplings, and other properties, and it predicts some phenomena which are not observed -- specifically, the existence of strangeness-changing neutral currents in weak interactions.

A fourth quark was added to the model to deal with some of its problems.[4] The new quark, denoted by "c," is an isosinglet with a new additive quantum number "charm." The addition of another quark implies new phenomena, such as charmed mesons, the $c\bar{q}$ pairs, and (as noted in Ref. 4) new uncharmed mesons, the $c\bar{c}$ states. Since charmed mesons have not been found in the low ($\lesssim 1$ GeV) mass range, the charmed quark is expected to be heavy. As noted by many authors, the ψ is an excellent candidate for the $c\bar{c}$ vector meson: it has the expected quantum numbers and it has the small width expected if decay to charmed mesons is below threshold (so hadronic decays are suppressed by the quark line rule).

Theoretical consideration of quark confinement suggests that due to the high mass of the charmed quark the coupling of the $c\bar{c}$ system may be moderately weak and perturbation calculations may be applicable. This leads to a picture of $c\bar{c}$ states similar to positronium, called "charmonium" by analogy.[5,6] The $c\bar{c}$ have a hydrogenic wave function --

in particular, radially and orbitally excited states may exist.[7] The ψ' is a candidate for the radially excited $c\bar{c}$ state: it has the right quantum numbers, its decays to lepton pairs indicates a nonzero wave function at the origin (which vanishes for $L \neq 0$ hydrogenic wave functions) -- and its high branching fractions for decays to ψ suggest an intimate connection.

Identifying ψ and ψ' as the $1\,^3S_1$ and $2\,^3S_1$, the charmonium model predicts the presence of more states in this mass region: a pseudoscalar state is expected near ψ and ψ', and the orbitally excited $1\,^3P_{0,1,2}$ states are expected to lie between ψ and ψ'. The 1P states will have $CP = +-$ and will not couple to e^+e^- via an intermediate photon. They can, however, be reached by electric dipole transitions from ψ' and could decay in like manner to ψ. ψ and ψ' could also decay via magnetic dipole transitions to lower-lying pseudoscalar states. Calculations of the partial widths for these various decays are uncertain, since they depend on the detailed wave functions and also may be affected by the presence of the nearby continuum.[8-11] A sketch of the predicted states showing allowed transitions is given as Fig. 1.

This discussion has been in the context of the $c\bar{c}$ assignment to ψ and ψ', but other interpretations also lead to specific predictions for radiative decays. For example, Harari has proposed[12] a six-quark model in which the P states are absent, but a pseudoscalar state near the ψ is predicted and ψ' may decay to this state with considerable rate.

Further interest in radiative decays of ψ' arises from the failure to identify significant decays of ψ' other than those including a ψ or going through an intermediate photon. The decays $\psi' \to \psi + X$ (excluding $\gamma\gamma\psi$) are $\cong 54\%$; $\psi' \to e^+e^-$ or $\mu^+\mu^-$ are $\sim 1\%$ each, and $\psi' \to \gamma \to$ hadrons is $R(\text{off resonance}) \times (\psi' \to e^+e^-) \sim 3\%$ (where R is the ratio

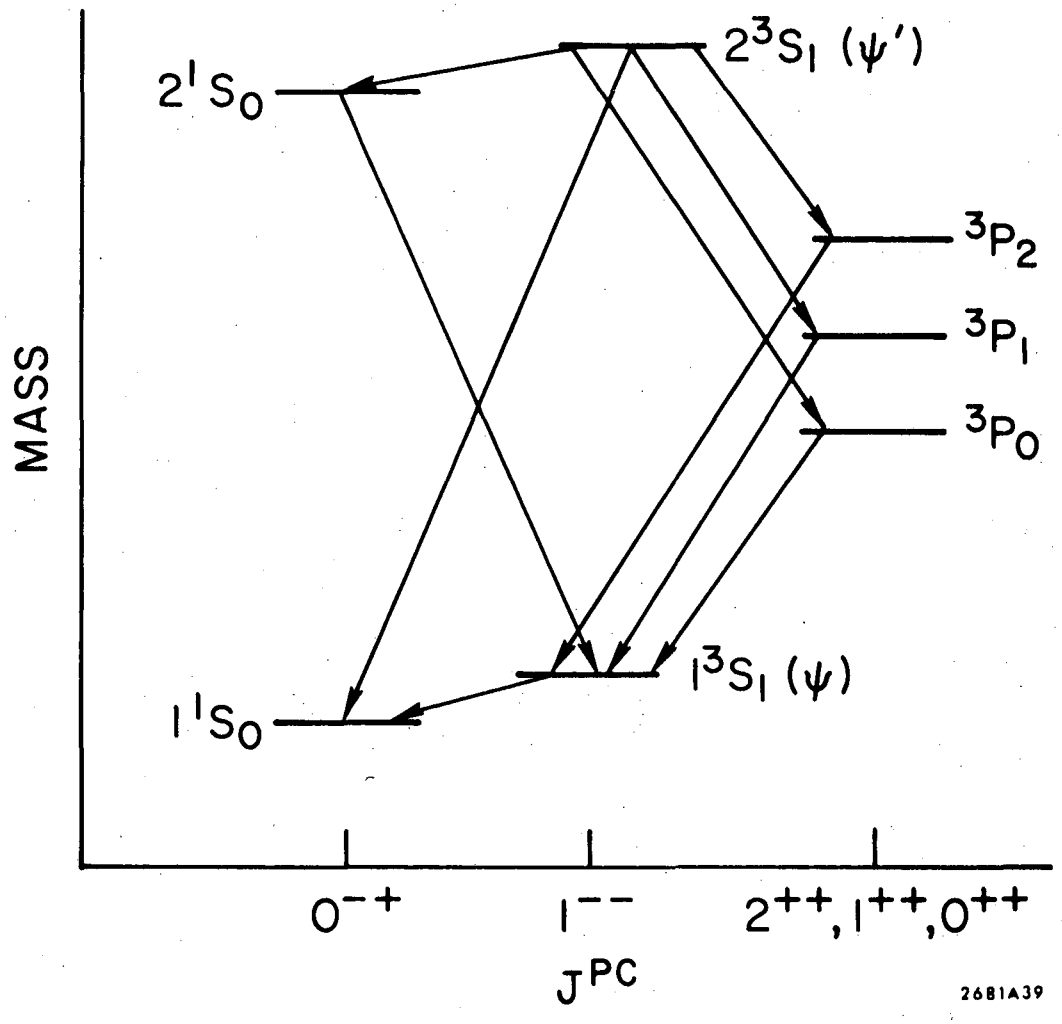

Fig. 1. Charmonium model states and transitions.

of the cross sections for hadron production and muon pair production). In the charmonium model the direct decay of ψ' to hadrons is expected to be roughly proportional to the square of the wave function at the origin and can be estimated from the results at the ψ and the relationship

$$\Gamma(\psi' \rightarrow \text{hadrons}) \cong \Gamma(\psi \rightarrow \text{hadrons}) \times \frac{\Gamma(\psi' \rightarrow e^+e^-)}{\Gamma(\psi \rightarrow e^+e^-)}$$

to be $\sim 10\%$.[13] This summation leaves unaccounted roughly 30% of ψ' decays, so there is room for large rates for radiative decays of ψ'. Problems arise, at least in the charmonium model, since P states reached by electromagnetic transitions from ψ' are expected to decay dominantly to $\gamma\psi$,[8-9] but the total rate for $\psi' \rightarrow \gamma\gamma\psi$ is only $\sim 4\%$.[14] There still remains the possibility that ψ' has radiative decays to states which decay dominantly hadronically, and, of course, non-radiative processes could account for some or all of the missing 30%.

II. THE APPARATUS

A. SPEAR

SPEAR is an electron-positron colliding beams machine, in which beams of electrons and positrons are stored and are directed to collide head-on. A plan view of SPEAR is shown in Fig. 2. Single bunches of electrons and positrons counter-rotate in a common vacuum chamber and guide field with a circulation frequency of 1.28 MHz, colliding with zero crossing angle at each of the two interaction regions each revolution. Since the laboratory frame is also the center-of-mass frame, the energy available for interactions is twice the energy of a single beam.

Particles are injected into SPEAR from the Stanford Linear Accelerator. Radio-frequency cavities provide power to the beam to make up the energy loss by synchrotron radiation and to accelerate the beams to higher energy -- acceleration to higher beam energies is accomplished simply by raising the magnetic field slowly and uniformly around the ring so the phase-stable bunches take up from the rf system the necessary additional energy.

The beams are separated electrostatically during injection and acceleration; it is also possible to take data while the beams are separated to measure background. When the separating field is turned off the bunches collide in a region of gaussian shape with rms dimensions of 5 cm along the beam line and 0.01 cm in the vertical and 0.1 cm in the horizontal transverse dimensions. Electron-positron interactions occur at a rate proportional to the cross section for the process; the proportionality factor, called the luminosity, depends on a number of factors including the current and cross-sectional area of each beam. The beam currents and luminosity decay exponentially in time; the beams are dumped and the ring is refilled when the luminosity has dropped

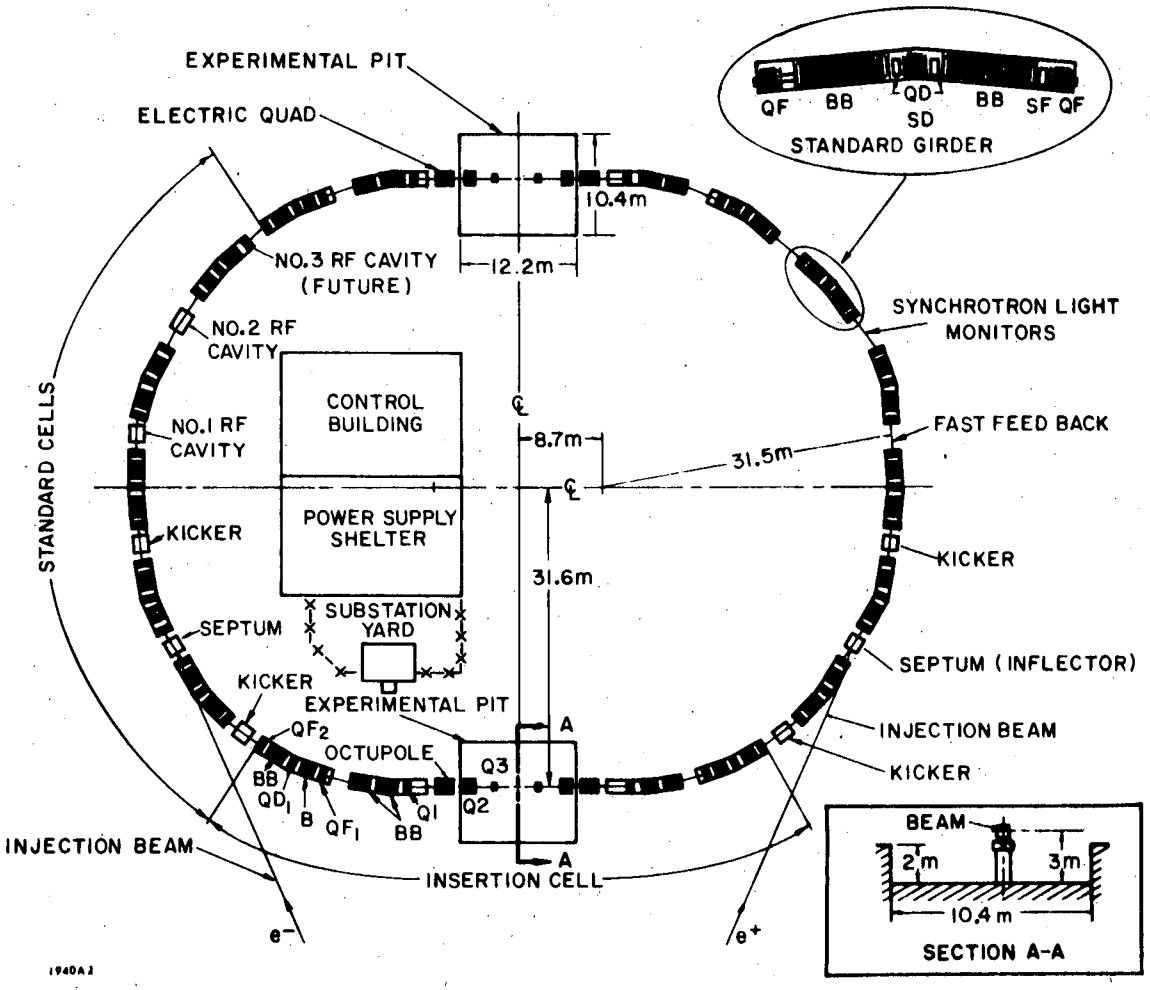

Fig. 2. Plan view of SPEAR.

below optimum. The typical integrated luminosity for a fill at ψ' is $\sim 4\ nb^{-1}$. An XDS Sigma V computer performs online control and diagnostic functions, setting magnet currents, monitoring pressures and many other critical factors.

The energy dispersion of the beams is determined by fluctuations due to synchrotron radiation; it is gaussian with rms deviation of 1.2 MeV in center-of-mass energy at energies near ψ'. This is large compared to the width of the ψ' and (along with radiative processes) determines the observed resonance shape. The error in calibration of the energy of the ring is estimated to be $\pm 0.1\%$, and the error in setting the energy is ± 0.1 MeV.

B. The Magnetic Detector

The SLAC-LBL Magnetic Detector occupies the West interaction region at SPEAR. The detector is a three-meter long, three-meter diameter cylindrical array, coaxial with the beam. It consists of plastic scintillation counters for triggering and particle identification and proportional and spark chambers for tracking charged particles; a large solenoid provides a four-kilogauss axial magnetic field for charged particle momentum determination. The counters and cylindrical spark chambers cover approximately 45° to 135° in polar angle θ with complete azimuthal acceptance. Four gaps of "end cap" spark chambers normal to the beam line on the south end of the detector provide charged particle detection from 15° to 45° in θ. Figures 3a-b show an end view and a sectioned side view of the detector. Figure 4 is a photograph of the north end of the detector with the end pieces of the iron flux return removed.

A particle emanating from the interaction region into the detector traverses in sequence:

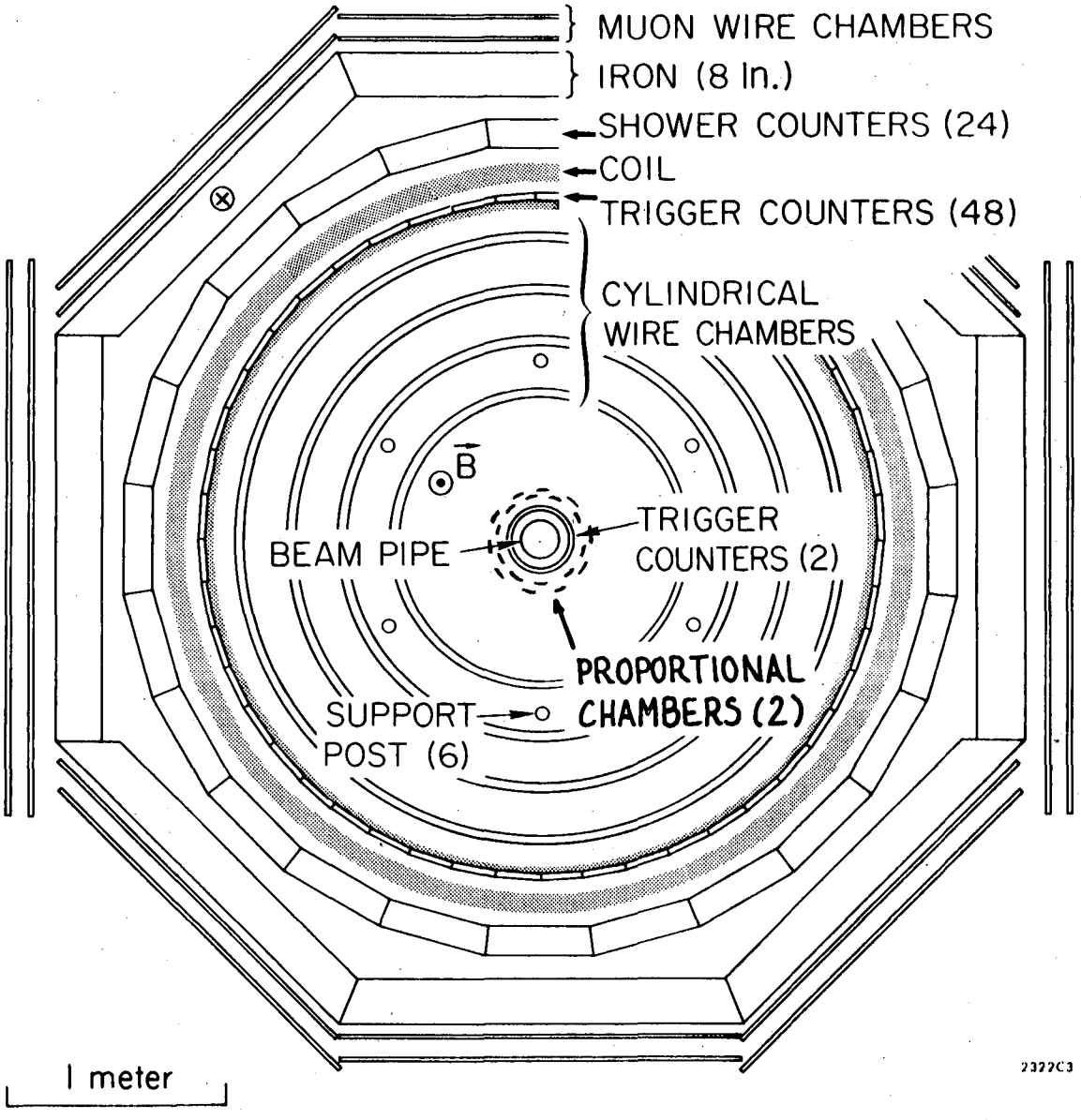

Fig. 3. (a) End view of the Magnetic Detector.

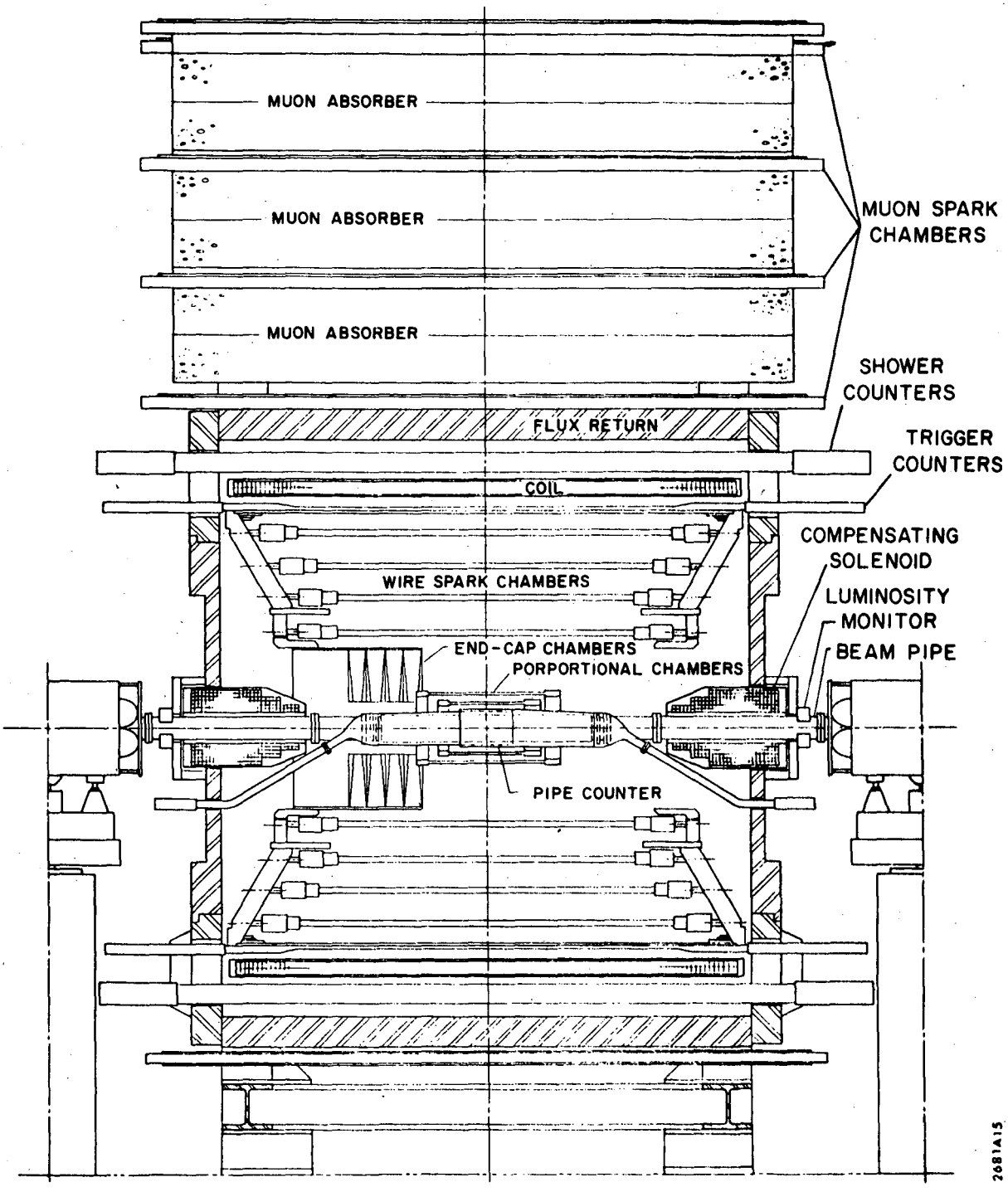

Fig. 3. (b) Sectioned side view of the Magnetic Detector.

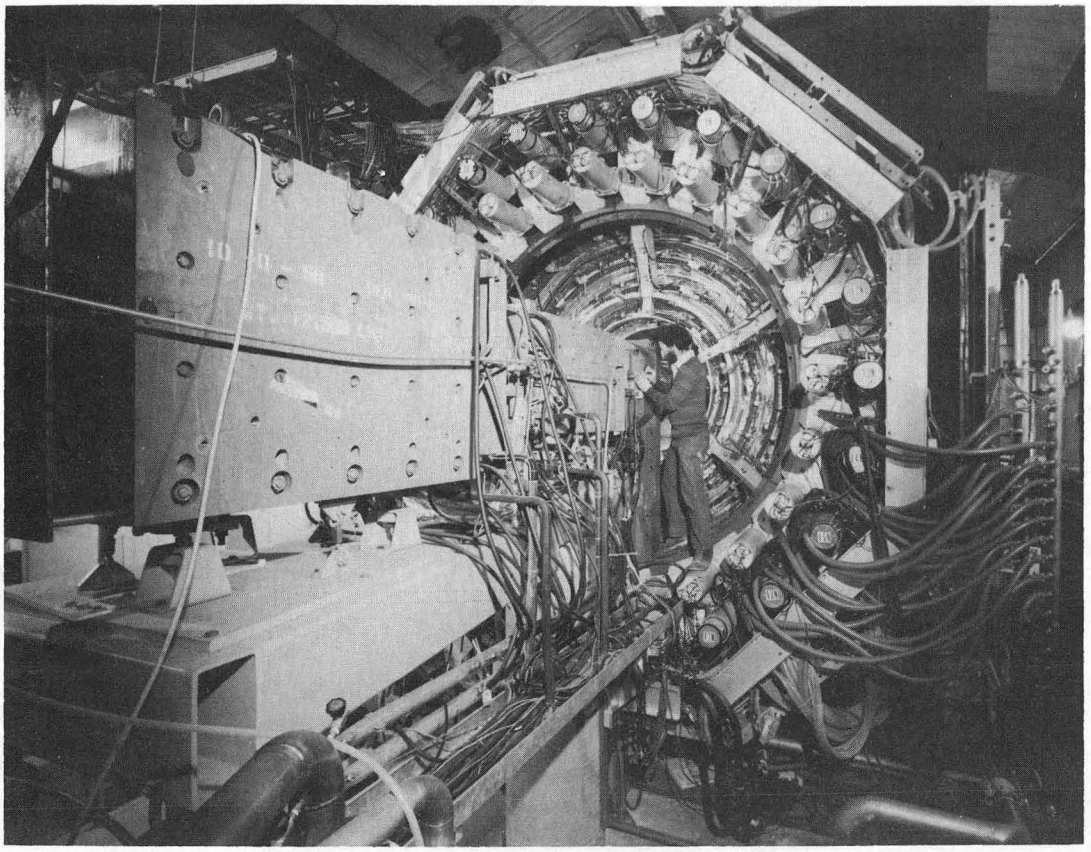

CBB 7312-7292

Fig. 4. Photograph of the North end of the Magnetic Detector with the end pieces of the flux return removed.

— the vacuum chamber -- a corrugated cylinder of 0.15 mm thick non-magnetic stainless steel at a radius of 0.08 ± 0.004 meters from the beam line. The chamber has a mean thickness, including the effect of the corrugation, of 0.152 gm/cm^2, or 0.011 radiation lengths.

— the pipe counters -- two cylindrical plastic scintillation counters each 0.69 cm thick and extending ± 18 cm along the beam line, at radii of 11 and 13 cm. Each counter is divided in the vertical plane into two hemicylinders; a 56DVP phototube views each hemicylinder from one end through a lucite light pipe. The efficiency of a single counter for detecting minimum-ionizing particles was > 95%, as measured with cosmic rays.

— the proportional chambers -- two concentric proportional chambers were installed in January 1975. The inner chamber has a radius of 17.3 cm, 0.21 cm wire spacing, and covers 34° to 146° in polar angle; the outer chamber is at 22.4 cm radius, has 0.28 cm wire spacing, and covers 29° to 151°. The chambers are each 0.0043 radiation lengths thick. Each chamber was > 90% efficient for detecting prongs in multiparticle hadronic events.

— cylindrical spark chambers -- there are four sets of cylindrical wire spark chambers at radii of 66, 91, 112, and 135 cm with active regions in polar angle of 31° - 149°, 40° - 140°, 43° - 137°, and 45° - 135°. Each set consists of two gaps, one with the wires at ± 2° with respect to the beam line and the other with the wires at ± 4°. The wires are 0.19 mm diameter aluminum with 1.1 mm spacing. A mixture of 10% helium and 90% neon is used. The chambers are read out magnetostrictively by a total of 100 wands; both the high-voltage and the ground wires are read. Each wand can record up to fifteen sparks and fiducials. The efficiency of the

chambers is generally > 90% for each wire "plane." Since the analysis requires two or more wires in the set of four to determine spark coordinates, the spark efficiency is very high. The chambers are supported by a 1.3 cm thick aluminum cylinder outside the outer chamber and by six aluminum support posts at 79 cm radius, between the first and second chambers. These posts are 6 mm thick and 5 cm in diameter, subtending ~ 7% of the azimuth. Due to the possibility of large scatters, charged particles whose trajectories pass through a post must be ignored, reducing the effective acceptance of the detector.

— trigger counters -- forty-eight plastic scintillator counters are mounted on the outside of the spark chamber support can. Each counter is 2.5 cm thick, 23 cm wide, and extends ± 130 cm along the beam line; a 56DVP phototube at each end measures the light output. The trigger counters have two functions: to provide part of the detector trigger and to measure time of flight (TOF) of particles to allow particle identification. For triggering it is desirable to have a high-threshold discrimination on the phototube output to reduce triggers on low energy background particles, but for TOF measurements a low threshold is needed to reduce time-slewing due to variations in pulse shape. To accomplish these purposes, the anode signal of each phototube is split 3:1. The larger fraction is split again in the ratio 4:1; the 4/5 part of this larger fraction is discriminated and provides the stop signal for a time-to-digital converter (TDC), and the 1/5 part is input to an analog-to-digital converter (ADC) to enable off-line corrections for slewing due to pulse height variation. The smaller fraction from the first split is discriminated and sets latches (gated flip-

flops) for triggering. Each phototube is latched and there is a "time-compensated" latch to indicate an AND of both phototubes on a counter.

The time compensation scheme is a way to reduce background triggers by minimizing the length of the gates on the latches. Cosmic rays, a principal source of background, require 10 nanoseconds to traverse the detector; hence, the trigger rate due to cosmic rays will be proportional to the length of the latch gate in excess of 10 ns. A light signal takes $\sim$ 20 ns to propagate from one end of the counter to the other, so the phototube signal from one end may vary by $\pm$ 20 ns relative to the signal from the other end. This variation is compensated by delaying the earlier signal, in the following way: the discriminated phototube signals are injected into the two ends of a string of voltage comparators, the threshold of a comparator being greater than a single discriminator pulse and less than twice that level and the number of comparators such that the signal propagates through the entire chain in 20 ns. Thus the output of the time compensator has time variation reflecting the range of velocities of the incident particles. The time compensator was latched with an 18 ns gate, permitting latching on protons down to momenta where they range out in the spark chamber support can.

— the solenoid -- the solenoid is a double wind of hollow, water-cooled aluminum conductor potted in epoxy resin between inner and outer aluminum skins; it is coaxial with the beam at 1.7 m radius. The solenoid is powered by a 2.8 megawatt supply at a nominal current of 4370 amperes; compensating coils at each end of the detector, in series with the main solenoid but wound in the opposite

sense, assure that $\int B \cdot d\ell = 0$ along the beam line through the detector -- a necessity for stable beam storage. The solenoid produces an axial four kilogauss field which is uniform to 5% in the active region of the tracking chambers; a polynomial fit accurate to 0.1% was used in the data analysis. The solenoid's thickness is roughly one radiation length.

— the shower counters -- outside the solenoid are twenty-four shower counters. A counter consists of five 0.64 cm thick (~ one radiation length) lead sheets each followed by a 0.64 cm sheet of Pilot F plastic scintillator. The counters are 48 cm wide and have active length of 3.1 meters. The lead-scintillator sandwich is contained in a box consisting of 1.3 cm thick aluminum plates front and back, bolted to 0.3 cm thick aluminum side plates. The lead contains six percent antimony to increase its stiffness. Four three-meter long lucite strips were glued to each sheet of plastic near the sides to support the lead free of the plastic and prevent crazing; however, the removal of the excess glue scratched the plastic, reducing its initial attenuation length of ~ 1.5 meters to ~ 0.8 meter. This reduced the light output and efficiency of the counters. The efficiency of the shower counters is discussed in Appendix A.

Each shower counter has a five-inch RCA 4522 phototube at each end. The phototube anode signal is split: 1/10 goes to ADC's for pulse height measurement and 9/10 goes to an adder-comparator circuit called a "mixer." The mixer adds the signals from the two phototubes of a counter and discriminates the sum, setting a latch when the threshold is exceeded. The 1/10 of the signal used for pulse height measurement is split 3:1, the 3/4 going to an ADC with 1/4 picocoulomb/channel sensitivity and the 1/4 to an ADC with one pico-

coulomb/channel sensitivity. This scheme provides the large dynamic range needed to include pulse heights from high energy electrons while resolving from pedestals the pulse heights of minimum-ionizing particles.

- the iron flux return -- the detector is surrounded by iron which acts as a flux return path and makes the magnetic field in the detector nearly uniform. The iron is 20 cm thick around the circumference of the detector and 8 to 12 cm thick on the ends.
- muon spark chambers -- large spark chambers outside the return iron detect penetrating particles. The inner detector and the return iron are 1.7 interaction lengths thick, absorbing muons with momenta < 350 MeV/c and giving $\sim 20\%$ hadronic punchthrough. More spark chambers and concrete absorbers on top of the detector provide better muon identification over $\sim 10\%$ of the solid angle, having a thickness of 5 interaction lengths total.

The luminosity of the storage ring was monitored by observing small angle e^+e^- elastic scattering, using counter telescopes at each end of the detector at $\pm$ 20 milliradians from the beam line in the vertical plane. Each of these telescopes consists of a scintillation counter to define the position of an incident charged particle and a tungsten-scintillator sandwich shower counter to identify electrons and discriminate against low energy and minimum-ionizing particles. The luminosity counter latch status and the pulse height in the shower counter were recorded with each event. Coincidences of pairs of luminosity counters collinear through the interaction region ("true" coincidences) and non-collinear ("false" coincidences) were scaled, gated by the live time of the detector, permitting calculation of the effective luminosity. This system provided the luminosity measurements for running on the ψ and ψ'

resonances; the luminosity counters were calibrated off resonance relative to large angle e^+e^- scatters in the main detector.

C. Triggering and Data Collection

The trigger system for the magnetic detector was designed to be very flexible, allowing special triggers for check out or trouble-shooting and including the ability to escalate the trigger level if backgrounds should prove severe. Figure 5 is a block diagram of the fast electronics, showing the routing of counter signals and the major elements of the trigger. It was possible to select with the twist of a dial any of a variety of triggering modes: beam events, cosmic rays, pulser, or computer control.

The normal "beam" trigger was derived from the pipe counters, trigger counters, and shower counters. A pickup upstream from the detector along one or the other beam detected the passage of the particle bunch and generated a master strobe, which was split and delayed to generate gates for the various counters. After $\sim$ 200 nanoseconds the counter latches were interrogated to see if the preset trigger conditions had been met. If not, the latches were cleared and the system was ready for the next beam passage. In the case of a valid trigger configuration, further master strobes were inhibited and the detector was triggered: spark chambers were pulsed and TDC's and ADC's started. After appropriate delay, counter and spark chamber data were bussed by CAMAC to an XDS Sigma V computer which wrote the data onto magnetic tape and analyzed a sample of the events. The system was disabled after a trigger for 0.2 - 0.3 second to allow the spark chamber charging lines to recharge and to get the data onto tape.

Our standard trigger was designed to limit the trigger rate to an

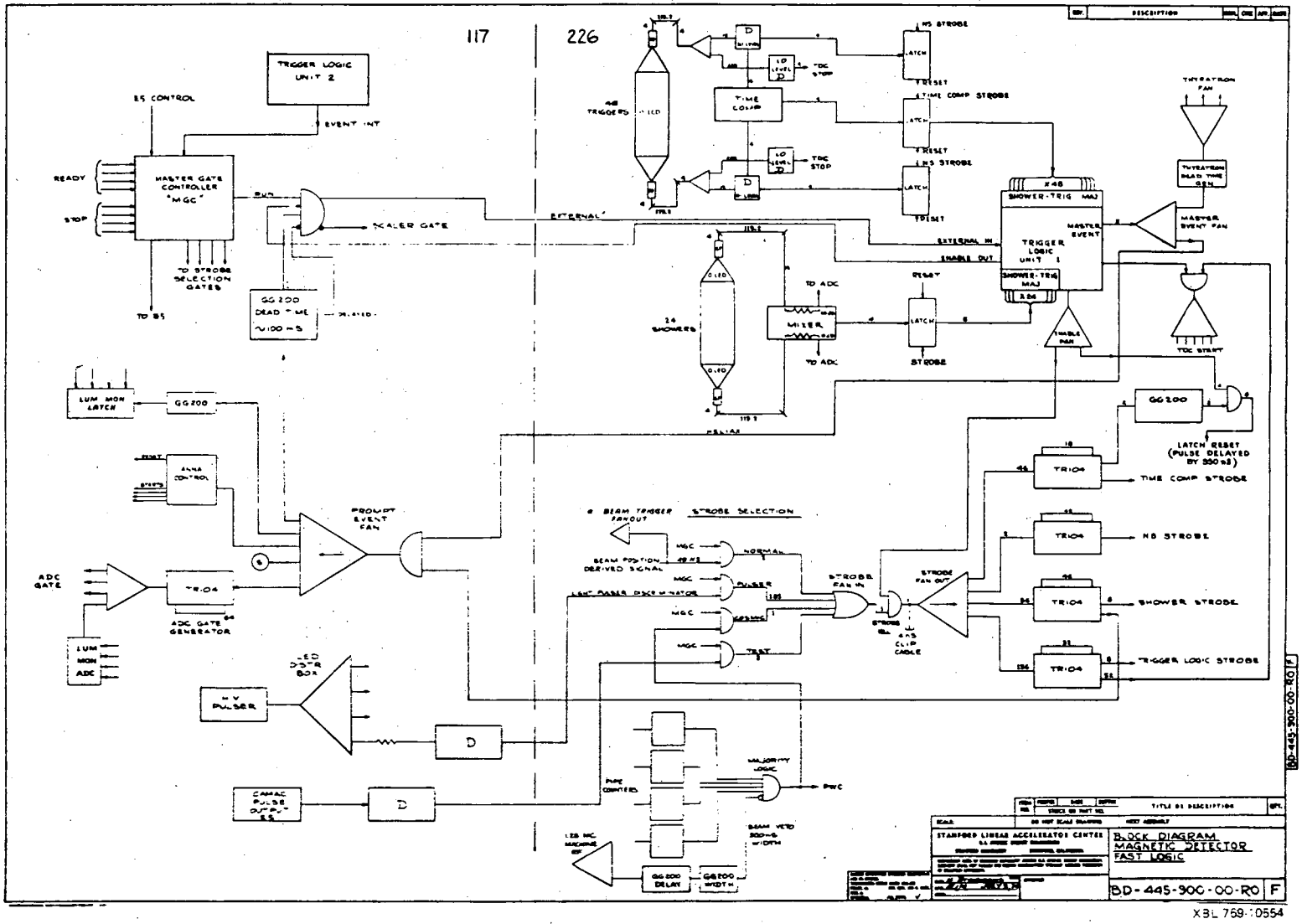

XBL 759-10554

Fig. 5. Block diagram of the fast electronics for the Magnetic Detector.

acceptable level while introducing the minimum bias into event selection. Due to ferocious background it was necessary to include the shower counters in the trigger, introducing the momentum bias discussed in Appendix A. The usual "hadron" trigger consisted of the following elements ANDed together:

*) a coincidence between the inner and outer pipe counters on the same side;

*) two TASH's, where a TASH is a trigger counter in coincidence with the radially outward shower counter or the next closest shower counter;

*) two SHAT's, where a SHAT is a shower counter in coincidence with one of the two trigger counters directly inboard or one of the next closest two trigger counters.

The distinction between two TASH's and two SHAT's is sketched below:

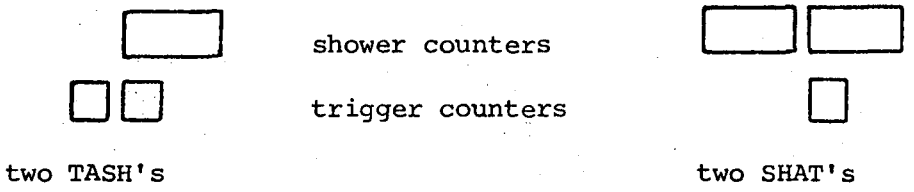

Two independent trigger counter-shower coincidences were necessary to reduce background triggers.

With this trigger the dead time of the apparatus was generally less than 10%. Some of our data were taken with a less restrictive trigger -- the 2 TASH, 2 SHAT requirement was reduced to the requirement of one TASH and an additional trigger counter latch. This trigger increased considerably the efficiency for events consisting of all low momentum particles, such as $\psi' \to \pi^+\pi^-\psi$ events where the ψ is unseen, but had little effect on the efficiency for events with photon conversions.

III. ANALYSIS

Off-line analysis of the data was done in two passes. In the first pass, time-of-flight system parameters and the beam positions in the interaction region were measured. Pass II used these quantities in performing the full event reconstruction, writing an output tape containing both the raw data and the information from the reconstruction. Event reconstruction consisted of: identification and measurement of charged particle tracks, processing of trigger counter time-of-flight data and of the shower counter pulse-heights, searching the muon spark chambers for evidence of the presence of muons, and event classification. Two types of events were omitted from this "Pass II" tape: cosmic ray events clearly identified as two-prong events with the appropriate timing difference and colinearity to be a single particle traversing the entire detector, and "junk" events with too few spark chamber points and no detected tracks, for which further analysis would be pointless. Of the initial sample of ψ' events, $\sim 50\%$ were eliminated as junk and $\sim 10\%$ as cosmics.

The details of point and track recognition in the cylindrical spark chambers have been discussed in the theses of Bob Hollebeek[15] and John Zipse.[16] Briefly, space points were defined by the crossing of struck wires in two or more of the four "planes" in a chamber. If all four planes were efficient, two points would be found in a single chamber. Starting from the outer two chambers, two points were selected from two different chambers and used to define, along with the origin, a candidate track helix (assuming a uniform magnetic field). Further points falling near the candidate track within tolerances in the r-φ and z projections were added to the list of possible points. Tracks were then required to have three or more points to merit further consideration. A least-

squares fit of a helix, again in the uniform field approximation, to the point coordinates produced first approximation values of the momentum, direction, and position of the track. The algorithm included the possibility of dropping points which made inordinate contributions to the χ^2 of the track. Points in the inner chamber only were allowed to be used in more than one track, to avoid a bias against photon conversions or particle decays which might give two nearby signals in the inner chamber but should separate before traversing the other chambers.

The redundancy of wire planes and chambers led to very high tracking efficiency. The wire plane spark efficiency was monitored on-line and was generally $\gtrsim 90\%$. From extensive scanning of reconstructed events, and from studying the losses imposed by requiring three or four wire crossings in a chamber in order to define a space point, the tracking efficiency is believed to be $> 97\%$. The six internal support posts for the spark chamber package were a major source of track losses: a particle striking a post could scatter through a sufficiently large angle that it no longer appeared to come from the origin and the inner points would lie outside the tolerance for distance from the helix defined by two outer points and the origin. Tracks striking a post might still be found by the tracking routines but have grossly mismeasured momentum due to the scattering.

The proportional chambers, added to the detector in January 1975, were incorporated into the track-finding algorithm in two ways. For tracks with three or more cylindrical chamber points, the track parameters determined from the points were used to predict the position of intersection of the track with each of the proportional chambers. In each chamber the point closest to the extrapolated position, if there was such a point within $\sim$ 1 cm, was added to the point list and the

track was refitted. Only the proximity in the transverse (r-φ) plane was used; the resolution and efficiency of the cathode strips designed to provide z information were too poor to be useful.

The proportional chambers were also used to find tracks which had not been found by the algorithm discussed earlier. After finding tracks with three or more cylindrical spark chamber points, the program had a list of track candidates, called "two-point tracks," which had been determined by the origin and two cylindrical chamber points but for which no other cylindrical chamber points had been found. To reduce both computing time and the number of spurious tracks, this list was cut to those two-point tracks having a point in each of the two inner spark chambers. The parameters of these track candidates were then recomputed assuming the two points were produced by a particle from a photon conversion in the pipe counters. Specifically, the track parameters were calculated assuming the two points lay on a helical path which was perpendicular in the transverse projection to a cylinder of radius 11.7 cm (the mean pipe counter radius). This peculiar algorithm was designed to make the best possible guess for tracks which were part of a photon conversion pair while retaining high efficiency for finding tracks which came from the origin and were not part of a conversion pair. As before, the point, if any, nearest to the predicted intersection in each chamber and within tolerance was assigned to the track and the track was then fit in the usual manner. The difference between the predictions of this algorithm and the algorithm including the origin as a point to define the helix was at most half the tolerance on the deviation of the proportional chamber point from its expected position, so tracks truly emanating from the origin were still found with high efficiency. Photon conversions, however, produce pairs of tracks which are nearly collinear with

the (radial) photon direction and which have separated by $\lesssim 1$ centimeter when they intersect the proportional chambers. The original algorithm tended to systematically associate the wrong proportional chamber point with the track, that is, it tended to assign to the positron the proportional chamber point caused by the electron and vice-versa. This would worsen the momentum resolution for these tracks and would open up the angle between them, broadening the effective mass distribution for conversion pairs including one or two two-point tracks.

Figure 6 is a scatterplot of momentum versus $\cos\theta$ for two-point tracks from ψ' events. As expected for $|\cos\theta| \lesssim 0.6$, most of the two-point tracks have momenta too low to reach three cylindrical chambers: there is a cutoff of ~ 75 MeV/c transverse momentum for reaching three cylindrical chambers, and 55 MeV/c for reaching two chambers. Two-point tracks in this small $|\cos\theta|$ region with larger momenta may have missed having more cylindrical chamber points due to inefficiencies or may be accidental combinations of background points. The high momentum tracks near $\cos\theta \sim \pm 0.7$ are due to a gap of $\Delta \cos\theta = 0.03$ where particles could pass through the inner two cylindrical chambers and miss the outer two. The population of low momentum tracks at small $\cos\theta$ relative to the population of higher momentum tracks at large $\cos\theta$ is in good agreement with Monte-Carlo simulation of the detector acceptance folded on ψ' decays.

Three types of fits were made to the points on a track: the CIRCLE fit, which assumes a uniform magnetic field; the ONETRK fit, which used a polynomial map of the magnetic field; and the BC (beam-constrained) fit, which used the field map and added the measured beam position in the transverse plane as a point to which the track was constrained. Every track had a CIRCLE fit, since that was how the track was found.

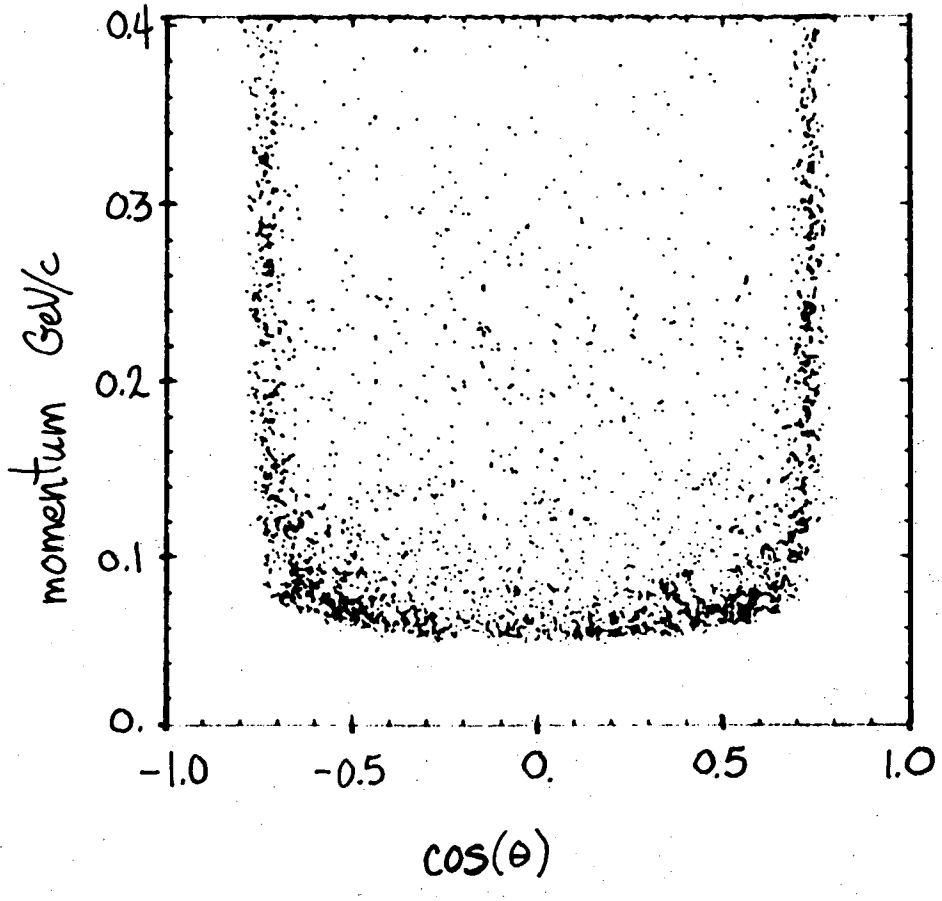

XBL 769-10485

Fig. 6. Momentum versus cos (θ) for "two-point" tracks.

The ONETRK and BC fits are χ^2 minimizations of the deviations of the fit track positions from the observed coordinates, using a modified version of the program CIRCE.[17] This algorithm did not have the ability to drop points which were causing the χ^2 to be out of bounds, and so some fraction of the tracks were missing the BC or ONETRK fits due to the failure of the fitting algorithm to converge. Two-point tracks were omitted from the BC fit. The ONETRK fit failed for 1.4% of $\geq$ 3-point tracks and 7% of two-point tracks; virtually all of these were near a momentum where the track intersected a chamber nearly tangentially, so that if the starting value of the momentum was too low, the fitted track would not reach the outermost point and the fit would fail.

The momentum resolution depended on the number and type of points on the track. The spatial resolution of points in the cylindrical spark chambers was 0.5 mm in the r-φ direction and 1.4 cm or 0.7 cm in the z direction for 2° or 4° stereo gaps respectively. The points were fixed radially at the center of the spark gap. The r-φ resolution of the proportional chamber was $\sim$ 0.7 mm; the porportional chambers had no z resolution. The transverse position of the interaction region was measured in Pass I from Bhabha events with a precision of $\sim \pm$ 0.1 mm in x and in y. Due to the small uncertainty in the beam position, the proportional chamber points were relatively unimportant to the BC resolution. However, it was necessary to include the effect of multiple scattering in the vacuum pipe, pipe counters, and proportional chambers in the BC fit. In the course of fitting the track, the uncertainty in the fitted momentum was calculated from the known spatial resolution of the tracking chambers and the observed deviations of track points from the fitted track. The relationship of this calculated momentum error to the track momentum resolution was studied using the track momentum pulls

from kinematic fitting, where a momentum pull is the ratio of the change in track momentum divided by the track's momentum error. The momentum pulls from fitting $\psi' \to 4\pi^{\pm}$ and $\psi' \to \psi\pi^{+}\pi^{-}$, $\psi \to e^{+}e^{-}$ or $\mu^{+}\mu^{-}$ were normally distributed with unit rms deviation, indicating the momentum resolution was well represented by the calculated momentum error. The BC fit was further improved by tweaking the track angles and momenta by empirical amounts determined from study of Bhabha event momenta and angles correlated with θ and φ, correcting for slight errors in the beam position and chamber constants. After these corrections the BC momentum resolution is well represented by $dp \cong \{(1.6p\%)^2 + (0.6\%)^2\}^{1/2}$.

The resolution of the ONETRK fit was poorer than the BC fit since the beam position, a point with small error at the end of long arc length, was not used. The ONETRK fit was therefore more sensitive to the number of points on the track. Figure 7 shows the ONETRK momentum resolution as a function of momentum. The tracks used for Fig. 7 were positrons and electrons, selected as part of a conversion pair; the electron mass was used in calculating the multiple scattering error. The error bars in Fig. 7 are the rms deviation from the mean momentum uncertainty in that momentum bin, indicating the spread of the momentum uncertainty distribution. The data in Fig. 7 show that the momentum resolution is poorer and has a greater variation for low momentum tracks than for higher momentum tracks, as expected due to the fewer number of points on low momentum tracks. The two-point tracks suffer an additional deterioration of resolution since the dip of the tracks is determined only by the two cylindrical spark chamber points.

The ONETRK fitting was preceded by a vertex fit, which did a constrained fit for all tracks within 15 cm of the beam line and 40 cm z extent, assuming a common origin. This fit gave the vertex position

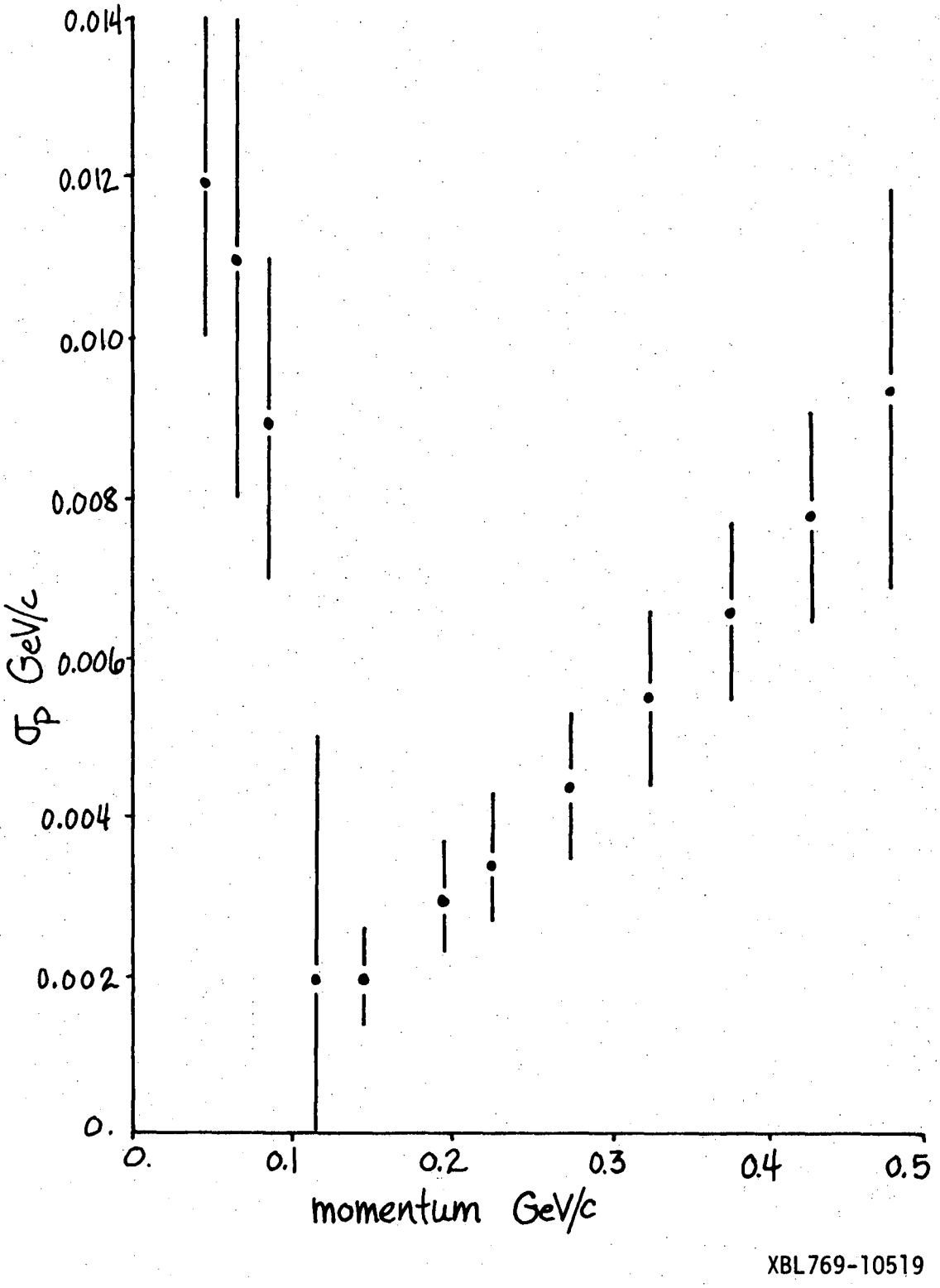

Fig. 7. Charged particle momentum resolution from the ONETRK fit.

for later discrimination against beam-gas events or background events due to particle interactions in the vacuum pipe or other material.

To achieve the best possible time-of-flight resolution, the start-time offset due to beam current dependence of the pickup signal was measured at Pass I using Bhabha events and was applied at Pass II. Corrections to the TOF were also made for slewing due to pulse-height variations. After these corrections, the rms TOF resolution was 0.4 ns.

The shower counter pulse-height data were corrected for counter gain and attenuation losses using the track information for charged particles and z as determined from the logarithm of the ratio of the pulse heights from the two ends of the counter in the case of neutral shower counter hits. Due to the thickness of the radiator and the infrequent sampling, the energy resolution of the shower counters was very poor -- the rms resolution was $\sim 30\%$ for electrons from ψ decay and $\sim 45\%$ for muons from ψ decay.

The purpose of event classification was to separate QED and hadronic events from background events due to cosmic rays or to accidental interactions of beam particles with the residual gas or with the vacuum pipe. The large cross sections of ψ and ψ' largely obviated this step, other than the filtering already discussed. Background events were negligible; the population of other background event classes was consistent with losses of $\sim 10\%$ from ψ or ψ' events as expected on the basis of our studies of nonresonant data.[18]

IV. STATES OBSERVED BY HADRONIC DECAYS

This Chapter will discuss the observation of new states by the detection of their decays to charged particles. A previously published paper[19] has established the existence of new states in a number of hadronic channels and has demonstrated that these states are produced in radiative decays of ψ'; consequently, this work will dwell on new results on the number of these states, their masses, and their decay modes. Much of this Chapter has been excerpted from the work of George Trilling and Dave Johnson.[20]

The data sample for this study consisted of events with 2, 4, or 6 charged prongs with total charge zero, taken from an initial sample of $\sim$ 350,000 ψ' events. Events were required to have all tracks consistent with a common vertex near the beam interaction region; the beam-constrained fits to the tracks, improved by empirical corrections, were used. All events used in the analysis satisfied one-constraint fits, applied using the bubble-chamber kinematic fitting program SQUAW, to ψ' radiative decay and subsequent hadronic decay.

New states χ produced in radiative decays of ψ', $\psi' \rightarrow \chi + \gamma$, decay via a variety of hadronic channels; e.g.,

$$\chi \rightarrow \pi^+\pi^-\pi^+\pi^-$$

$$\chi \rightarrow \pi^+\pi^- K^+K^-$$

$$\chi \rightarrow \pi^+\pi^-\pi^+\pi^-\pi^+\pi^-$$

$$\chi \rightarrow \pi^+\pi^- \quad \text{or} \quad K^+K^- \quad .$$

The radiative decay is established by a study of the missing mass against the observed charged particles. Figure 8, taken from Ref. 19, shows the missing-mass-squared M_x^2 for four-prong events from ψ and ψ'; Figs. 8a and 8b show M_x^2 for ψ' and ψ events with missing momentum p_x in the range 0.1 - 0.3 GeV/c, and Fig. 8c shows M_x^2 for ψ' events with $p_x > 0.3$ GeV/c.

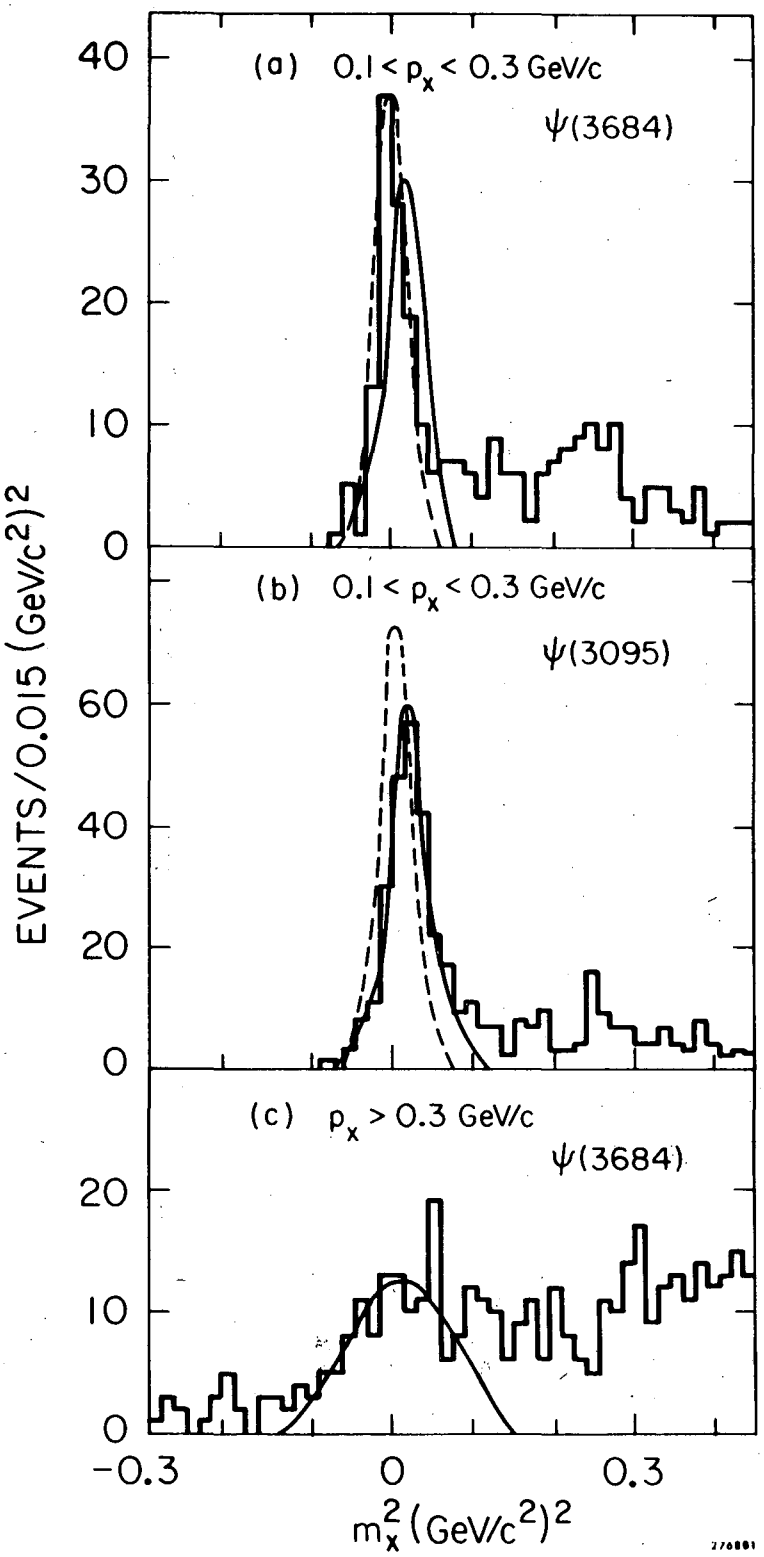

Fig. 8. Missing-mass-squared M_x^2 for 4-prong events from ψ and ψ': (a) M_x^2 for ψ' events with $0.1 < p_x < 0.3$ GeV/c; (b) M_x^2 for ψ events with $0.1 < p_x < 0.3$ GeV/c; (c) M_x^2 for ψ' events with $p_x > 0.3$ GeV/c.

The solid and dashed lines show the predictions for a missing π^0 and a missing photon, respectively. For $0.1 < p_x < 0.3$ GeV/c, the M_x^2 distribution for ψ is consistent with a missing π^0, while the ψ' distribution shows a dominant fraction of the events having a missing photon. For $p_x > 0.3$ GeV/c, the ψ' distribution is consistent with a missing π^0.

Cuts used to isolate the various decay modes and remove background were as follows:

(a) $\underline{\pi^+\pi^-\pi^+\pi^-}$

(i) $|(\text{Missing Mass})^2| \leq 0.05\ (\text{GeV}/c^2)^2$,

(ii) (Missing Energy - Missing Momentum) ≤ 0.1 GeV/c -- to avoid confusion with $\chi \to \pi^+\pi^-K^+K^-$,

(iii) (Missing Mass recoiling against any $\pi^+\pi^-$) ≤ 3.05 GeV/c^2 -- to remove contamination from $\pi^+\pi^-\psi$ and $\eta\psi$ decays followed by $\psi \to e^+e^-$ or $\mu^+\mu^-$ decays.

(b) $\underline{\pi^+\pi^-K^+K^-}$

(i) $|(\text{Missing Mass})^2| \leq 0.05\ (\text{GeV}/c^2)^2$,

(ii) (Missing Energy (calculated as if all tracks are pions) - Missing Momentum) > 0.1 GeV/c -- to avoid confusion with $\chi \to \pi^+\pi^-\pi^+\pi^-$,

(iii) Same as (iii) for $\pi^+\pi^-\pi^+\pi^-$,

(iv) $\chi^2_{TOF}(\pi^+\pi^-K^+K^-) < \chi^2_{TOF}(\pi^+\pi^-\pi^+\pi^-)$ where χ^2_{TOF} is the test of goodness of fit of measured times of flight to the predicted ones.

(c) $\underline{\pi^+\pi^+\pi^+\pi^-\pi^+\pi^-}$

(i) $|(\text{Missing Mass})^2| \leq 0.05\ (\text{GeV}/c^2)^2$,

(ii) Same as (ii) for $\pi^+\pi^-\pi^+\pi^-$,

(iii) (Missing Mass recoiling against any $\pi^+\pi^-$) outside the range 3.05 - 3.20 GeV/c^2 -- to remove $\pi^+\pi^-\psi$ contamination.

(d) $\underline{\pi^+\pi^- \text{ or } K^+K^-}$

(i) Cuts to remove muons and electrons are applied,

(ii) (Azimuthal Angle between the two track momentum vectors) $> 160^{o}$,

(iii) Both momenta > 1000 MeV/c,

(iv) (Missing Momentum transverse to the average $\pi^{+}\pi^{-}$ line or $K^{+}K^{-}$ line) $\geq$ 50 MeV/c -- to remove radiative $e^{+}e^{-}$ and $\mu^{+}\mu^{-}$ decays not already cut out by (i),

(v) Effective mass of two charged particles when treated as $\pi^{+}\pi^{-}$ lies outside the range 3020 - 3190 MeV -- to remove residual $\psi \rightarrow \mu^{+}\mu^{-}$ or $e^{+}e^{-}$ not cut out by (i). Cuts (ii), (iii) here do not remove events of interest but help to cut down background.

The fitted mass spectra corresponding to the decay modes above are shown in Fig. 9. The 4π and $2\pi 2K$ spectra show clear evidence for three X peaks at masses of 3415, 3500 and 3550 MeV/c^2 plus a higher mass peak corresponding to the decay $\psi' \rightarrow 4\pi$ or $\pi\pi KK$. Except for the fortuitously narrow $\pi^{+}\pi^{-}K^{+}K^{-}$ spike near 3.50 GeV/c^2, the observed widths are all about the same and consistent with the experimental resolution. The interpretation of the populations above 3.45 GeV/c^2 in terms of <u>two</u> distinct intermediate states is further supported by the detection of the same states in cascade decay modes,

$$\psi' \rightarrow \gamma X \rightarrow \gamma\gamma\psi$$

(see Chapter VI). As can be seen in the 3415 MeV state, the 6π data appear to have slightly worse resolution than the 4π and $\pi\pi KK$ data, and the two upper states are not resolved. The near uniform population from 3.48 to 3.57 GeV/c^2 suggests however that comparable amounts of the 3500 and 3550 MeV/c^2 states are present.

For the $\pi^{+}\pi^{-}$ and $K^{+}K^{-}$ data, a separation between the two hypotheses has been made on the basis of lowest χ^2 in the kinematic fit. The data confirm the previous result of a very strong 3415 MeV signal, and also show a considerably weaker signal at 3550 MeV. The two events around

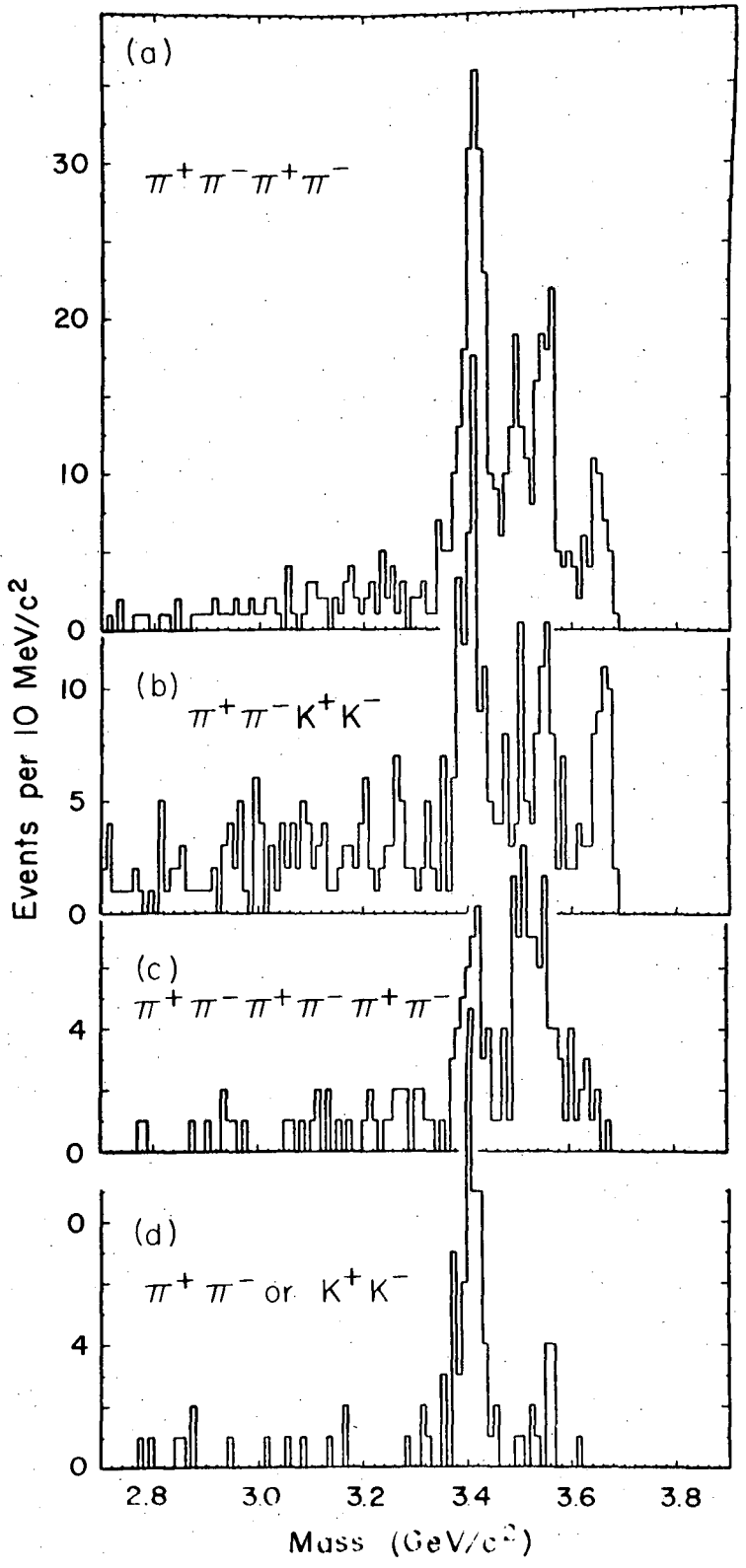

Fig. 9. Mass spectra for (a) $\pi^+\pi^-\pi^+\pi^-$, (b) $\pi^+\pi^-K^+K^-$, (c) $\pi^+\pi^-\pi^+\pi^-\pi^+\pi^-$, (d) $\pi^+\pi^-$ or K^+K^-.

3500 MeV may just arise from the tail of the 3550 MeV population, and there is no compelling evidence for a signal at 3500 MeV. Thus this distribution is consistent with the possible interpretation of the three states as the 0^{++}, 1^{++} and 2^{++} levels expected from the charmed quark model.

Branching ratio products $B(\psi' \to \chi\gamma)B(\chi \to \text{hadrons})$ were determined for the various states, normalizing the data of Fig. 9 to well known ψ' decay modes of the same topology, namely $\psi' \to \mu^+\mu^-$ for $\pi^+\pi^-$ or K^+K^-, $\psi' \to \pi^+\pi^-\psi \to \pi^+\pi^-\mu^+\mu^-$, $\pi^+\pi^-e^+e^-$ for 4π and $2\pi 2K$ and $\psi' \to \pi^+\pi^-\psi \to \pi^+\pi^-\pi^+\pi^-\pi^+\pi^-$, $\pi^+\pi^-\pi^+\pi^-\pi^+\pi^-\pi^0$ for 6π. Corrections have been made for geometrical and trigger efficiency (assuming phase space χ decays), losses in time-of-flight identification, decay in flight of $K^\pm$ mesons, and the various cuts discussed earlier (which actually reduce the signal very little but do remove much of the background). The results are given in Table I; the quoted errors reflect both statistical and systematic uncertainties. For completeness, we have also included the modes $\psi' \to \pi^+\pi^-\pi^+\pi^-$ and $\psi' \to \pi^+\pi^-K^+K^-$ for which the quoted number is just the ψ' decay branching ratio.

The 4π and $\pi\pi KK$ branching ratio products are nearly equal for the three χ states. For the direct $\psi' \to 4\pi$, $\pi\pi KK$ decays, the $\pi\pi KK$ decay mode has a substantially higher branching ratio as might be expected since the 4π decay violates G parity conservation and only goes via a "second-order" electromagnetic decay. Indeed the given 4π branching ratio (which must really be considered as the ratio of the total number of 4π events, arising either from the ψ' or from nonresonant hadron production, to the total number of hadronic decays of the ψ') is in good agreement with the expectations from a pure second-order electromagnetic process.

Table I

State	Decay mode	$BR(\psi' \to \gamma X) \times BR(X \text{ decay})$
$X(3415)$	$\pi^+\pi^-\pi^+\pi^-$	$(3.2 \pm 0.6) \times 10^{-3}$
	$\pi^+\pi^- K^+K^-$	$(2.7 \pm 0.7) \times 10^{-3}$
	$\pi^+\pi^-\pi^+\pi^-\pi^+\pi^-$	$(1.4 \pm 0.5) \times 10^{-3}$
	$\pi^+\pi^-$	$(0.7 \pm 0.2) \times 10^{-3}$
	K^+K^-	$(0.7 \pm 0.2) \times 10^{-3}$
$X(3500)$	$\pi^+\pi^-\pi^+\pi^-$	$(1.1 \pm 0.4) \times 10^{-3}$
	$\pi^+\pi^- K^+K^-$	$(0.6 \pm 0.3) \times 10^{-3}$
	$\pi^+\pi^-$ and K^+K^-	$< (0.15 \times 10^{-3})$
$X(3500) + X(3550)$	$\pi^+\pi^-\pi^+\pi^-\pi^+\pi^-$	$(2.5 \pm 0.8) \times 10^{-3}$
$X(3550)$	$\pi^+\pi^-\pi^+\pi^-$	$(1.6 \pm 0.4) \times 10^{-3}$
	$\pi^+\pi^- K^+K^-$	$(1.4 \pm 0.4) \times 10^{-3}$
	$\pi^+\pi^-$ and K^+K^-	$(0.23 \pm 0.12) \times 10^{-3}$
$\psi(3685)$	$\pi^+\pi^-\pi^+\pi^-$	$(0.8 \pm 0.2) \times 10^{-3}$*
	$\pi^+\pi^- K^+K^-$	$(1.4 \pm 0.4) \times 10^{-3}$**

* $BR(\psi' \to 4\pi)$

** $BR(\psi' \to 2\pi 2K)$

Information on the spin of the X states may be obtained from the angular distributions of the photon relative to the incident beam line. These distributions are shown in Fig. 10. For spin zero, this distribution is predicted to be $1 + \cos^2 \theta$, whereas for higher spins the predictions are not unique. Fitting the distributions to $1 + a \cos^2 \theta$, the coefficient a has the value 1.4 ± 0.4, 0.26 ± 0.5, and 0.22 ± 0.4 for the X(3415), X(3500), and X(3550) respectively. Clearly the X(3415) is consistent with expectations from spin zero. The other distributions are consistent with isotropy, but the statistical errors are too large to draw any very useful conclusion.

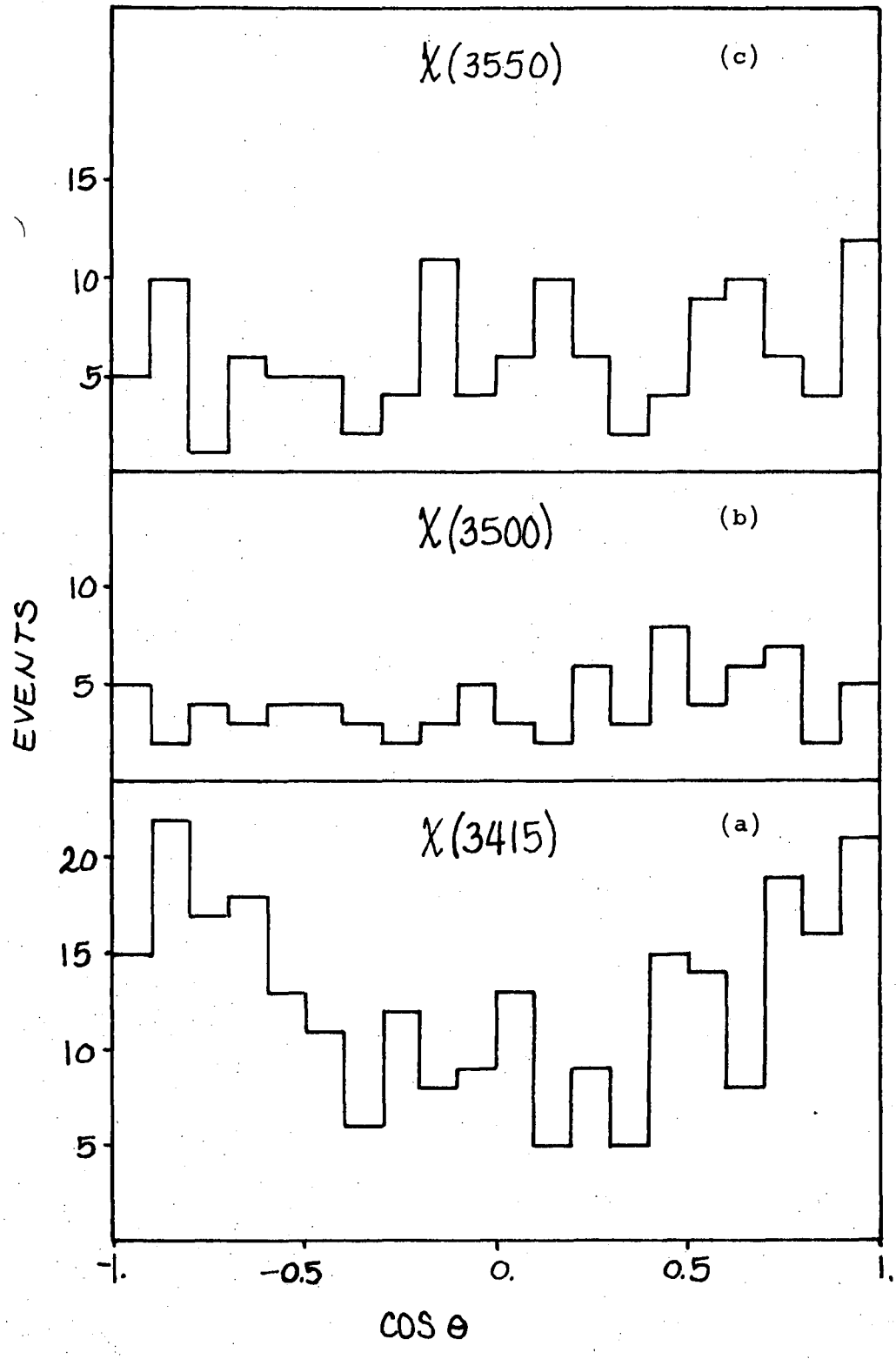

XBL769-10520

Fig. 10. Distribution of cos θ_γ for (a) $\chi(3415) \rightarrow 4\pi, \pi\pi KK$. (b) $\chi(3500) \rightarrow 4\pi, \pi\pi KK$. (c) $\chi(3550) \rightarrow 4\pi, \pi\pi KK$.

V. INCLUSIVE PHOTON SPECTRA

By studying the inclusive photon spectra of ψ and ψ' we may observe directly the existence of radiative decays to new even-charge-conjugation states without relying on the decays of such states to only charged particles. The inclusive photon spectra enable us to measure the total branching fraction for a radiative decay, rather than the product of the branching fraction for the radiative decay to some state multiplied by the branching fraction for the decay of that state to some particular channel. Since such a large fraction of ψ' decays include a ψ, it is necessary to study the inclusive spectra of both ψ and ψ' to associate any structure in the spectra with the correct parent.

A. Photon Detection

Photons are detected by their conversion to electron-positron pairs in material near the beam line. The material effective as a converter is sketched in Fig. 11; it includes the vacuum pipe, the pipe counters, and the proportional wire chambers, a total of 0.052 radiation lengths of material located 8 to 22 cm from the beam line. The composition of this material is 0.15 gm/cm^2 iron, 1.54 gm/cm^2 carbon, 0.13 gm/cm^2 hydrogen, 0.02 gm/cm^2 oxygen, and 0.06 gm/cm^2 aluminum.

Figure 12 shows the conversion probability as a function of photon energy for photons normally incident on the effective converter, compiled from Hubbell's calculations[21] of photon conversions in various materials. The conversion probability is 0.030 at $E_\gamma = 0.2$ GeV and rises to 0.039 at 2 GeV. Hubbell's calculation includes pair production from interaction with the atomic electrons, which for carbon contribute 12 to 18% of the total conversion probability. Wheeler and Lamb have determined[22] that the momentum transfers for conversions on atomic electrons are

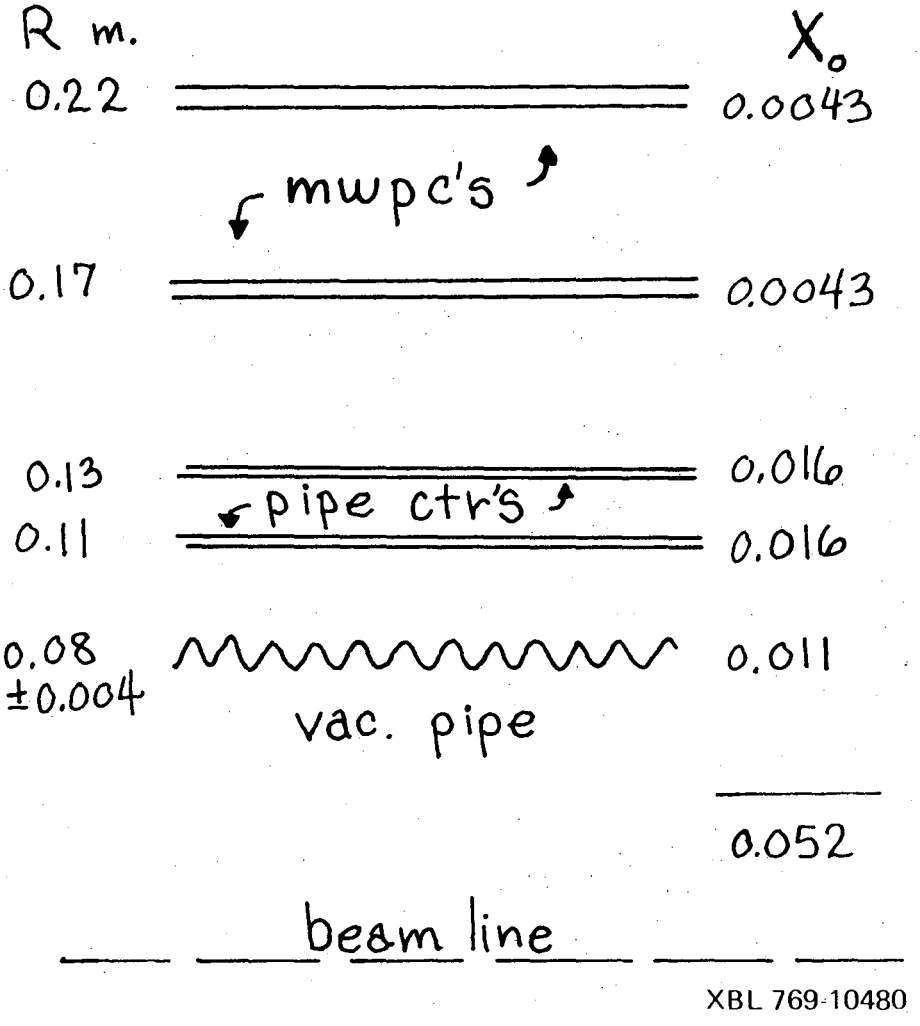

Fig. 11. The effective converter, with thickness and distance from beam line.

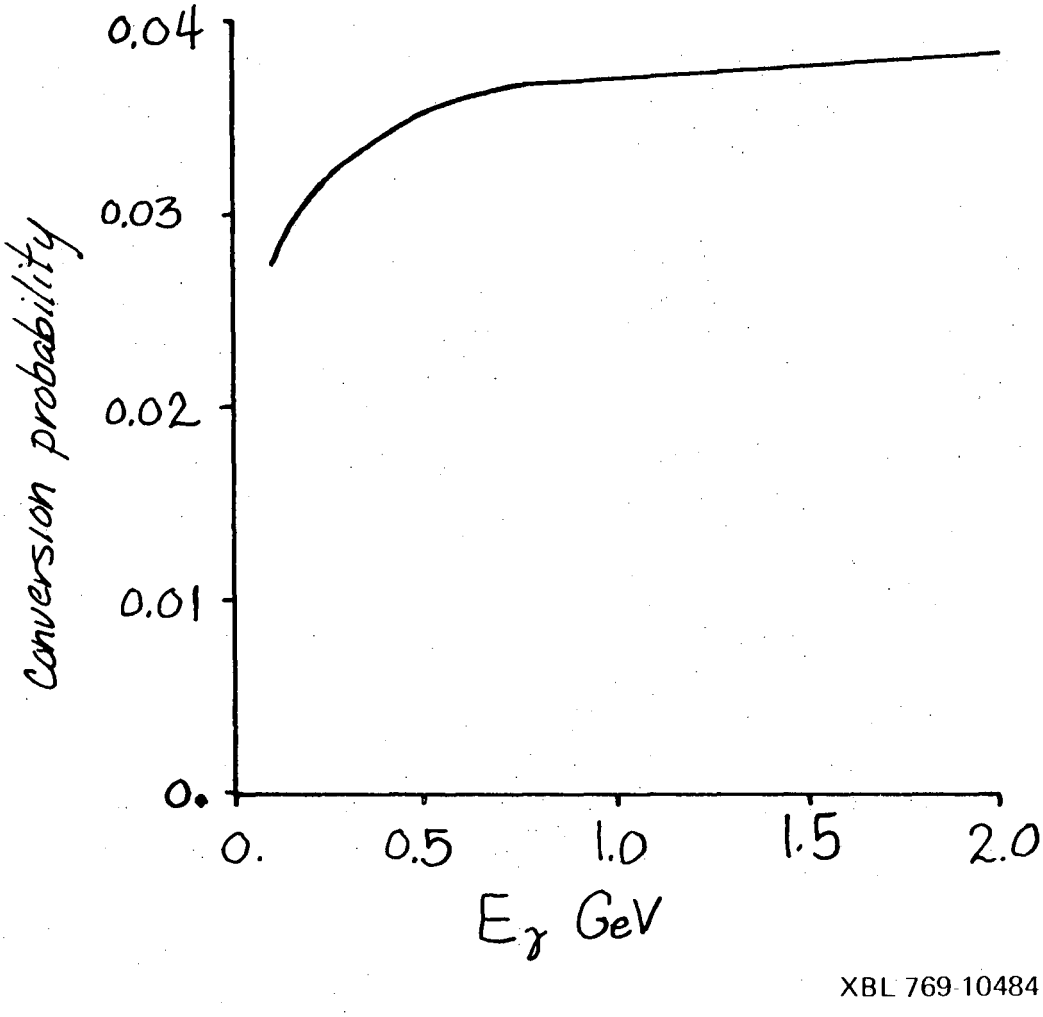

Fig. 12. Conversion probability versus photon energy for normally incident photons.

characterized by the electron mass, so triplet production or broadening of the effective mass distribution of the conversion pairs from the atomic electrons will be negligible. To check this, three particle combinations with small effective mass and total charge ± 1 were selected as triplets. The number of positively charged triplets was equal within statistics to the number of negatively charged triplets, indicating genuine triplet production was small (the observed triplets being attributed to tracking duplications or to accidental hadron combinations).

The electron and positron from a conversion are detected by the four cylindrical spark chambers and the two proportional chambers. There is a minimum transverse momentum of ~ 55 MeV/c required for a particle from near the beam line to traverse two or more spark chambers. From studying the cos θ distribution of detected charged particles, tracks are found with high efficiency out to $\cos\theta > 0.6$. The transverse momentum requirement and the detector angular acceptance determine the efficiency for detecting converted pairs.

Figure 13 shows the calculated photon detection efficiency, for $|\cos\theta_\gamma| < 0.6$ and transverse momentum of the electron and positron > 0.055 GeV/c. The $|\cos\theta_\gamma| < 0.6$ cut was made to avoid regions of uncertain efficiency near the edges of the spark chambers. The calculation takes into account the energy-dependent conversion probability and the detector acceptance, including the 15% loss of acceptance within $|\cos\theta_\gamma| < 0.6$ due to the spark chamber support posts. The calculation takes the energy partition between the positron and the electron in the full screening limit, as given in Heitler.[23] This gives 10% lower acceptance than the zero-screening limit, which is quite close to a flat E_+/E_γ distribution. The photon cos θ distribution is assumed to

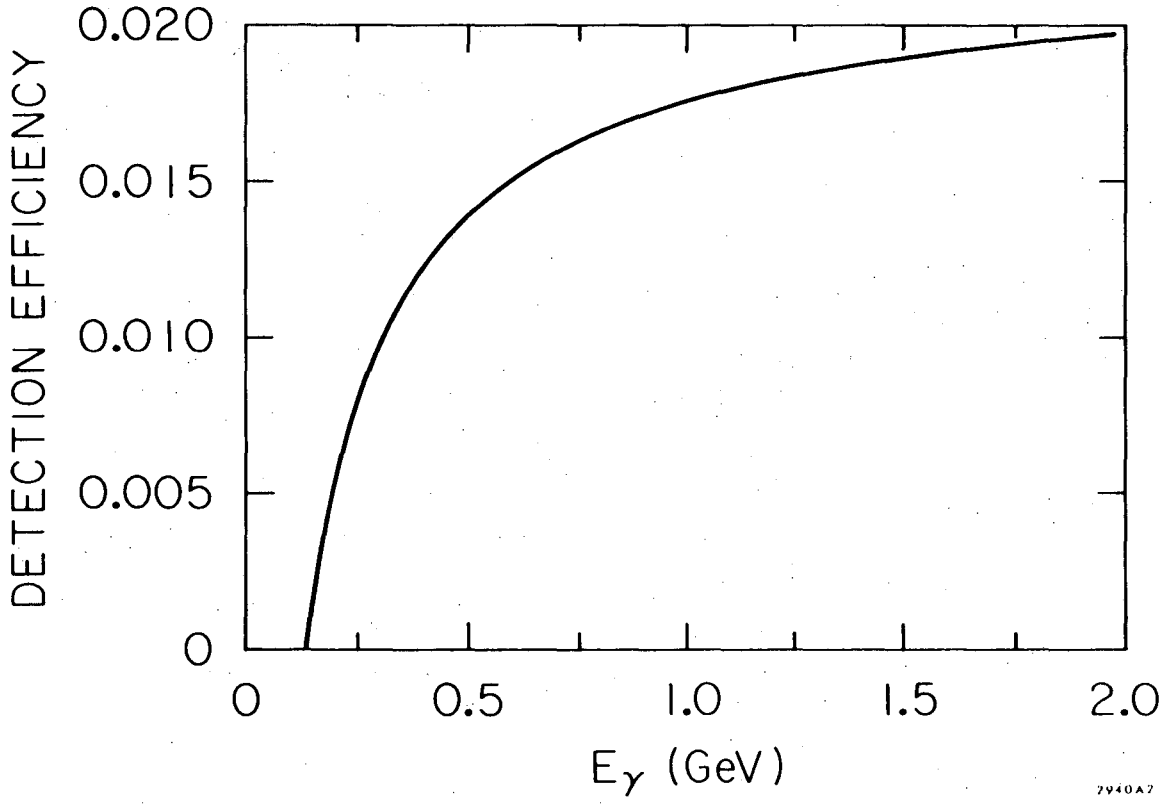

Fig. 13. Photon detection efficiency versus photon energy, for $|\cos \theta_\gamma| < 0.6$.

be isotropic; the acceptance for a $1+\cos^2\theta$ distribution is lower by 16%.

Pairs of oppositely charged particles with small invariant mass-squared M^2 are selected as photon conversions. Calculation of M^2 is complicated by the variable distances of the constituents of the effective converter from the beam line. The invariant mass-squared for a conversion pair is $M^2 = 2p_+p_-(1 - \cos\theta)$ where θ is the opening angle of the particles; since θ is small, $M^2 \approx p_+p_-\theta^2$. Evaluating the vector momenta of the electron and the positron at the wrong radius Δr meters from the true conversion point leads to an increase in the calculated opening angle of $\Delta\theta \sim \frac{\Delta r}{\rho_+} + \frac{\Delta r}{\rho_-}$ where $\rho_\pm$ are the radii of curvature of the tracks. In terms of the momenta, $\Delta\theta \sim 0.12\,\Delta r \frac{p_+ + p_-}{p_+p_-}$ with p_+, p_- in GeV/c. This $\Delta\theta$ is large compared to the natural opening angle and leads to an error in the calculated mass-squared of

$$\Delta M^2 = p_+p_-(\Delta\theta)^2 = (0.12\,\Delta r)^2 \frac{(p_+ + p_-)^2}{p_+p_-} .$$

With the ~ 0.055 GeV/c momentum threshold, the p_+, p_- dependence of ΔM^2 is small and $\Delta M^2 \approx 0.058(\Delta r)^2$ GeV^2 with Δr in meters. The effective converter is located 0.08 to 0.22 meters from the beam line; in addition, photons can convert internally (Dalitz pairs in the case of π^o decay) and make conversion pairs originating at the beam line. To sort this out, the invariant mass-squared for each pair of particles was calculated twice: first, M_c^2, using the vector momenta at a radius of 11.7 cm, the mean radius of the converter; second, M_o^2, using the vector momenta of the tracks at their point of closest approach to the beam line. The CIRCLE momenta were used to avoid problems with tracks missing the ONETRK fit. Figure 14 is a diplot of M_o^2 against M_c^2 for oppositely charged pairs of tracks from ψ' events. Some pairs have M_o^2 near zero and M_c^2 0.0003 to

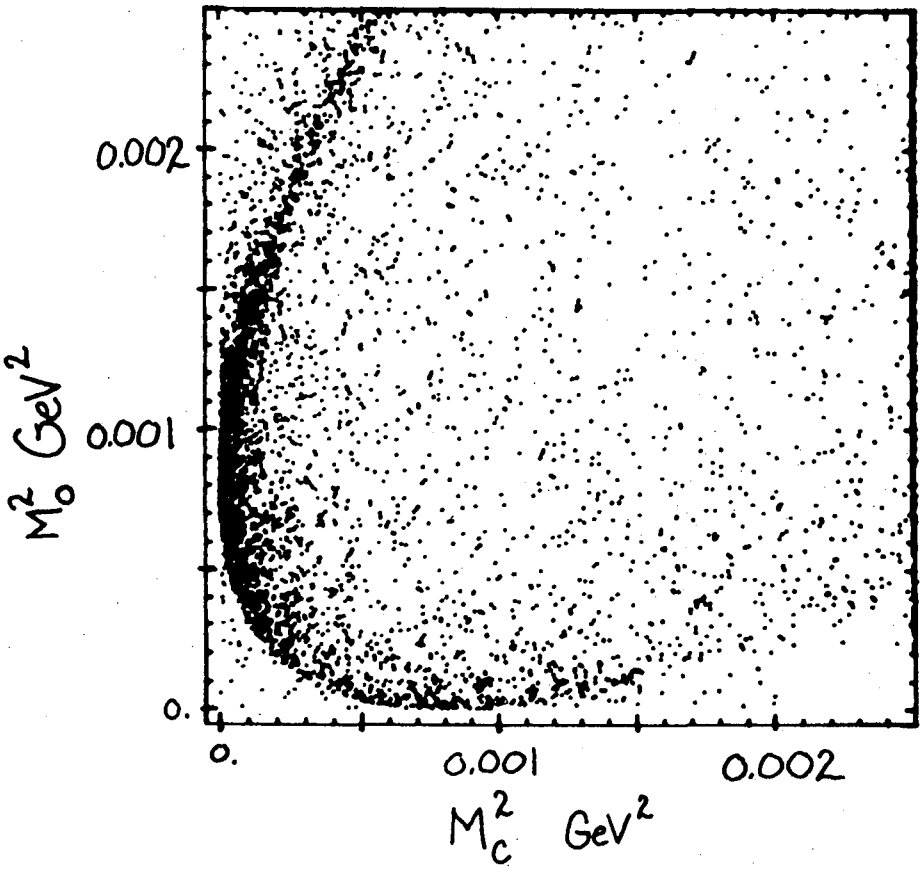

XBL 769-10481

Fig. 14. Mass-squared of (+-) pairs calculated at the mean converter radius, M_c^2, plotted against the mass-squared calculated at the origin, M_o^2.

0.0008 GeV^2, indicating a conversion pair originating near the beam line. There is an accumulation of events with $M_c^2 \cong 0$ and M_o^2 0.0004 to 0.0015 GeV^2 -- these are conversions in the vacuum pipe, pipe counters, and proportional counters. The shape of the high density region in Fig. 14 is due to the relative thickness of the various effective converters and their distance from the two radii at which M_o^2 and M_c^2 are calculated. The scattered points are accidental combinations of hadrons which chanced to have low mass-squared when taken as electrons.

Figure 15a,b shows respectively the M_c^2 and M_o^2 projections from Fig. 14. The dashed histograms in this figure are the mass-squared distributions for the like-charged (++ and --) pairs in the same events. The like-charged pairs will give a rough measure of the accidental hadron background in the conversion signal. There are two effects which enhance the low mass like-charged pair distribution and do not affect the unlike-charged pairs: the track-finding routines may find two tracks, manifestly of the same charge, through the same set of points, and there is a real physical correlation between like-charged particles (the GGLP effect).[24]

A cut against $M_c^2 > 0.00075$ GeV^2 was imposed to select conversion pairs. This cut keeps essentially all the externally converted pairs, admitting $\sim$ 20% accidental hadron-pair background as estimated from the like-charged pairs. The internal conversions will be discussed in detail later; approximately 34% of the internal conversions will fall within this M_c^2 cut, constituting $\sim$ 7% of the total pairs selected.

B. Photon Energy Resolution

The photon energy is calculated as the sum of the energies of the positron and electron. When available, the ONETRK quantities were used; otherwise, the CIRCLE momenta were used. The photon energy resolution

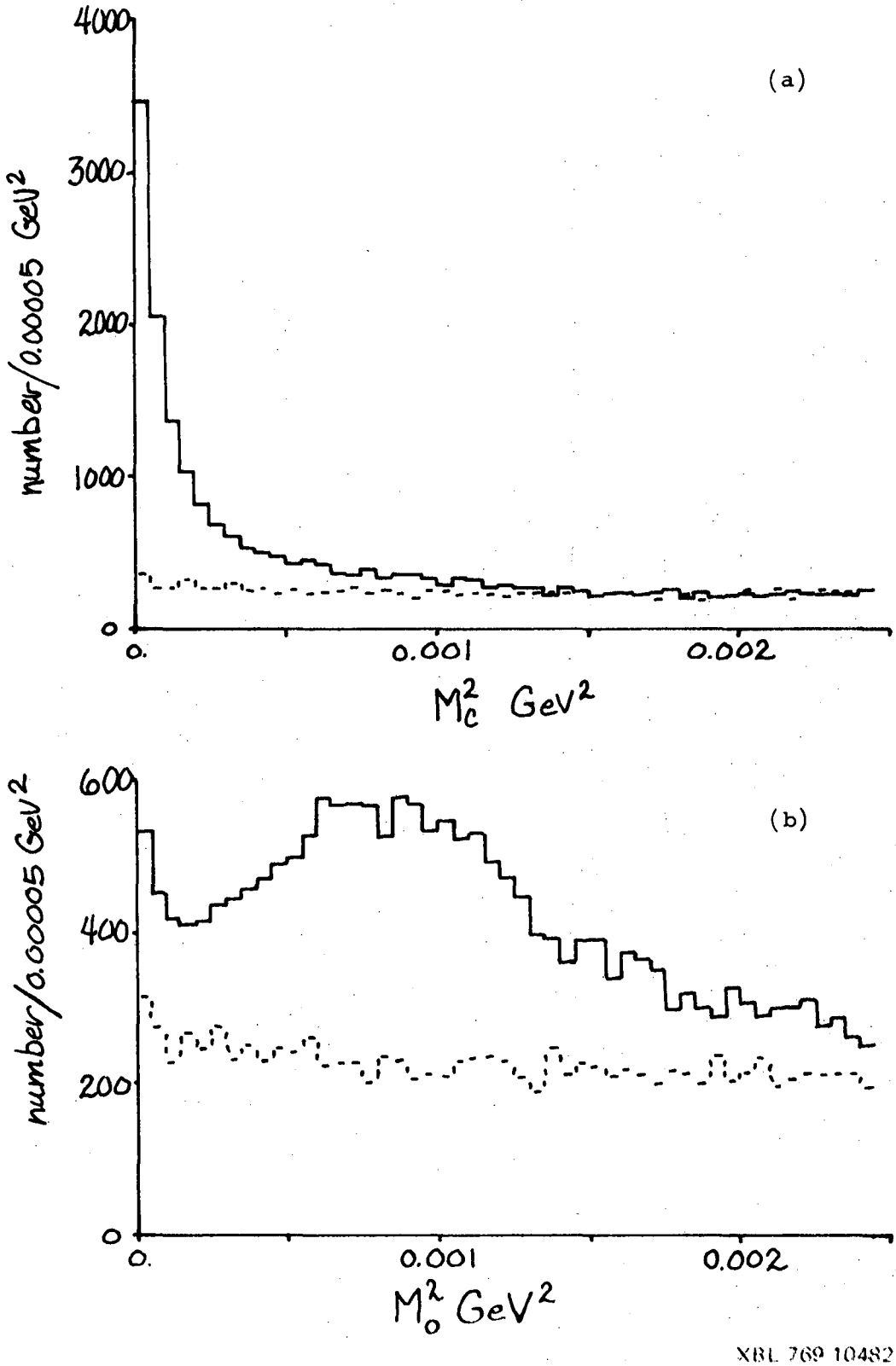

Fig. 15. The (a) M_c^2 projection and (b) M_o^2 projection from Fig. 14. Dotted lines show the distributions for like-charged pairs.

is determined by the momentum resolution of the tracking chambers and by the energy loss of the electron and positron by ionization or radiation as they pass through the material remaining after conversion. The contribution from tracking chamber resolution was measured using the momentum errors calculated in the ONETRK fitting procedure -- recall that the normally-distributed momentum pulls from four-constraint fits to $\psi' \to \pi^+\pi^-\psi$, $\psi \to \mu^+\mu^-$ or e^+e^- and to $\psi' \to 4\pi^\pm$ are evidence that these momentum errors are reasonably correct. Figure 16 shows the mean momentum resolution contribution to photon energy resolution as a function of photon energy, calculated by combining in quadrature the estimated momentum errors of the two tracks of a conversion pair. The error bars in Fig. 16 are the rms deviation from the mean energy resolution, indicating the width of the distribution of photon energy resolution -- the precision with which the uncertainty in photon energy for a single conversion pair is known. Electron masses were assumed in calculating the multiple scattering contribution to the momentum resolution; this may lead to large calculated errors for the background tracks which were hadrons. The trend of the points in Fig. 16, flat at low energy and rising gradually at high energy, is due to the poor momentum resolution of low momentum tracks: photon conversions of energy E_γ have tracks of momenta from threshold ~ 0.055 GeV/c to $E_\gamma - 0.055$ GeV/c; low energy photons have a higher fraction of low momentum tracks than higher energy photons do.

The photon energy resolution is also affected by energy loss by the positron and electron by ionization or radiation as they pass through the material remaining after conversion. The effective converter has a thickness of 2 gm/cm^2 carbon equivalent. The ionization energy loss by electrons in carbon is 1.9 - 2.1 MeV/gm-cm^{-2} for electron energies above

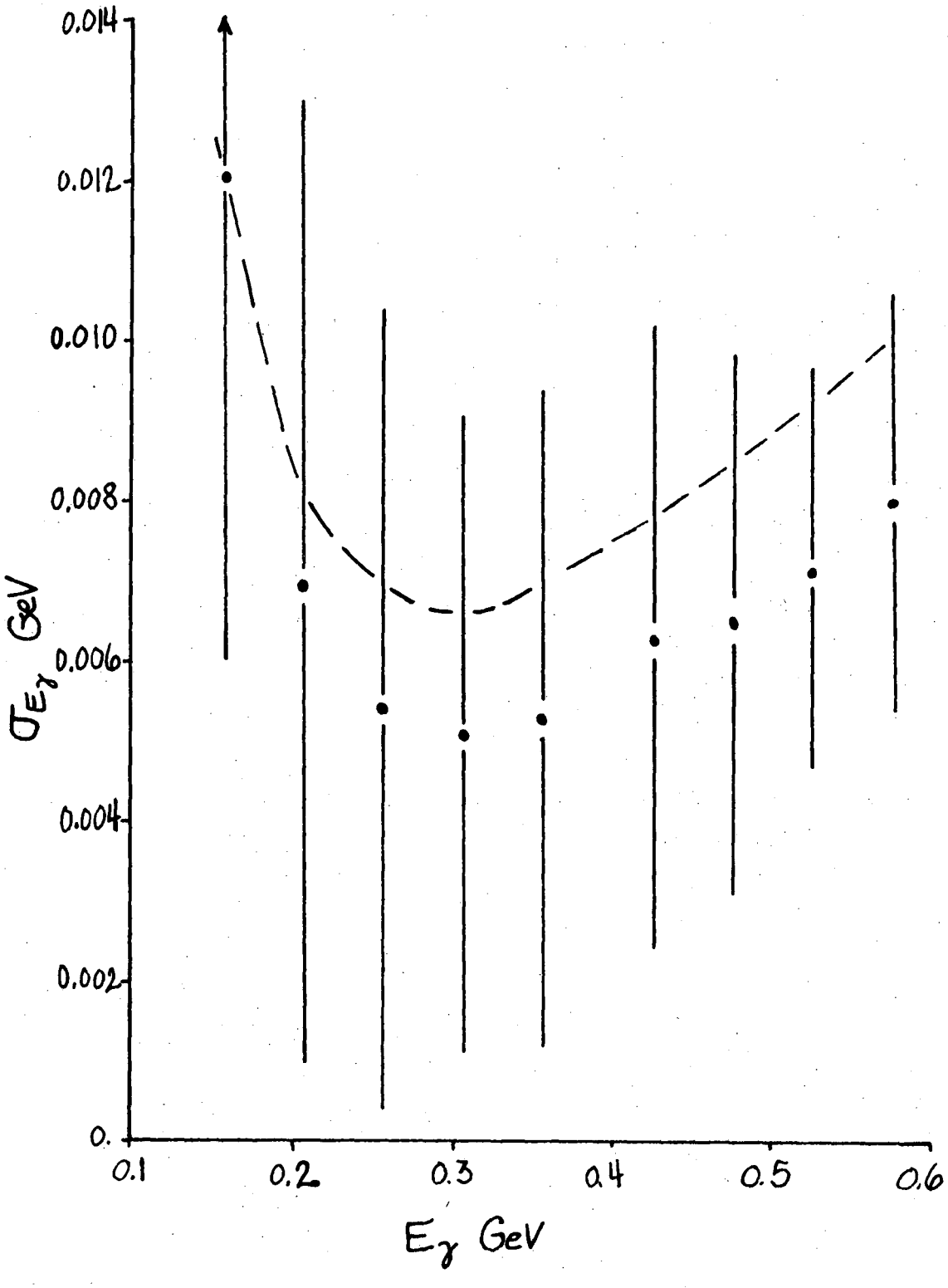

XBL769-10523

Fig. 16. Photon rms energy resolution versus photon energy. The solid line indicates the charged particle momentum resolution effect, the dashed includes also energy loss by ionization and radiation.

50 MeV.[25] The maximum energy loss by ionization for a photon conversion pair is 9.3 MeV, with average energy loss of 4.6 MeV and rms variation of 2.7 MeV.

Radiative effects will be discussed in detail later. Briefly, radiative processes lead to a high probability for the conversion pair to lose a small amount of energy and a small probability of radiating a large amount of energy -- this small probability being roughly independent of the amount of energy radiated. The effect of radiative processes on a monochromatic signal is to broaden the peak slightly, by $\lesssim 1\%$, and to completely remove from the peak a small fraction of the total events, smearing them out roughly uniformly across the landscape.

The photon energy resolution will be the combination of all these effects. The dashed line in Fig. 16 is the sum in quadrature of the momentum resolution, ionization loss, and 1% broadening from the radiative effects. The rms photon resolution is 2-4% for photon energies 0.2 to 2 GeV.

Photons from the QED process $e^+e^- \rightarrow \gamma\gamma$, where one of the photons converts internally or externally, may be detected. Candidate events for this process were selected as two-track events in which the two tracks formed a conversion pair and in which one of the two shower counters directly opposite the converted photon was latched. Figure 17 shows the photon energy distribution for these events; there is a very clear signal for monochromatic photon production at ~ 1.86 GeV, with an rms resolution of ~ 50 MeV.

In order to satisfy the trigger requirement of a signal in both pipe counters, the conversion must occur either internally or externally in the vacuum pipe or early enough in the inner pipe counter to latch that counter. The uncertainty of how much of the inner pipe counter is

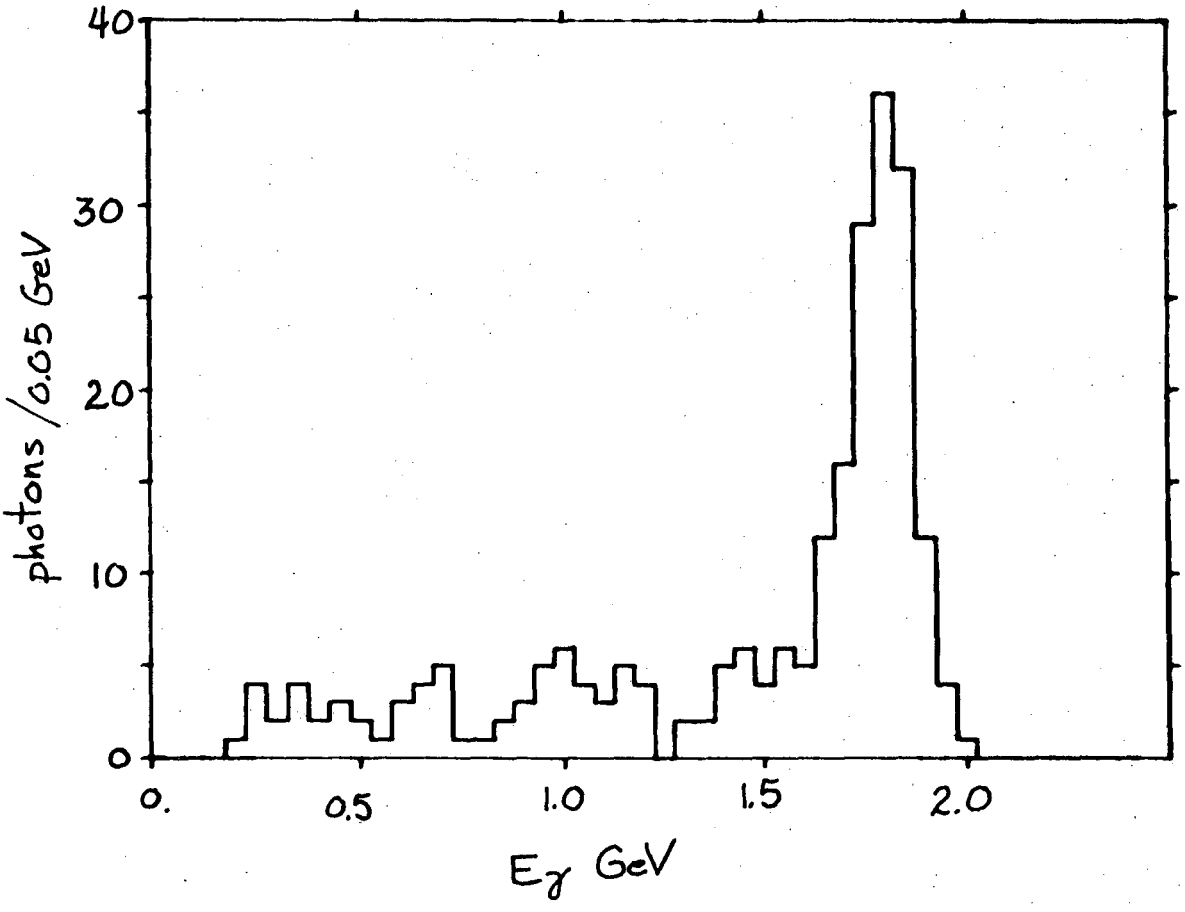

XBL 769-10483

Fig. 17. Photon energy distribution for candidates for $e^+e^- \to \gamma\gamma$, with one γ converting.

effective as a converter precludes the use of these events to test the conversion efficiency; the "internal conversion" radiative corrections also complicate this. Agreement with the calculated rate is good, within the $\sim 40\%$ systematic uncertainty.

Figure 18 shows a computer reconstruction of a typical event with a converted photon. The photon, tracks 4 and 6, has energy of ~ 260 MeV. The symbols at the ends of the tracks represent the latched trigger and shower counters.

C. The Inclusive Photon Spectra

Figure 19 is the inclusive spectrum for 5561 photons from 150,000 ψ events. No cuts have been made to define the angular acceptance; the data are plotted in 4% energy bins. Figure 20 is the ψ inclusive spectrum for 4659 photons with $|\cos\theta_\gamma| < 0.6$. These spectra have a gross shape determined by the acceptance folded on the photon spectrum from hadron decays, predominantly π^o decay products. The photon spectrum from π^o decay has its maximum at $E_\gamma = m_{\pi^o}/2 = 67$ MeV and falls roughly exponentially; the observed spectrum, zero below 110 MeV and with a broad maximum from $\sim 250 - 500$ MeV, reflects the effect of increasing acceptance multiplying the falling produced photon spectrum. The smooth curve in Fig. 20 is the inclusive photon spectrum from a pion phase-space Monte Carlo of ψ events, normalized to the data in the 300 - 350 MeV region. The shape of the experimental spectrum agrees very well with the Monte-Carlo results; further discussion of the Monte-Carlo simulation will be deferred for a bit.

Figure 21 is the inclusive spectrum for 14,000 photons from 330,000 ψ' events; Fig. 22 is the spectrum for the photons with $|\cos\theta| < 0.6$. The data are again presented in 4% energy bins. The general shapes of

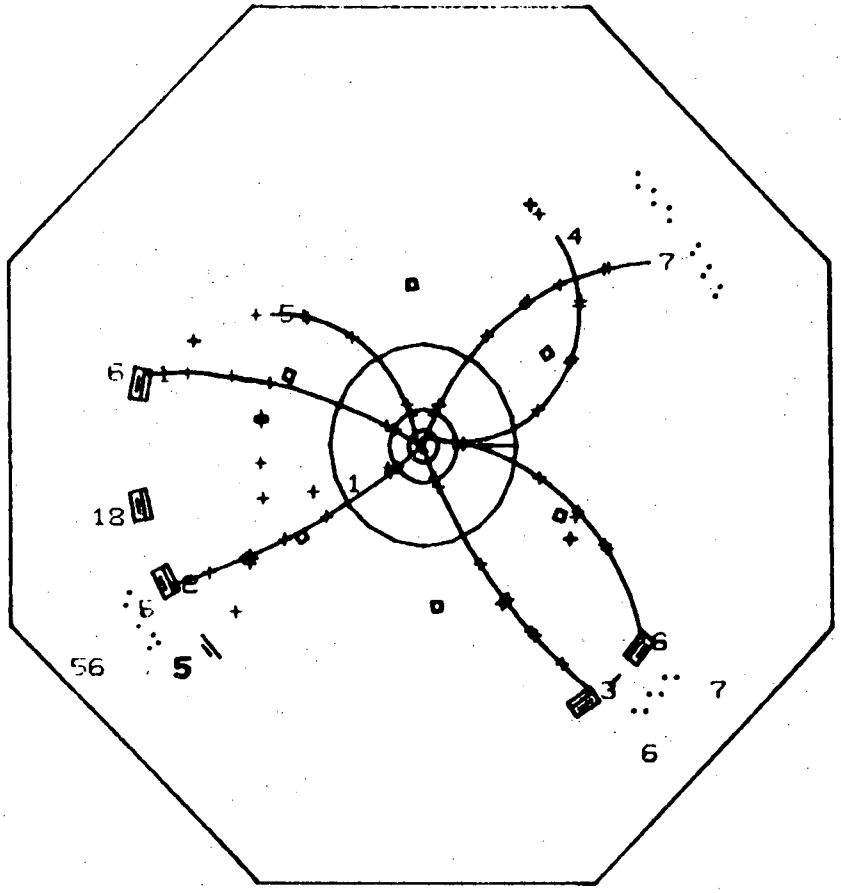

XBL 769-10473

Fig. 18. A typical event with a converted photon.

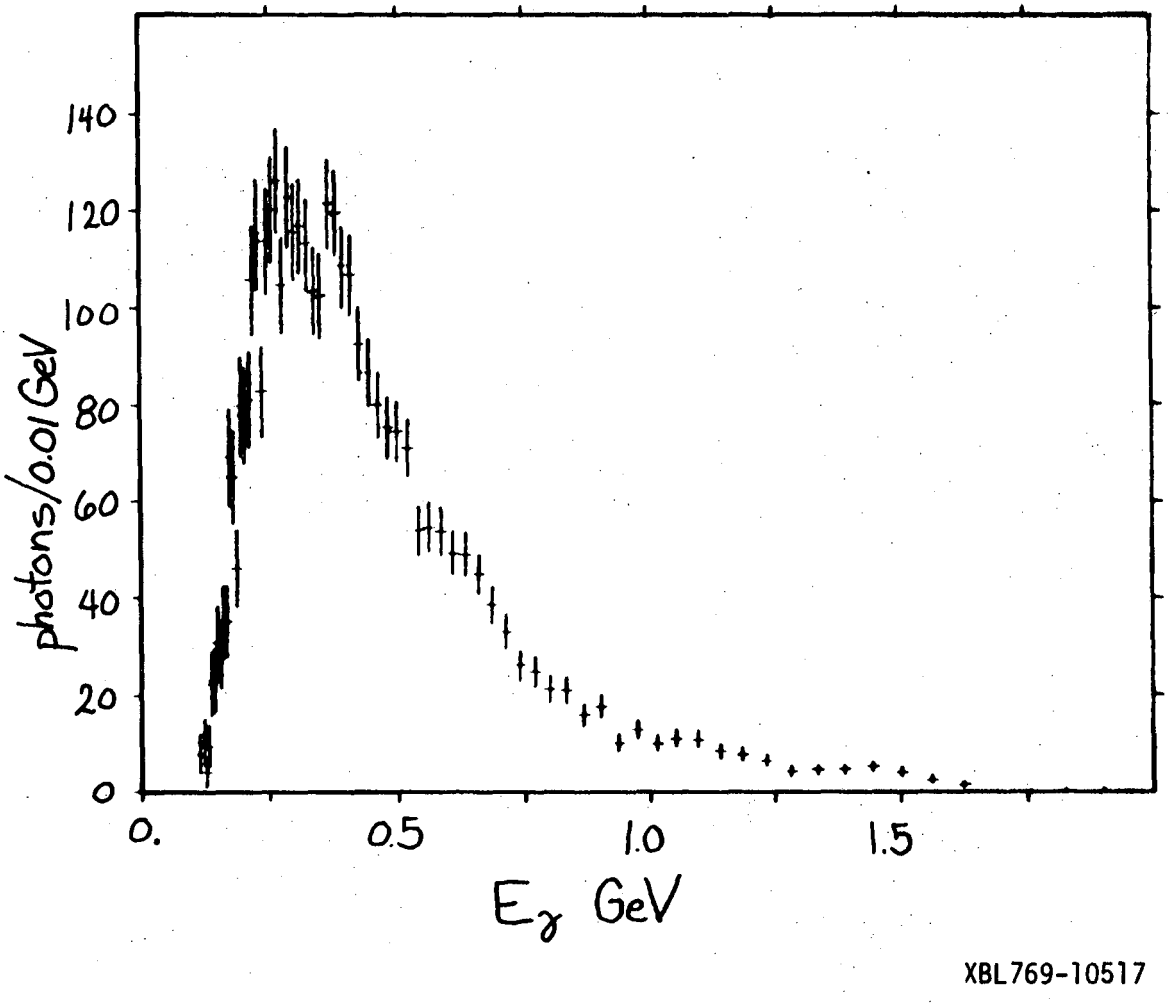

Fig. 19. The ψ inclusive photon spectrum.

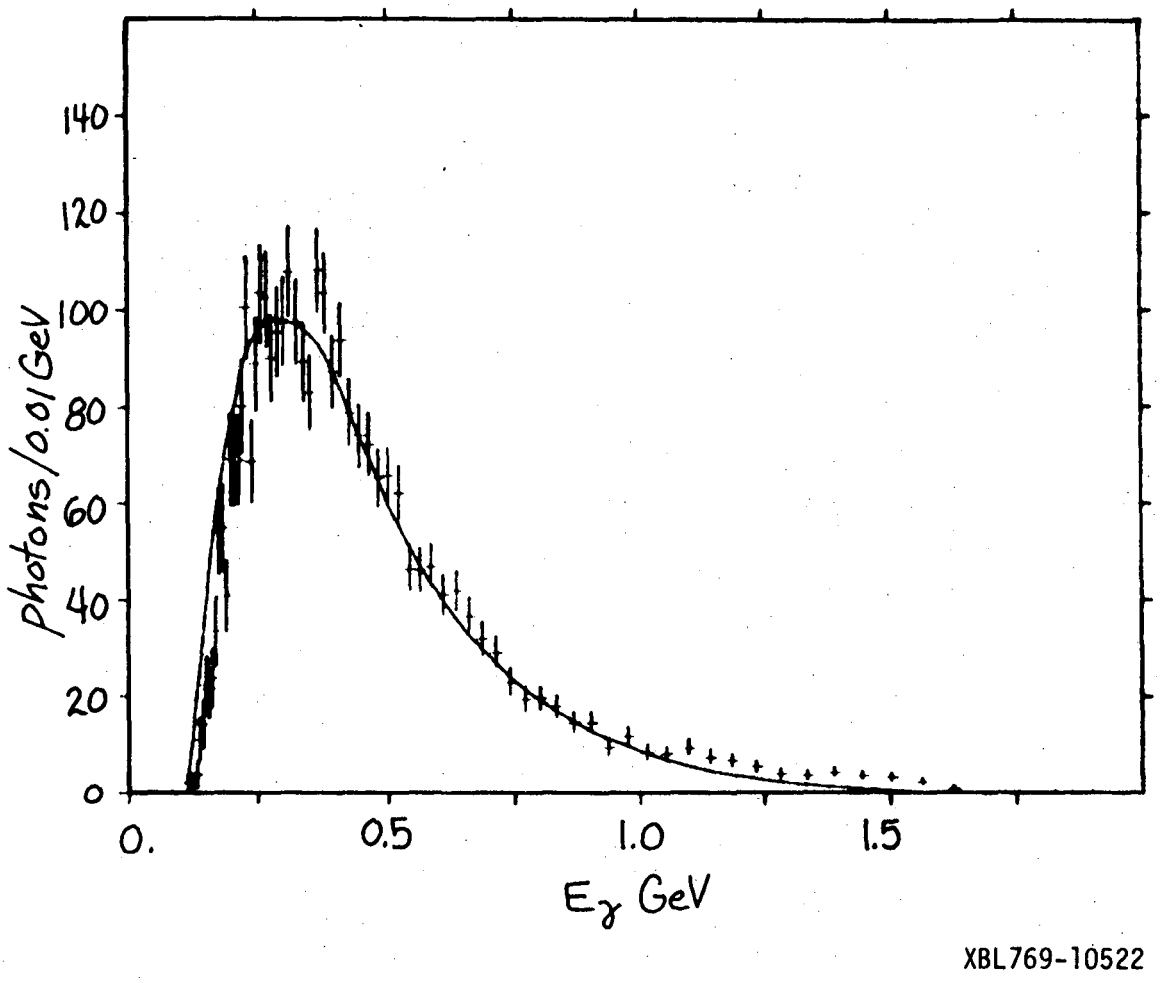

Fig. 20. The ψ inclusive photon spectrum with $|\cos\theta_\gamma| < 0.6$. The line is the photon spectrum from a Monte-Carlo simulation of ψ events.

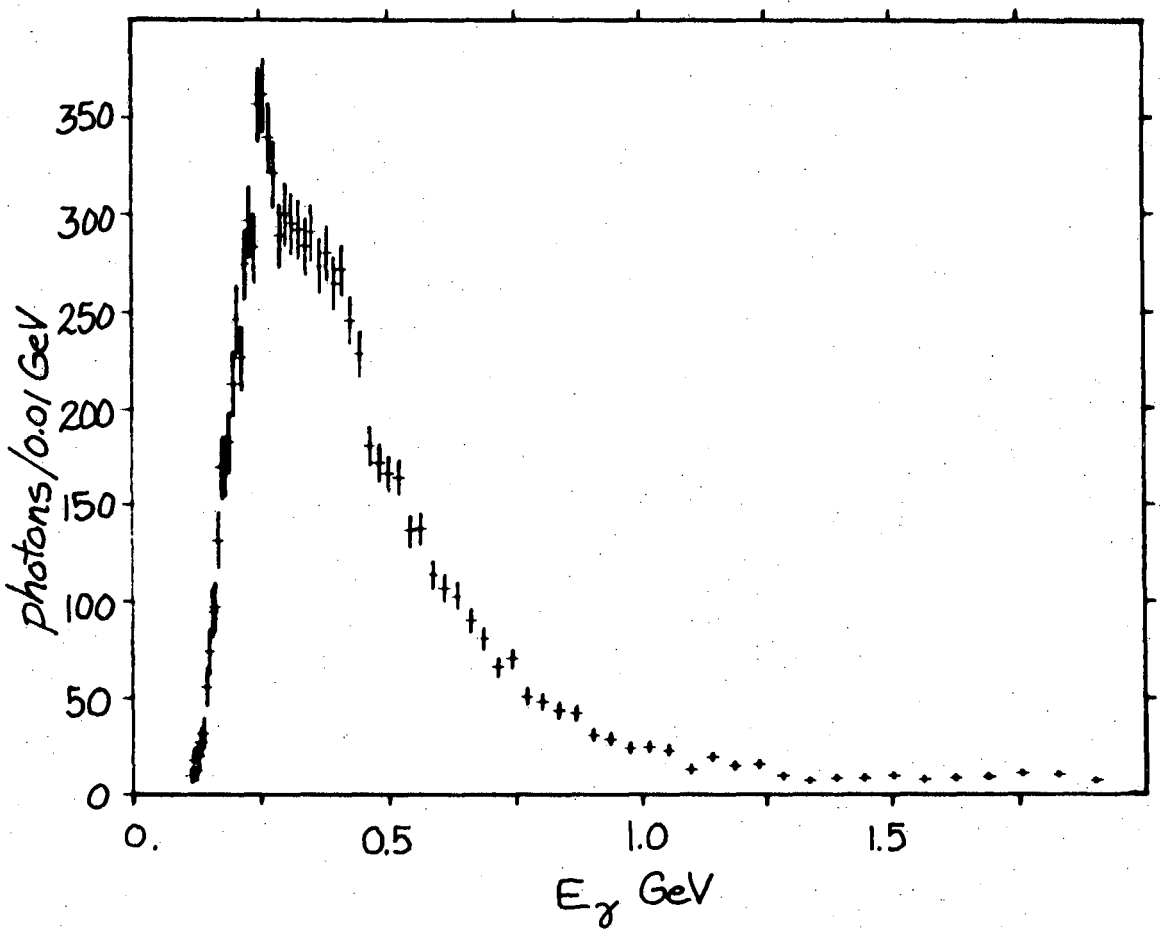

Fig. 21. The ψ' inclusive photon spectrum.

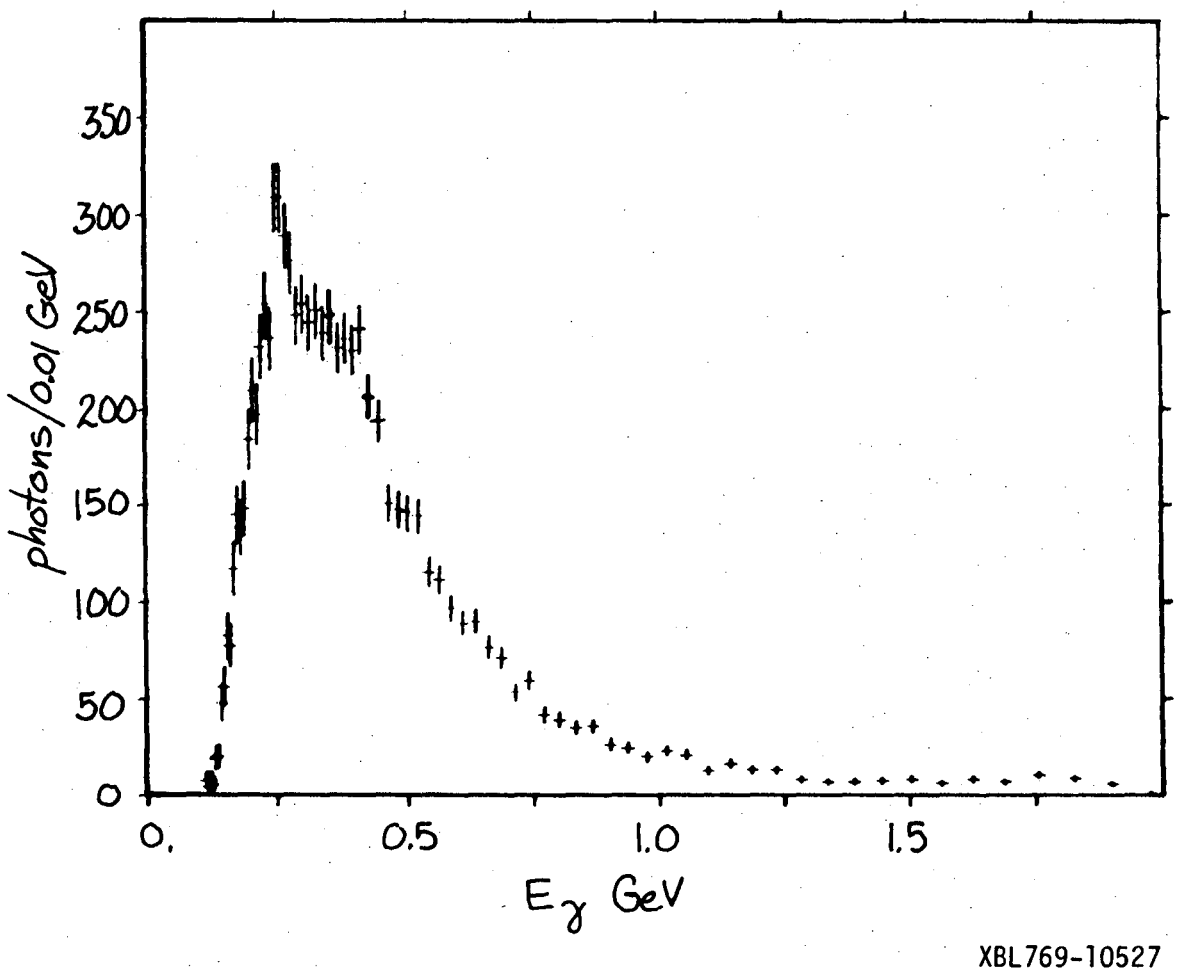

Fig. 22. The ψ' inclusive photon spectrum with $|\cos\theta_\gamma| < 0.6$.

these spectra are very similar to those for the ψ, not surprisingly since 57% of ψ' decays go via ψ. In addition, there is a clear peak at $E_\gamma \sim$ 260 MeV with a full width at half maximum of $\sim$ 20 MeV, consistent with the expected resolution of a narrow signal. To check that this peak is not being shaped by the rapidly varying acceptance, the data were analyzed imposing successively cuts of 55, 65, and 75 MeV/c on the transverse momenta of the electron and positron. The 55 MeV/c cut corresponds to the physical limits of the detector; the 65 MeV/c and 75 MeV/c cuts reduce the acceptance by 16% and 31% respectively and change the slope of the acceptance in the 260 MeV region dramatically. Figure 23a,b,c shows the ψ' inclusive photon spectrum with $|\cos\theta_\gamma| < 0.6$ and 55 MeV/c, 65 MeV/c, and 75 MeV/c transverse momentum cuts. The peak stays at the same energy with approximately the same observed width, demonstrating that the peak is not being shaped by the acceptance.

The peak is located at 256 ± 10 MeV, where the error reflects the uncertainty in the relative peak position and the systematic uncertainty in the energy scale. The actual energy of the monochromatic photon is 4.6 MeV higher due to the energy lost by ionization by the electron and positron after the conversion as they traverse the remaining material. After this correction the line is at 261 ± 10 MeV. This corresponds to a transition from ψ' to a state of mass 3413 ± 11 MeV; we identify this with the state X(3415) observed in the hadronic decay channels (see Ref. 19 and Chapter IV). There is no other likely explanation of this bump. The photons from $\eta \to \gamma\gamma$ from inclusive η production will peak at $m_\eta/2 = 275$ MeV and will have a broad distribution reflecting the momentum distribution of the η's. The photons from $\psi' \to \psi\eta$, $\eta \to \gamma\gamma$ will be Doppler broadened and smeared from 193 to 389 MeV uniformly. The absence of this bump in the ψ spectrum puts to rest the possibility that it is

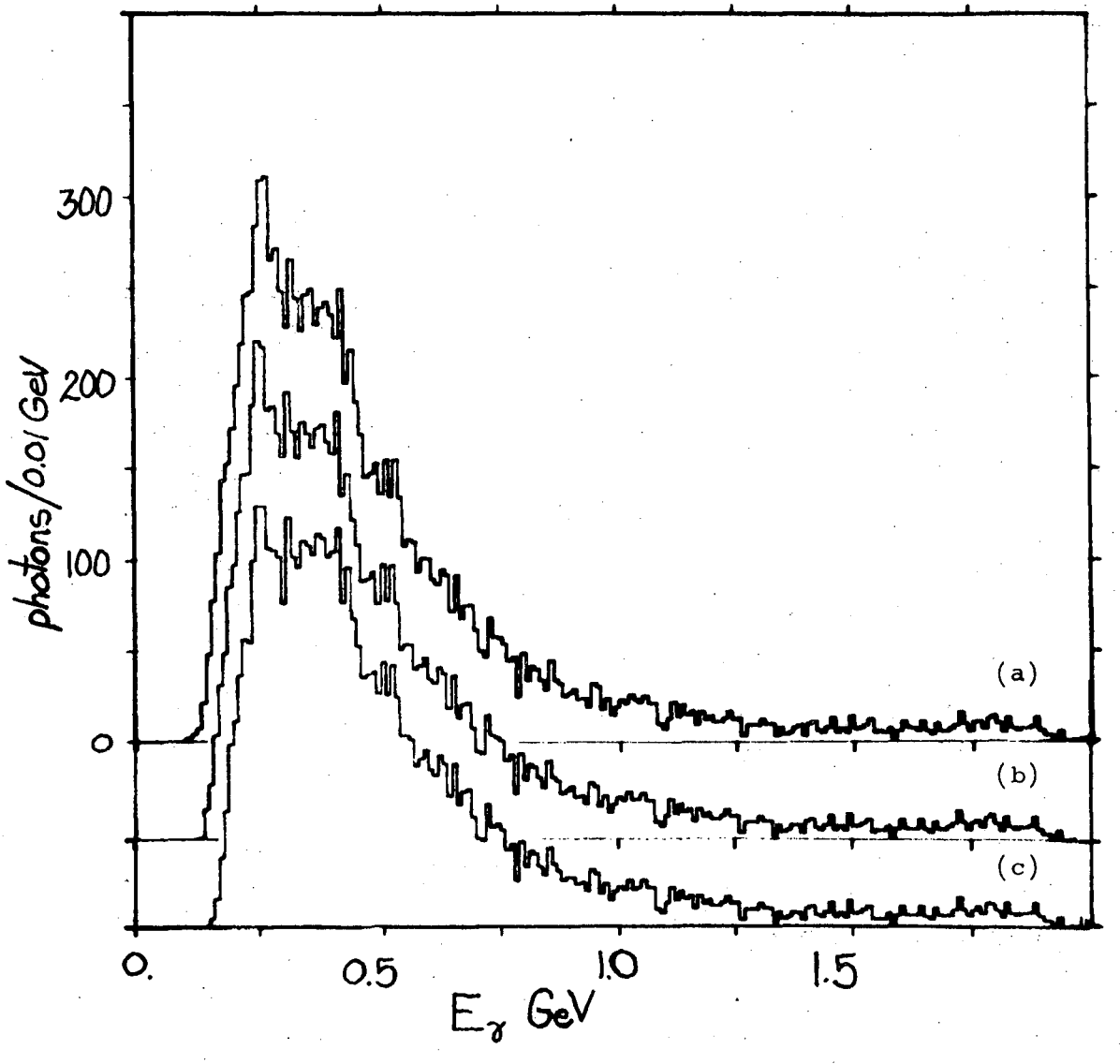

Fig. 23. The ψ' inclusive photon spectrum with $|\cos\theta_\gamma| < 0.6$ and charged particle transverse momentum cuts of (a) 55 MeV/c, (b) 65 MeV/c, (c) 75 MeV/c.

produced in ψ decays from the $\psi' \to \psi$ cascade events.

D. Branching Fraction Calculation

The branching fraction for this transition is calculated as

$$BF = \frac{(\text{no. of signal events})/(\text{photon det. eff.} \cdot RC \cdot \epsilon_{tr}^{s})}{(\text{no. of total events})/\epsilon_{tr}^{all}} \times f_{ext} .$$

Here RC is a correction for radiative losses, ϵ_{tr}^{all} is the average trigger efficiency for hadronic events, and ϵ_{tr}^{s} is the trigger efficiency for events containing a $\sim$ 260 MeV photon conversion. The photon in the radiative transition may convert internally to an electron-positron pair; f_{ext} is a correction for internal conversions which pass the cuts selecting photon conversions. The number of signal events is the excess over the smooth background; for reasons to be revealed shortly, the ψ Monte-Carlo results were used to estimate the background. The number of total events is calculated from the number of events used to compile the inclusive spectrum with corrections for nonresonant hadronic and QED events and for the higher trigger efficiency of the leptonic decays of ψ and ψ'. Starting out with 356,970 ψ' events, 47,310 of these were "QED-type" events -- events with two collinear high-energy prongs, or with three prongs with high shower counter pulse height typical of high energy electrons. These events could be ψ or ψ' decays to muon pairs or to electron pairs, or they could be due to nonresonant processes $e^+e^- \to \mu^+\mu^-$ or $e^+e^- \to e^+e^-$. The three-prong events were electron pair events with a "knock-on" delta ray from the effective converter. From the leptonic branching fractions of ψ and ψ' and the $\psi' \to \psi$ cascade rate, $\sim$ 25% of these QED-type events are resonant ψ' events. The nonresonant hadronic total cross section in this region is $\sim$ 20 nb while the effective ψ' peak cross section is $\sim$ 600 nb, implying a $\sim$ 3%

subtraction for nonresonant hadronic events. There is a slight further correction since the trigger efficiency for the QED events is roughly just the detector acceptance, so we correct the number of QED-type events by 0.5/0.7 where 0.5 is roughly the hadronic trigger efficiency and 0.7 is the detector solid angle covered. The total number of events is then 308,818 events, with $\lesssim 5\%$ error.

E. Trigger Efficiencies

The photon acceptance so far discussed does not include the detector trigger efficiency, that is, the probability that the event met the trigger criteria. As discussed in Appendix A, the TASH efficiency for electrons and positrons is significantly higher than for pions at low momenta; hence, the trigger efficiency ϵ_{tr}^{s} for events including a converted photon is higher than for events consisting only of hadrons, ϵ_{tr}^{all}. This effect was measured from the data in two ways. The first method involved scanning events which contained photon conversions with $0.250 < E_{\gamma} < 0.270$ GeV. The events were reconstructed and simulated pictures of the events were generated, as shown in Fig. 18. Events were required to have no other particles striking the counters which were associated with the electron and positron from the conversion. In this way, it was possible to determine the number of TASH's due to the conversion pair and the number due to the other particles in the event. The cut against events with particles near the counters for the conversion particles slightly biased the sample to lower multiplicity and hence lower efficiency; also, accidental shower counter hits (as discussed in Appendix A) raised the effective TASH efficiency for the conversion pair. Due to the large number of counters and the high TASH efficiency for positrons and electrons these effects should be moderately small.

Of the original sample of 248 events, 174 passed the cut for other particles in the conversion counters. Twenty-one of these events had two solid TASH's from the conversion pair and hence enable us to measure the hadronic trigger efficiency. Nine of these 21 events had ≥ 2 TASH's from the hadrons; 12 did not, implying a hadronic trigger efficiency of $\sim 0.43 \pm 0.11$, in good agreement with Monte-Carlo calculations. Of the 174 events, 55 had < 2 TASH's from the hadrons. Denoting the trigger efficiency for events with a photon conversion as ϵ_{tr}^{s} and the average trigger efficiency for all hadronic events as ϵ_{tr}^{all}, this predicts $\epsilon_{tr}^{all}/\epsilon_{tr}^{s} = 1 - 55/174 = 0.68 \pm 0.11$.

The second scheme for measuring $\epsilon_{tr}^{all}/\epsilon_{tr}^{s}$ was an automated version of the first. The latches for counters associated with a conversion particle were turned off, and the event was examined to see if it still met the trigger conditions. Depending on whether the electron or positron or both had momenta high enough to reach the trigger and shower counters, zero, one, or two sets of counters were turned off. This eliminated the contribution to triggering from the conversion, but also eliminated the beneficial influence of other particles which hit the same counters. To correct this, the number of counters turned off was measured as a function of photon energy. The data were analyzed while randomly turning off a counter set, and while randomly turning off two counter sets. This measured the accidental losses; these results were then weighted according to the number of counters turned off by a given energy photon conversion to calculate the accidental losses for photon conversions of that energy. After this correction for the accidental losses, $\epsilon_{tr}^{all}/\epsilon_{tr}^{s}$ could be calculated. This method avoided the multiplicity bias present in the first method, but still included the accidental TASH effect. The ratio shows $\epsilon_{tr}^{all}/\epsilon_{tr}^{s}$ decreases with energy from ~ 1 to ~ 0.5 as calculated by this

scheme. For $0.250 < E_\gamma < 0.270$ GeV this method found $\epsilon_{tr}^{all}/\epsilon_{tr}^{s}$ to be 0.74 ± 0.07, in good agreement with the other calculation -- in fact, slightly higher as expected due to the multiplicity bias in Method 1.

F. Radiative Effects

Photon conversions may have their energy significantly altered or may be lost completely due to radiation by the electron or positron as they pass through the remaining material after conversion. There are two ways to calculate this, one simple and one a bit more complicated. In the simple approach, the ensemble of photon conversions is reduced to a "typical" conversion where the electron and positron each have half the photon energy and the conversion occurs half-way through the radiator. Furthermore, we ignore the possibility of more than one radiative interaction for the positron and electron together. In these approximations, the radiative losses for photons of energy E_γ converting in radiator of thickness t radiation lengths are the same as the losses for a single electron of energy $E_\gamma/2$ traversing t radiation lengths. According to Rossi,[26] the probability per radiation length for an electron to radiate a photon carrying away a fraction v of the total energy is

$$\Phi_{rad}(v) = \frac{1}{v}\left[1 + (1 - v)^2 - (1 - v)\left(\frac{2}{3} - 2b\right)\right] ,$$

where $b \approx 0.0135$ is a small constant nearly independent of the converter material. The probability $P_{lost}(v)$ that a photon of energy E_γ converting in a radiator t radiation lengths thick will yield an electron and a positron with total energy $E > (1 - v)E_\gamma$ after exiting the radiator is then

$$P_{lost}(v) = t \int_{2v}^{1} \Phi_{rad}(u)du .$$

For $t = 0.0515$ and $v = 0.035$, this gives $P_{lost}(0.035) = 0.15$; i.e., 15% of photons converting in this 5% radiator will produce pairs with less than 96.5% of the original photon energy.

A more precise calculation includes the possibility of plural interactions and the variation of conversion point within the radiator. Bethe and Heitler have calculated,[27] neglecting collision loss and using an approximate formula for the differential radiation probability, that the probability an electron of energy E_o traversing a radiator of thickness t will emerge with energy in dE at E' is

$$\omega(E_o,E,t)dE = \frac{dE}{E_o} \frac{[\ell n(E_o/E)]^{\frac{t}{\ell n 2}-1}}{\Gamma(t/\ell n 2)} .$$

This distribution was incorporated in a Monte-Carlo calculation in which photons were allowed to convert uniformly through the converter and the positron and electron independently propagated; for simplicity, a flat E_+/E_γ distribution was used. (Figure 24 shows the fractional observed energy distribution for 260 MeV photons.) This calculation revealed:

(1) 16% of converted photons lost $> 3.5\%$ of the original energy,

(2) the fraction of conversions losing $> 3.5\%$ is a nearly linear fraction of the radiator thickness.

These results are in good agreement with the earlier calculation, as expected for a thin converter. Furthermore, this calculation indicated that 7% of 200 MeV photon conversions and 3% of 400 MeV photon conversions are lost due to one or the other particle losing enough energy to fall below the 55 MeV/c transverse momentum threshold. These losses represent a lower limit to the losses from the inclusive photon spectrum, since in the case of large radiation, the invariant mass of the conversion pair may be increased greatly by opening up the angle between the particles, moving the mass beyond the cut. However, such large angle radiative processes are infrequent and will not be a large effect.

A slight further correction is necessary to account for the departure

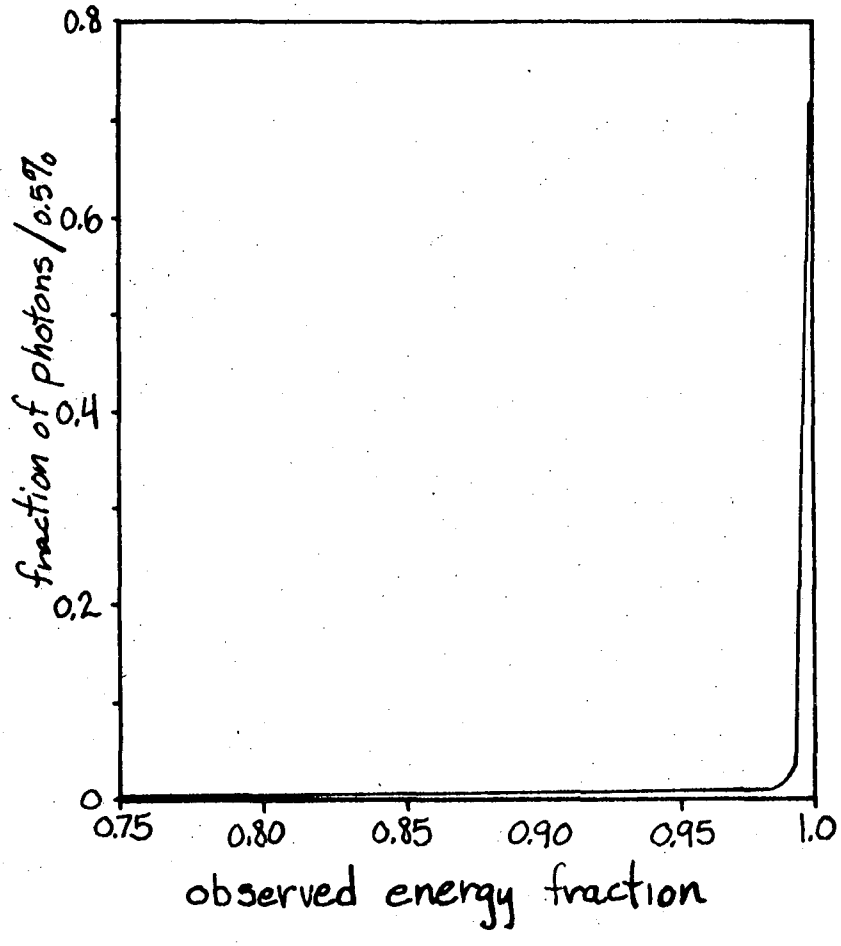

Fig. 24. Fractional observed energy distribution for Monte-Carlo simulated radiation losses of 260 MeV photon conversions.

from normal incidence of photons upon the converter. The probability of conversion and the probability of radiation both grow linearly with the converter thickness, which varies as $(1/\sin\theta)$ for this cylindrical geometry. The radiative losses then are higher by the weighting of $(1/\sin^2\theta)$, increasing the 16% loss to 20%. Thus we conclude RC ~ 0.8.

G. Internal Conversions

Photon conversions may also happen internally, as in the case of the Dalitz decay of the π^o. In the case of π^o's, the internal conversion rate is 1.17% for $\pi^o \to \gamma e^+ e^-$, or an internal conversion probability of 0.58% per photon. Internal conversion rates for transitions from a particle of mass M+E to a particle of mass M have been calculated by Kroll and Wada[28] and by Joseph[29] to be

$$\rho_T = \frac{2\alpha}{3\pi}\left\{\ell n\left(\frac{2E}{m}\right) - \frac{11}{6} - g(E/M)\right\} \quad ,$$

where m is the electron mass, g(E/M) is a small term, and the longitudinal polarization component has been neglected. For E ~ 250--300 MeV this gives a probability of ~ 0.8% for internal conversion. Hence for photons from π^o's or from radiative decays to massive states, internal conversions will make contributions which are a sizable fraction of those from external conversions. However, the cuts made to reduce the background to the sample of externally converted photons also eliminate many internal conversions. To calculate the fraction of internal conversions which pass the M_c^2 cut, the mass distribution for internal conversions from Ref. 28 was incorporated in a Monte Carlo which assumed, for simplicity, a flat E_+/E_γ distribution. This simulation program generated an M_c^2 distribution for internal conversions which indicated, allowing for resolution effects, that 34% of the internal conversions would pass the M_c^2 cut of 0.00075 GeV^2. Thus the probability of a photon entering the monochromatic

signal via an internal conversion, in comparison to the probability for internal plus external conversions is $\frac{0.34 \times 0.008}{0.036 + 0.34 \times 0.008} = 0.07$, where 0.036 is the probability for external conversions and the detector acceptance cancels out of numerator and denominator. This leads to a value for f_{ext} of 0.93.

Plugging in all the factors, the branching fraction for $\psi' \to \gamma\chi(3415)$ is 0.063 ± 0.022 for an isotropic photon distribution and 0.075 ± 0.026 for a $1 + \cos^2\theta$ distribution; as noted in Chapter IV, the $1 + \cos^2\theta$ distribution is favored by the data. The 35% relative error is the sum in quadrature of the 17% statistical error and estimated systematic errors of 20% in the background subtraction, 20% in the photon detection efficiency, 10% in the $\epsilon_{tr}^{all}/\epsilon_{tr}^{s}$ calculation, and 5% in the radiative correction.

H. Comparison of Internal and External Conversions

It is of course important to check that the detector and the analysis programs functioned as expected and that photon conversions were detected efficiently. It was possible to check the photon conversion rate by comparing the relative populations of internal and external conversions. As shown in Fig. 14, internal and external conversions populate different regions of the $M_o^2 - M_c^2$ diplot. Pairs of opposite charge with $M_o^2 < 0.0002$ GeV^2 were classified as internal conversions (IC's); pairs with $M_o^2 > 0.0002$ GeV^2 and $M_c^2 < 0.00075$ GeV^2 were classified as external conversions (EC's). All external conversions should fall in the EC class, since the mass-squared shift for conversions in the vacuum pipe, the innermost converter, is $\Delta M_o^2 \gtrsim 0.00034$ GeV^2. Using the formula from Ref. 29 for the mass-squared distribution of internal conversions from π^o decay, $\sim 67\%$ of internal conversions will fall in the IC class. In the approximations discussed earlier, internal conversions with $M_c^2 < 0.00064$ GeV^2 will also have

$M_o^2 > 0.00020$ GeV^2 and will fall in the EC class; this amounts to $\sim 15\%$ of the internal conversions. Taking these losses into account, the EC and IC populations should reflect the relative probabilities for external conversion and internal conversion. Assuming most internal conversions come from π^o's, the probability for a photon to fall in the IC population will be 0.67×0.0059, where 0.0059 is the internal conversion probability per photon in a π^o decay; the EC probability will be 0.15×0.0059 plus the (energy-dependent) external conversion probability (the detector acceptance is the same for both types of conversion pairs and has been omitted).

The accidental backgrounds in the two classes must be subtracted. Background in the IC class can be estimated from the M_o^2 distribution for like-charged pairs and is $\sim 50\%$. It is somewhat erroneous to use like-charged pairs to estimate background to the EC class since like-charge pairs to first order do not experience the mass-squared shift when M^2 is calculated using the momenta at different positions -- the tracks are curving the same direction -- and the $M_o^2 > 0.00020$ GeV^2 cut eliminates some of the background. This effect makes the $\sim 20\%$ background subtraction to the EC class uncertain at the 25 - 50% level.

Figure 25 shows the background-subtracted energy distributions for internal and external conversions. The internal conversions are plotted with the solid points in Fig. 25; the external conversions, scaled by the ratio of probabilities for photons falling in the IC and EC classes, are plotted with open points. The scale factor for the external conversions was 0.12 at 0.2 GeV and dropped to 0.10 at 1 GeV as the external conversion probability rose. The good agreement between the two spectra in Fig. 25 is evidence that external conversions occur with the expected rate.

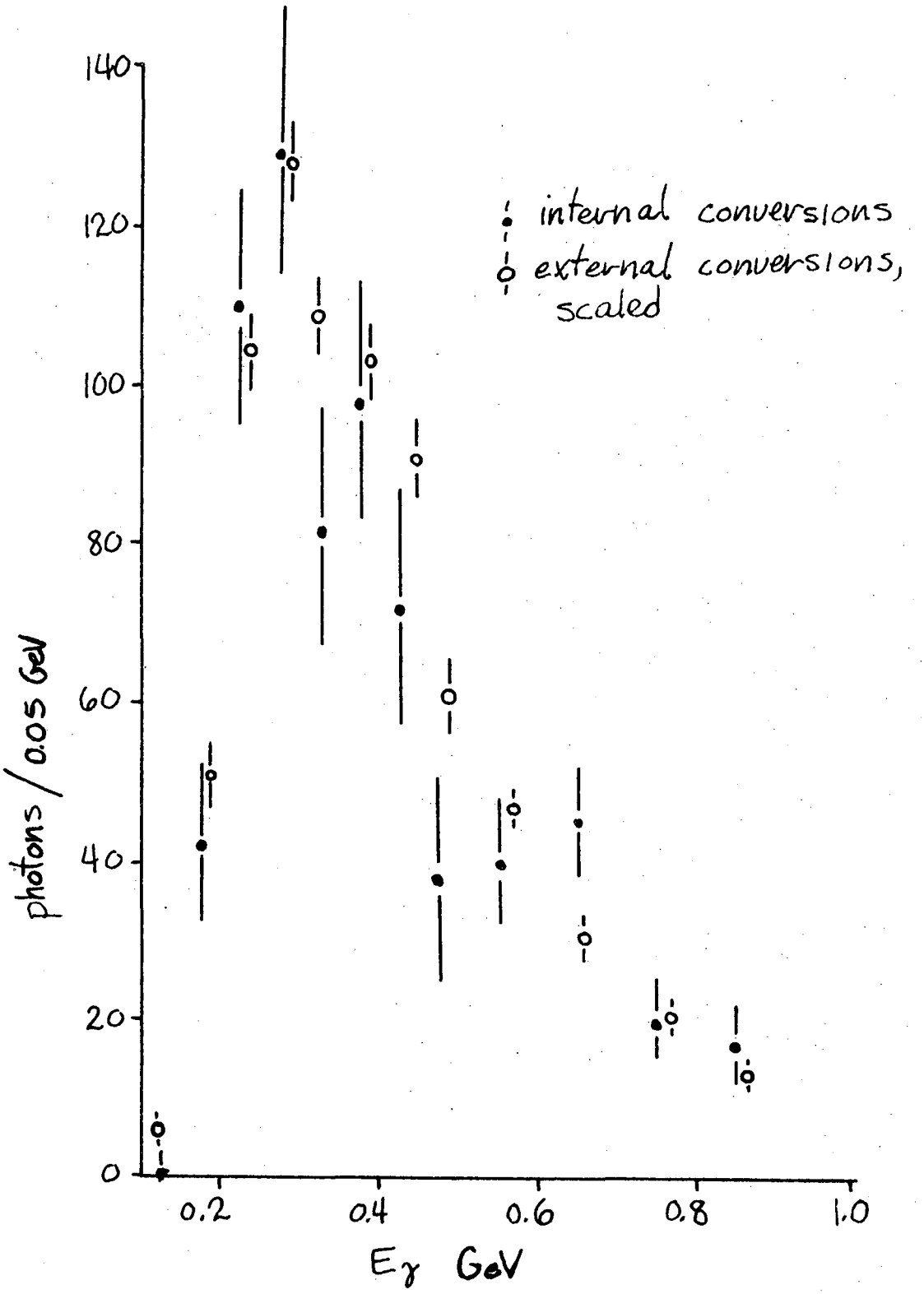

XBL 769-10474

Fig. 25. Internal and external conversions versus energy; the external conversions have been scaled by the ratio of the probabilities of internal and external conversion.

I. Monte-Carlo Checks

Performance of the detector was checked by comparing the experimental data with the predictions of a Monte-Carlo simulation of the detector and of hadronic events. The Monte-Carlo computer program, known as MADSIM, included all the known acceptance limits and inefficiencies of the magnetic detector. The measured TASH efficiencies, both for hadrons and for electrons from conversions, were input to the program. Photons were converted with the frequency calculated from Hubbell's results combined with the amount of converter present. Particle tracks were generated assuming 100% efficiency for tracks within the angular acceptance of the detector with transverse momentum greater than 55 MeV/c.

Hadronic events were generated according to several different models, the simplest of which was the all-pion phase space model. This model had two parameters: the average total particle multiplicity, from which a Poisson multiplicity distribution was generated, and the probability for a particle to be a π^o. Events were generated by selecting a multiplicity and assigning charges to the particles, conserving charge and rejecting all-neutral events (which violate charge conjugation). The particles were then boosted such that total momentum was conserved; the particles were distributed isotropically. Events were kept according to their phase-space weight in proportion to the maximum weight for that multiplicity. Events surviving this cut were propagated through the detector to generate an "observed" event reflecting the acceptance and efficiency of the detector. This simulated data was then analyzed using the same computer programs as for the experimental data.

The two-TASH hardware trigger requirement was also implemented in MADSIM; this trigger leads to observed multiplicity and momentum distributions which were quite different from the distributions of the "raw"

events before the administration of detector acceptance. The two parameters of the model were varied to get agreement between the experimental data and the simulated data on the mean charged particle multiplicity and the median charged particle momentum for events with three or more charged particles detected. For the ψ, the probability per particle of being neutral was fixed at 1/3 in keeping with the zero-isospin of the ψ. The value of ~ 6.2 for the total multiplicity parameter gave reasonable agreement with the data for the multiplicity and momentum distributions, raising hopes that the model would be a fair representation of the physical events.

This model is flawed, however, by the absence of heavy particles. Approximately 40% of ψ events contain a (charged or neutral) kaon and 7% of ψ events contain a nucleon. A model incorporating heavy particles was devised to examine the impact of the all-pion approximation. This model divided particles into three classes, each with four members: charged and neutral kaons, pions and etas, and nucleons (and antinucleons). The possible parameters proliferated. Arbitrarily, within the kaon class charged and neutral kaons were set to be equally probable, and in the nucleon class charged and neutral nucleons were made equally probable. In the pion/eta class, the probability of being a π^o was made the same as for being an η and was left as a parameter. There were then four parameters: the total multiplicity (as before), the probability of being in the kaon class, the probability of being in the nucleon class, and for particles in the π/η class the probability of being a π^o (or an η). Fortunately, the mean observed multiplicity and median momentum, to which the Monte Carlo was tuned, were sensitive mostly to the total multiplicity parameter and the parameter specifying the π^o/η probability; the kaon or nucleon parameters affected just the fraction of "observed"

events containing kaons or nucleons. Fit to the ψ data, the heavy particle model was much less efficient than the all-pion model; it produced 77 events per minute of computing time compared to 367 events per minute from the all-pion model.

Comparing detected photon conversions per event at ψ, with a $|\cos\theta_\gamma| < 0.6$ cut, the heavy particle model events contained 0.039 converted photons/event, compared to 0.048 photons/event from the pion model. The inclusive photon spectra from the two models were very similar in shape; the 19% drop in photon production in the heavy particle model was due to the increased fraction of total energy going into particle masses.

The ψ data contained, per hadronic event, 0.034 photon conversions with $|\cos\theta_\gamma| < 0.6$; this is 87% of the number from the heavy particle model (and 71% of the number from the pion model). The Monte-Carlo calculation did not include secondary interactions by the electron or positron after conversion; as mentioned previously, an average of $\sim 6\%$ of the photon conversions will not be detected because one of the particles has a secondary interaction and drops below the 55 MeV/c transverse momentum threshold. Correcting for this, the photon yield in the data is 93% of the value predicted by Monte-Carlo calculation with the heavy particle model.

Due to the relative inefficiency of the heavy particle model, the pion model was used to generate a data sample of ~ 92000 hadronic events; the inclusive photon spectrum from these events is shown in Fig. 26. The curve in Fig. 26 is a smoothed representation of the Monte-Carlo data. The smoothing was done by fitting a line through seven consecutive points to determine a value for the middle point; this smoothing was iterated twice to even out the statistical variation of

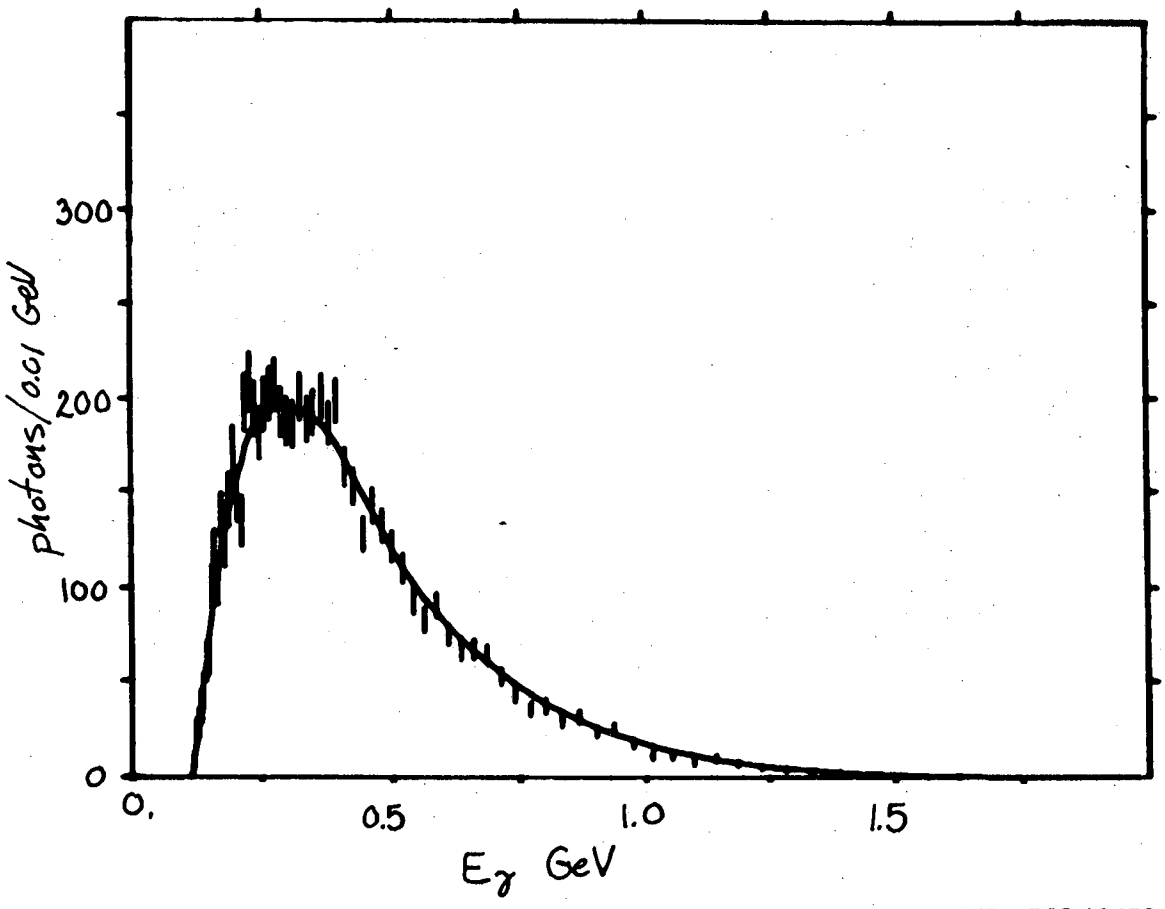

Fig. 26. The inclusive photon spectrum, with $|\cos\theta_\gamma| < 0.6$, taken from Monte-Carlo simulation of ψ events. The line is a smoothed version of this spectrum which was overlayed on the ψ spectrum in Fig. 20.

the data. As was shown in Fig. 20, the smoothed Monte-Carlo spectrum agrees quite well with the data. (Recall that the Monte-Carlo spectrum was normalized to the data in the 300 - 350 MeV region.) The deficit of photons below $\sim$ 200 MeV relative to the Monte-Carlo prediction is partly due to the radiative losses mentioned earlier and may reflect also some inefficiency for finding low momentum tracks. The excess of high energy photons in the data over the Monte Carlo is due to the presence in the data of high energy electrons from $\psi \to e^+e^-$ and from the QED $e^+e^- \to e^+e^-$ events. These high energy electrons may form a high energy "conversion pair" with a knock-on electron from the converter or with a particle from a converted bremstrahlung photon. Since the Monte Carlo models only the hadronic decays of ψ, such effects are missing from the simulated data. There may also be aspects of ψ decays which may not be well-represented by the Monte-Carlo model; for example, it has been suggested there may be decays $\psi \to \gamma$ + hadrons where the photon spectrum would rise with energy.[30,31]

Monte-Carlo simulation of ψ' events suffers the complication of the $\psi' \to \psi$ + anything cascade decays. The decay $\psi' \to \pi^o\pi^o\psi$ has $\sim$ 16% branching ratio and will contribute photons in roughly the 50 - 450 MeV region. To see the impact of this decay mode on the inclusive photon spectrum it would be necessary to use the heavy particle model to simulate both direct ψ' decays and the decay of cascade ψ events, since the branching ratio for $\psi' \to \pi^o\pi^o\psi$ is of the order of the difference in photon production by the heavy particle model and the pion model. However, running the heavy particle model long enough to generate a Monte-Carlo sample statistically comparable to the data would require approximately 100 hours of computer time. In addition, there would be severe problems with fitting a model for ψ' decays in the presence of the ψ

decays -- both hadronic and leptonic.

After such contortions the reliability of the Monte-Carlo prediction would be unclear. A shortcut to equally reliable results is to simply use the spectrum from the ψ simulation. Figure 27 shows the ψ' inclusive photon spectrum with the $|\cos\theta_\gamma| < 0.6$ cut overlaid with the smoothed ψ pion model spectrum; the Monte Carlo has been normalized to the data in the 300 - 350 MeV region. With this normalization, the data show a deficiency relative to the simulation for energies above $\sim$ 500 MeV. Alternatively, normalizing the Monte-Carlo spectrum to the data in the 500 - 750 MeV region yields the results shown in Fig. 28. Here there is an apparent excess of photons in the region below 500 MeV, as expected due to both $\psi' \to \pi^o\pi^o\psi$ decays and $\psi' \to \gamma X$, $X \to \gamma\psi$ events (to be discussed in detail in the next Chapter). Believing that local normalization would be best to estimate the rapidly rising spectrum in the region below 250 MeV, the background to the peak in the ψ' spectrum was estimated using the ψ Monte-Carlo results normalized to the ψ' data in the 300 - 350 MeV region (as will be discussed in the next Chapter, $\psi' \to \gamma X$, $X \to \gamma\psi$ events contribute very little in this restricted region).

To summarize these checks on the detector and on the analysis, comparison of internal and external conversions indicate that photon conversions occur with the expected rate within $\sim$ 20% uncertainty, and Monte-Carlo simulations of ψ events show good agreement with the data both in spectral shape and in rate, once the presence of heavy particles is taken into account. Since ψ and ψ' data were collected in intermixed runs, this implies a check on the ψ' data as well. Comparison of ψ Monte-Carlo results with the ψ' spectrum show the expected "excess" of photons in the region below $\sim$ 500 MeV; normalizing the

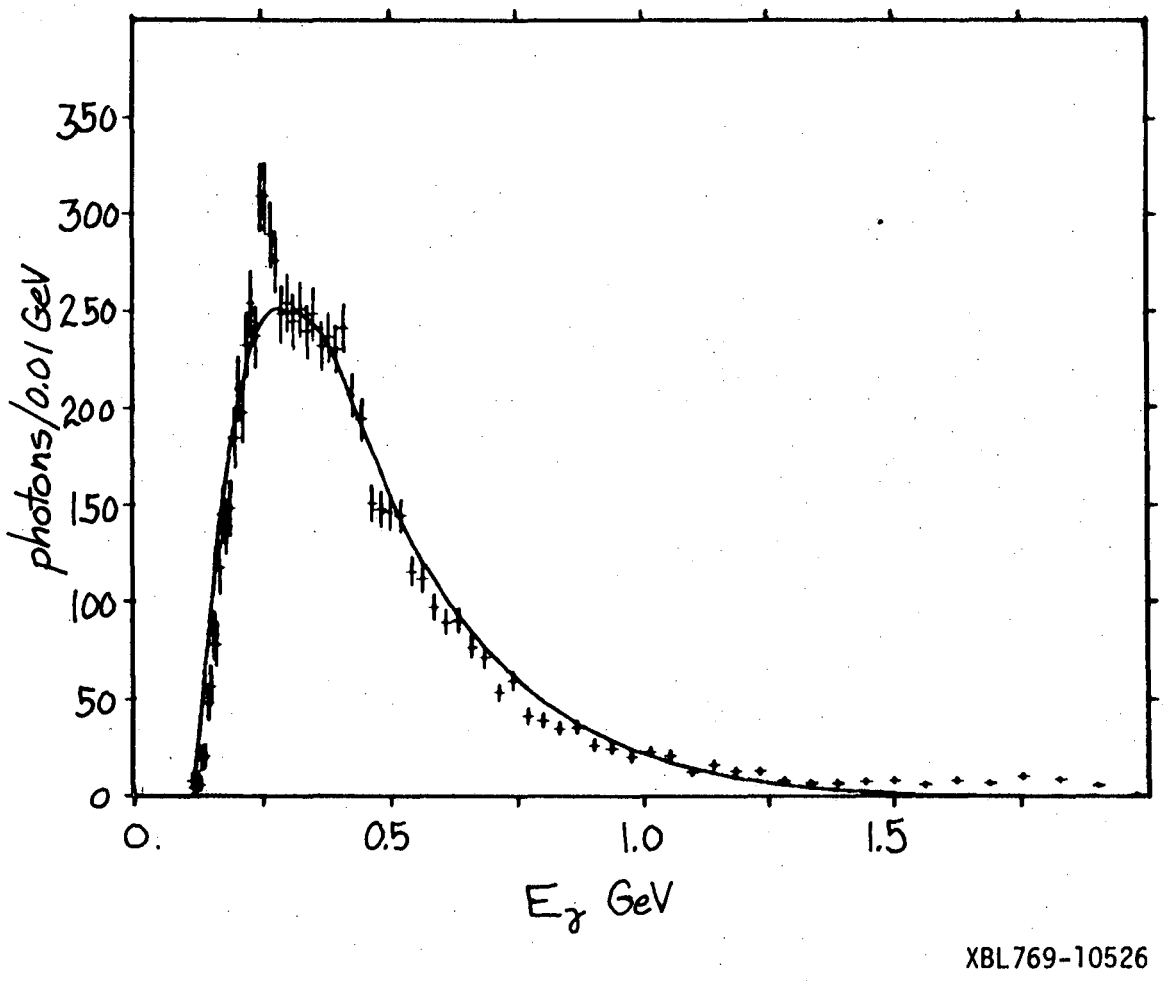

Fig. 27. The ψ' inclusive photon spectrum overlayed with the smoothed Monte-Carlo ψ spectrum normalized to the data in the 300 - 350 MeV region.

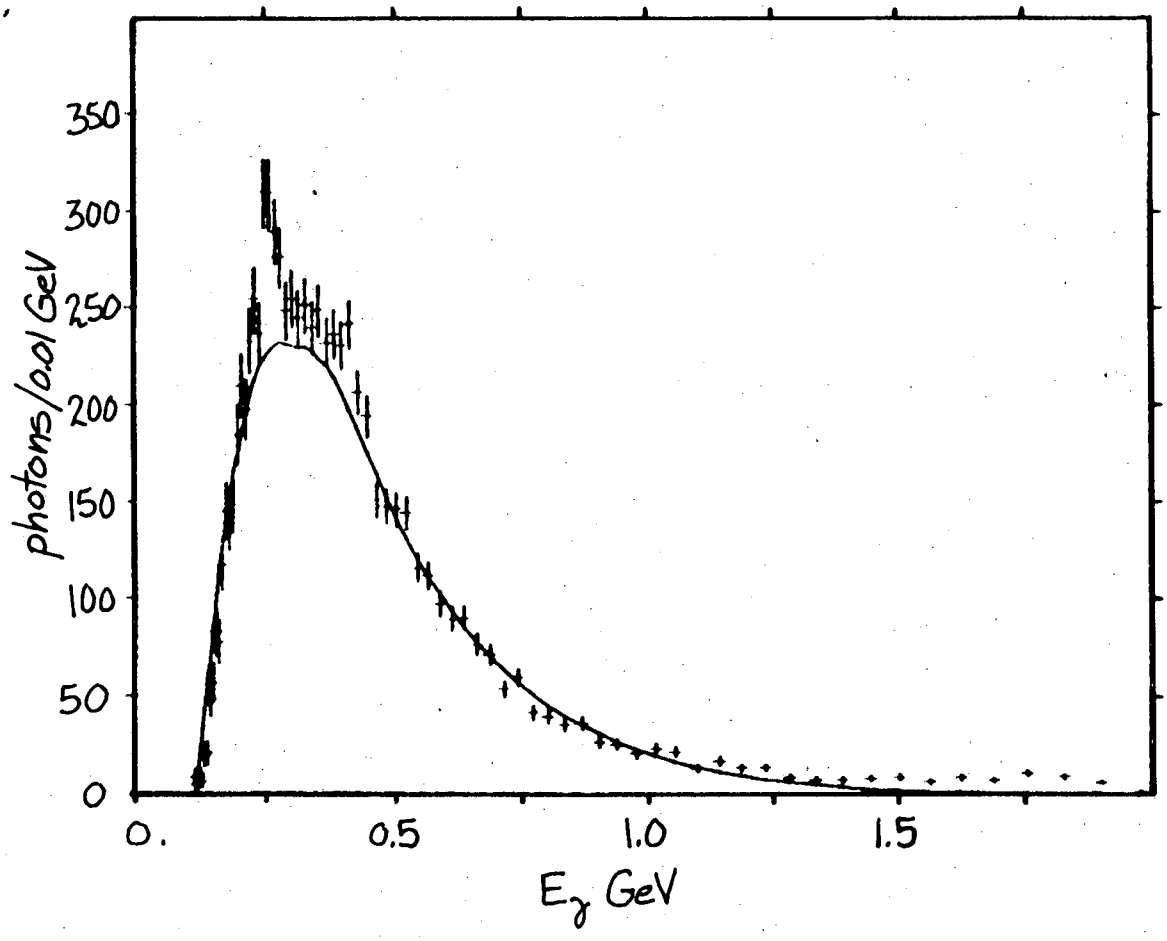

Fig. 28. The ψ' inclusive photon spectrum overlayed with the smoothed Monte-Carlo ψ spectrum normalized to the data in the 500 - 750 MeV region.

Monte Carlo to the data in the 300 - 350 MeV region gives a reasonable estimate of the background to the $\chi(3415)$ peak with $< 20\%$ uncertainty.

J. Branching Fraction Limits

Now that the credibility of the data has been established, let us return to the issue of peaks in the inclusive photon spectra. Other than the line for the $\psi' \to \gamma\chi(3415)$ decay, there are no clear monochromatic signals in the ψ or ψ' spectra. Before considering upper limits for possible signals, it is useful to review the kinematics of the transitions from ψ' to some intermediate state χ and from χ to ψ. For a state χ of mass m_χ the photon from $\psi' \to \gamma\chi$ will have energy $E_{\gamma 1} = (m^2_{\psi'} - m^2_\chi)/2m_{\psi'}$; the photons from $\chi \to \gamma\psi$ will have mean energy $E^*_{\gamma 2} = (m^2_\chi - m^2_\psi)/2m_\chi$, but due to the motion of the χ state in the laboratory frame the photons will be distributed from $(\frac{1-\beta}{1+\beta})^{1/2} \times E^*_{\gamma 2}$ to $(\frac{1+\beta}{1-\beta})^{1/2} \times E^*_{\gamma 2}$, where the Doppler factor $(\frac{1-\beta}{1+\beta})^{1/2} = [1 - (2E_{\gamma 1}/m_{\psi'})]^{1/2}$. Table II below gives values of $E_{\gamma 1}$ and $E_{\gamma 2}$ for the states observed in hadronic channels and in the $\psi' \to \gamma\gamma\psi$ channel (see Chapter VI concerning the possible state at 3455 MeV or 3340 MeV).

Table II

m_χ GeV	$E_{\gamma 1}$ GeV	$E^*_{\gamma 2}$ GeV	Range of $E_{\gamma 2}$ GeV
3.550	0.131	0.426	0.410 - 0.442
3.500	0.179	0.381	0.362 - 0.402
3.415	0.259	0.305	0.283 - 0.329
3.455	0.231	0.332	0.311 - 0.355
or 3.340	0.328	0.236	0.214 - 0.260

As is clear from Table II the Doppler-broadened second photons in the cascade $\psi' \rightarrow \gamma\gamma\psi$ decays will be more than doubled in expected width and, considering the resolution, will be merged together. Thus monochromatic limits will not apply for the cascade decays.

To calculate the upper limits for branching fractions for monochromatic signals, the number of signal events in the branching ratio calculation is replaced by the excess over the smooth background plus twice the error on total number within a FWHM photon energy resolution. Allowing for the $\sim$ 30% estimated systematic errors, these limits should be interpreted as 90% confidence level upper limits. Table III below gives the 90% CL upper limits for branching fractions for monochromatic signals, separated from other signals by at least the FWHM photon energy resolution, for representative energies above 250 MeV at ψ and ψ'.

Table III. 90% confidence level branching fraction limits for monochromatic photon production above 0.250 GeV at ψ and ψ'.

ψ		ψ'	
E_γ (GeV)	Limit	E_γ (GeV)	Limit
0.26	0.039	0.40	0.028*
0.37	0.038	0.50	0.022
0.51	0.024	0.74	0.011
0.80	0.014	1.05	0.010
1.10	0.008		

*Limit for a narrow peak. See text for a discussion of complications due to the cascade photons.

Below 250 MeV, the small and rapidly varying photon detection efficiency makes recognition of a monochromatic signal difficult and dubious. This difficulty is compounded by the poor energy resolution for low energy photons. Unfortunately, the photons for transitions from ψ' to $\chi(3550)$, $\chi(3500)$, and the possible state at 3455 MeV or 3340 MeV are below this threshold and are not accessible to study by this method.

The 90% CL branching fraction limits presented here are somewhat smaller than the 99% CL limits published by the HEPL Group[32,33]; the branching ratio of 7.5% for $\psi' \rightarrow \gamma\chi(3415)$ is larger than the HEPL limit of $\sim 6\%$ for that photon energy range. Recently the Maryland-Princeton-Pavia-San Diego-Stanford-SLAC collaboration (SP-27) at SPEAR has confirmed the effect described here. Their preliminary value[34] of $8 \pm 3\%$ is in good agreement with the data presented here.

VI. $\psi' \to \gamma\gamma\psi$

States of even charge conjugation intermediate in mass to ψ and ψ' may be produced in radiative decays of ψ' and may decay radiatively to ψ. In the simple charmonium model, in fact, the $1^3P_{0,1,2}$ states were expected to decay dominantly to $\gamma\psi$.[8] Peaks in the $\psi\gamma$ mass distribution from $\psi' \to \gamma\gamma\psi$ events may reveal the presence of new states. Earlier results of a similar analysis have been published.[35] The results presented in this Chapter draw extensively on the work of Bill Tanenbaum.

Photon conversions enable us to identify $\psi' \to \gamma\gamma\psi$ events, where one of the photons converts and the ψ is detected by its lepton pair decay. Photon conversions are selected with the same criteria as in Chapter V; background from $\psi' \to \pi^+\pi^-\psi$ events where the $\pi^+\pi^-$ simulate a converted photon is negligible, since the $\pi^+\pi^-$ mass peaks strongly at large values.[36] The ψ is identified by its lepton pair decay; the observed lepton pair mass is required to lie between 2.97 and 3.22 GeV and is then constrained to the ψ mass. Two cuts are applied to reduce the background from $\psi' \to e^+e^-$ or the QED process $e^+e^- \to e^+e^-$ where one of the electrons radiates a photon: first, electron pair events are rejected when the angle between the energetic electron and positron is greater than 177.5°, eliminating more than 95% of the radiative background but only $\sim 8\%$ of real $\psi' \to \gamma\gamma\psi$, $\psi \to e^+e^-$ events; second, events were rejected if the converted photon was collinear within 10° with one of the leptons -- five events were rejected with this cut.

Figure 29 shows the missing-mass-squared, M_x^2, recoiling against the $\psi\gamma$ system for the 54 events surviving the selection cuts. There is a peak at zero M_x^2 corresponding to true $\psi' \to \gamma\gamma\psi$ events and a broad background from $\psi' \to \pi^o\pi^o\psi$ where a photon from a π^o converted. Under

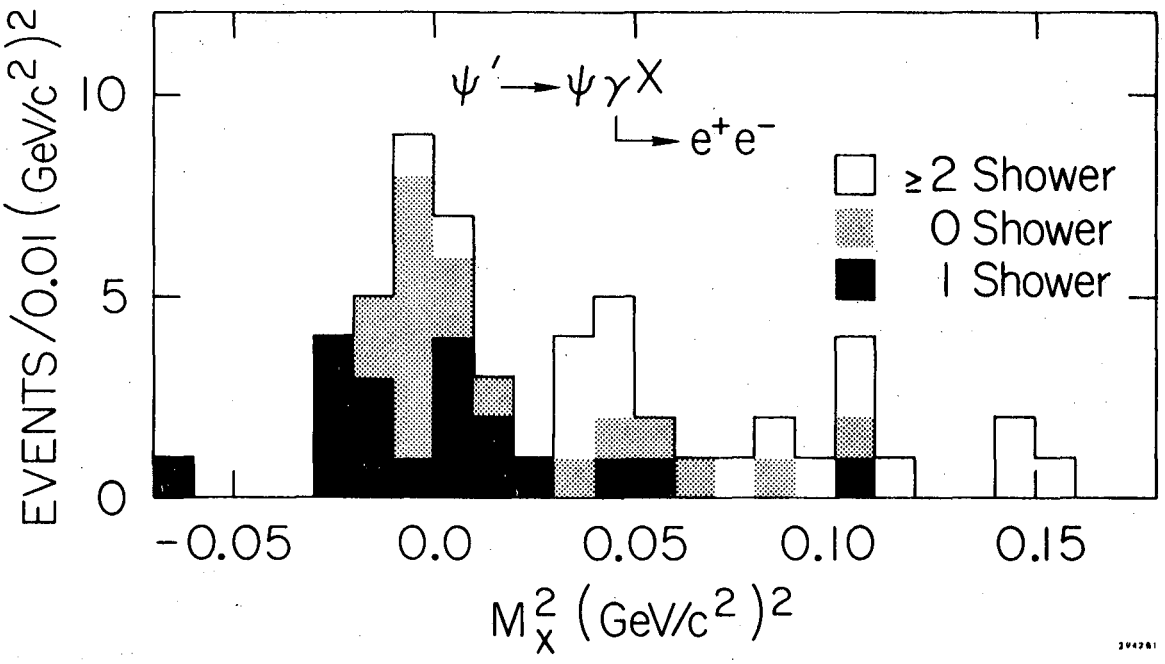

Fig. 29. The missing-mass-squared recoiling against $\psi\gamma$ in $\psi\gamma\gamma$ candidates with one photon converted. The shading is discussed in the text.

the hypothesis of $\psi' \to \gamma\gamma\psi$, the direction of the missing photon may be predicted from the observed photon and the ψ. Additional photons may be detected in the 24 shower counters, which cover $\sim 65\%$ of the solid angle and have resolution of $\sim 10^{\circ}$ in azimuthal angle. The shading in Fig. 29 flags the detection of additional photons in the shower counters: darkly shaded events have a shower counter signal consistent with the missing photon direction assuming a $\gamma\gamma\psi$ decay, lightly shaded events have no additional photons detected, and unshaded events have one or more photons detected in counters inconsistent with the $\psi\gamma\gamma$ hypothesis (as expected for $\psi' \to \pi^{\circ}\pi^{\circ}\psi$ events). The high correlation of shading with small M_x^2 corroborates the identification of events with small M_x^2 as $\psi' \to \gamma\gamma\psi$ events.

The 27 shaded events with $-0.03\,(\mathrm{GeV}/c^2)^2 < M_x^2 < 0.03\,(\mathrm{GeV}/c^2)^2$ are kept. The unconverted photon is detected in 15 of these events, consistent with the shower counter acceptance and efficiency. Figure 30 shows the missing-mass-squared M_x^2 recoiling against the ψ for these 27 events and also for 3 and 4 prong events in which a ψ was detected -- dominantly $\psi' \to \pi^+\pi^-\psi$. The M_x^2 distribution for the 3 and 4 prong events peaks at high values, indicating the distribution expected for $\psi' \to \pi^{\circ}\pi^{\circ}\psi$ events. In contrast, the 27 candidates for $\psi' \to \gamma\gamma\psi$ have a roughly flat M_x^2 distribution, as expected for radiative cascades through an intermediate state.[40] Six events with $M_x^2 > 0.27\,(\mathrm{GeV}/c^2)^2$ are removed as possible $\psi' \to \psi\eta$, $\eta \to \gamma\gamma$ events (four such events are expected).

The remaining 21 events are constrained to fit the reaction $\psi' \to \gamma\gamma\psi$. There are two values for the $\psi\gamma$ mass for each event; these are plotted against one another in Fig. 31. The shaded events have the unconverted photon detected in the proper shower counter. The expected

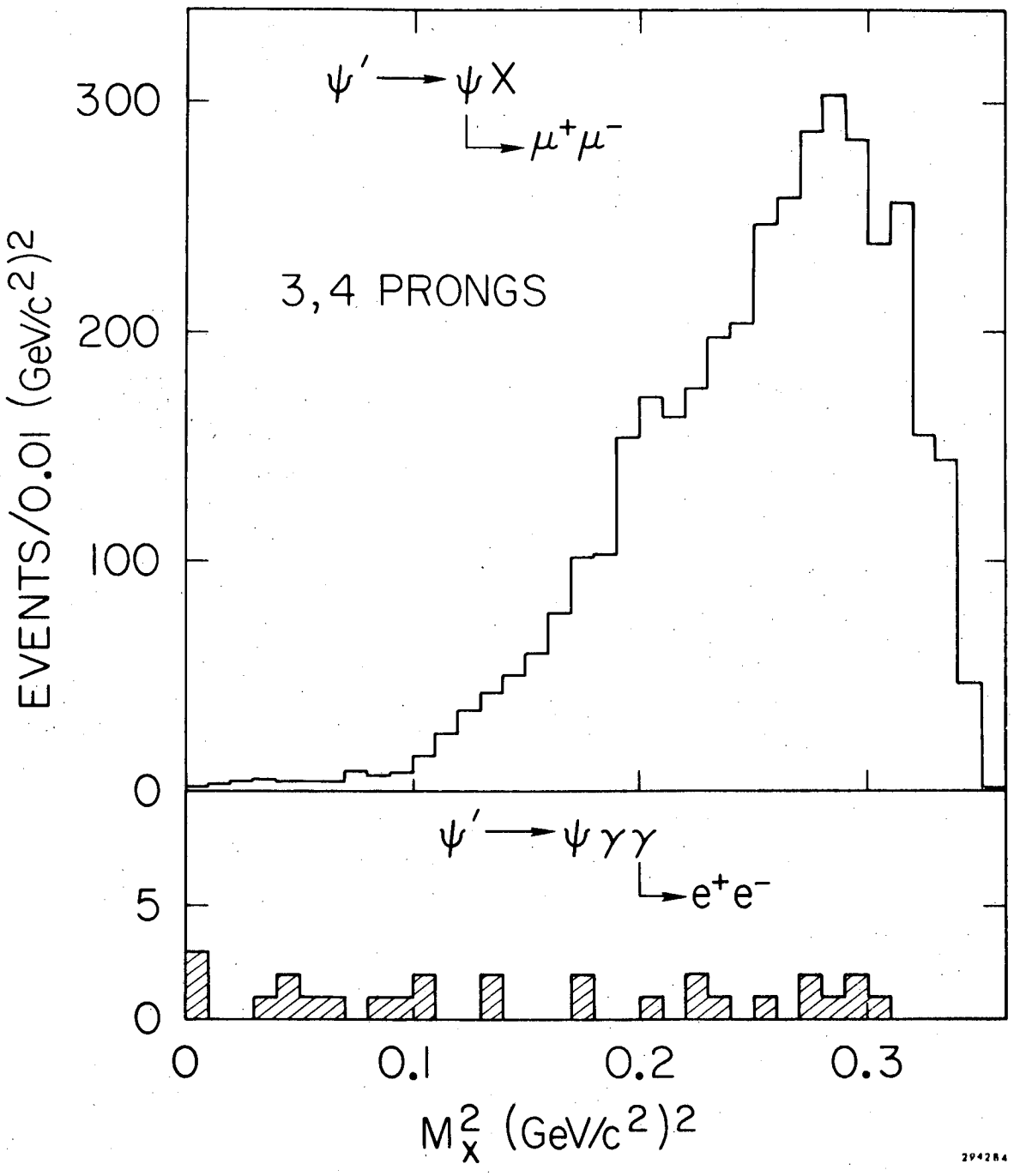

Fig. 30. Missing-mass-squared recoiling against the ψ for the 27 $\psi\gamma\gamma$ events and also for 3 and 4 prong events in which a ψ was detected.

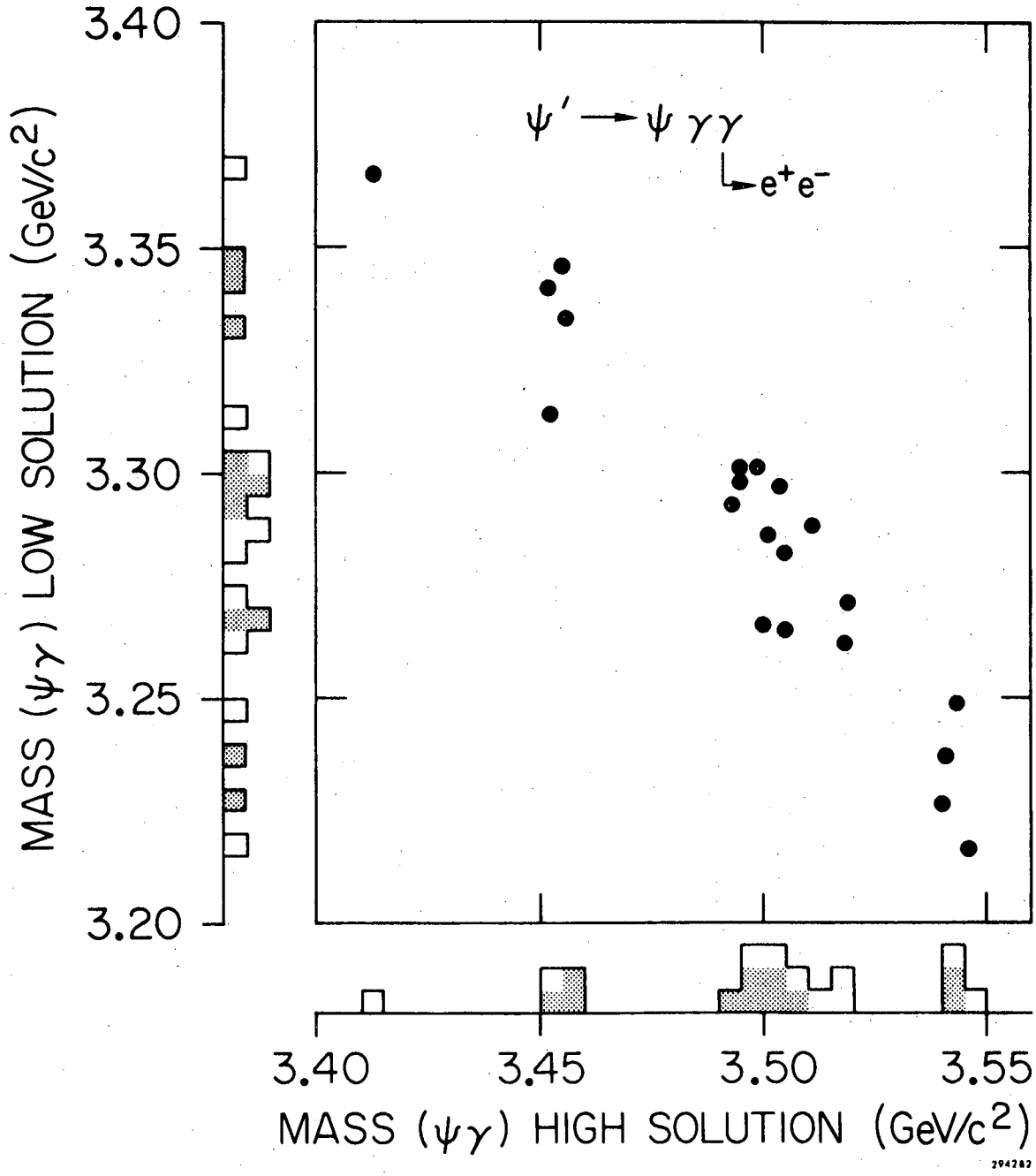

Fig. 31. Diplot of the two solutions for $\psi\gamma$ masses from 21 $\psi\gamma\gamma$ events.

background is one event.

There are three main clusters of events in Fig. 31. The mass spread of the high mass projection of each of these clusters is consistent with the expected rms resolution of ~ 8 MeV; the masses of the three corresponding states are 3543 ± 10 MeV, 3504 ± 10 MeV, and 3454 ± 10 MeV. The mass spread of the low mass projections of each of the clusters is consistent with the expected Doppler-broadened resolution of ~ 14 MeV; each cluster has a confidence level of $\lesssim 0.025$ for the low mass projection assuming the 8 MeV unbroadened resolution. However, the events at 3454 MeV could be explained by a state at 3340 MeV with three events and one event background. The states $\chi(3545)$ and $\chi(3505)$ can be identified with states observed through hadronic decays; there is no evidence in hadronic channels for a state at 3455 MeV or 3340 MeV (see Chapter VII). The single event at 3413 MeV is either from the $\chi(3415)$ or a background event.

Correcting for ψ branching ratios and the photon detection efficiency, branching ratio products for $\psi' \to \gamma\chi$, $\chi \to \gamma\psi$ can be calculated. The photon detection efficiency was calculated assuming full efficiency to $|\cos\theta_\gamma| \sim 0.65$ to use the full sample of $\psi\gamma\gamma$ events; the number of events with $|\cos\theta_\gamma| > 0.6$ was consistent with the photon detection efficiency calculated using a 0.65 $\cos\theta_\gamma$ cutoff compared to a 0.60 cutoff. The branching ratio products for $\psi' \to \gamma\chi$, $\chi \to \gamma\psi$ are $0.8 \pm 0.4\%$, $2.4 \pm 0.8\%$, and $1.0 \pm 0.6\%$ for $\chi(3455)$, $\chi(3505)$, and $\chi(3545)$ respectively -- all four events have been counted in the $\chi(3455)$. Taking the event at ~ 3415 MeV in the high mass projection as signal, the branching ratio product for $\chi(3415)$ is $0.2 \pm 0.2\%$.

VII. CONCLUSIONS

These three approaches to the study of radiative decays yield complementary information. The states $\chi(3505)$ and $\chi(3550)$ are observed both in hadronic channels and by their decays to $\gamma\psi$; the $\chi(3415)$ is seen in hadronic decays and in the inclusive photon spectrum. There is, however, no corroborating evidence for the state at either 3340 MeV or 3455 MeV observed in the $\gamma\gamma\psi$ events. In the inclusive photon spectrum the line for the transition to a state at 3455 MeV falls at 222 MeV, too low to be studied by this method; a state at 3340 MeV corresponds to a photon energy of 328 MeV, for which there is a branching fraction limit of $\sim 3\%$. In the study of hadronic decays, 90% confidence level upper limits for branching ratio products are 4, 5, 7, and 3×10^{-4} for $\psi' \to \gamma\chi(3340 \text{ or } 3455)$, $\chi \to \pi^+\pi^-\pi^+\pi^-$, $\pi^+\pi^-K^+K^-$, $\pi^+\pi^-\pi^+\pi^-\pi^+\pi^-$, and $\pi^+\pi^-$ or K^+K^- respectively. Apparently, the decay to $\gamma\psi$ must be a dominant decay mode for this state.

Counting the $\chi(3340 \text{ or } 3455)$, the number of states observed between ψ and ψ' agrees with the charmonium model prediction. The favored charmonium model quantum number assignments of 0^+, 1^+, and 2^+ for the $\chi(3415)$, $\chi(3505)$, and $\chi(3550)$ respectively find some support in the relative populations in the clusters in the $\gamma\gamma\psi$ events: the 1^+ state, forbidden to decay to hadrons via two massless vector gluons, is expected to have a higher branching fraction to $\gamma\psi$ as is observed for the $\chi(3505)$ (assuming roughly equal production of the $^3P_{0,1,2}$ states -- see footnote 13 of Ref. 11).

However, the simple charmonium model is hard-pressed to accommodate the mass splittings of the χ states.[11,37] Interpreting the $\chi(3340)$ or 3455) as the pseudoscalar companion of ψ or ψ', this state should decay dominantly to hadrons, contrary to observation. The charmonium model

predictions for partial widths for radiative decays are somewhat off: the predicted partial width for $\psi' \to \gamma X(3415)$ is 28 - 36 keV,[11] a factor of two greater than observed. In addition, the upper limit for transitions from ψ' to the (η_c) pseudoscalar companion to ψ is one-fourth the predicted value for this magnetic dipole transition (assuming this state lies near ψ).[11] But then, considering the difficulty of the calculation, a factor two discrepancy isn't all that bad.

In regard to the η_c, the DASP and DESY-Heidelberg experiments at DESY have reported evidence for a state X with mass 2.85 ± 0.05 GeV, produced in radiative decays of ψ and decaying to $\gamma\gamma$ with a branching fraction product upper limit of 1.6×10^{-4}.[38,39] Unfortunately, this mass range flirts with the credibility threshold for observation of monochromatic photon signals in the γ inclusive photon spectrum, corresponding to $189 \text{ MeV} < E_\gamma < 281 \text{ MeV}$. The $\gamma\gamma$ decay of η_c is expected to have a small branching fraction, due to competing hadronic decays. Either the X lies in the higher end of the quoted mass range, or the branching fraction for $X \to \gamma\gamma$ is quite a bit higher than anticipated -- or both of the above. As shown in Table III, we can quote 90% CL branching fraction upper limits for $\psi \to \gamma X$ of $< 4\%$ if the mass of X is less than 2.83 GeV.

The absence of high energy monochromatic signals in the ψ' inclusive spectrum refutes Harari's interpretation[12] of ψ and ψ' as bound states of three new quarks -- in that model, transitions from ψ' to a pseudoscalar state near ψ are expected with considerable branching fraction.

With a value of the branching fraction for $\psi' \to \gamma X(3415)$, it is possible to calculate branching fractions for X(3415) decay. These are 0.043 ± 0.017, 0.019 ± 0.009, and 0.036 ± 0.016 for the $4\pi^\pm$, $6\pi^\pm$, and $2\pi^\pm 2K^\pm$ channels respectively. The $4\pi^\pm$ and $6\pi^\pm$ branching fractions are quite

commensurate with the (G-parity allowed) $4\pi^{\pm}\pi^{o}$ and $6\pi^{\pm}\pi^{o}$ decays of ψ, which occur with branching fractions of 0.040 ± 0.010 and 0.029 ± 0.007.[40] The $2\pi^{\pm}2K^{\pm}$ decay mode is allowed for both the $\chi(3415)$ and the ψ. In the case of $\chi(3415)$ it occurs with approximately the same rate as the $4\pi^{\pm}$ decay; in the case of ψ, it occurs with a branching fraction of 0.004 ± 0.002, equal to the rate of the G-parity-forbidden $4\pi^{\pm}$ decay and one-tenth the rate of the allowed $4\pi^{\pm}\pi^{o}$ mode.[41] (The $4\pi^{\pm}$ decays of ψ occur through an intermediate photon.) This difference in $2\pi^{\pm}2K^{\pm}$ rates for the $\chi(3415)$ and ψ may reflect the SU(3) structure of these mesons.

The 7.5% branching fraction for $\psi' \rightarrow \gamma\chi(3415)$ accounts for one-fourth of the $\sim$ 30% unexplained decays of ψ'. The branching fractions for decays of ψ' to the $^3P_{0,1,2}$ states in the charmonium model are expected to be roughly equal, the $(2J+1)$ statistical weighting compensating the $(E_\gamma)^3$ phase space (although the presence nearby of the charmed meson threshold may reduce the rates for the higher-mass P states[11]). The sum of the branching fractions for radiative decays of ψ' may account for a substantial fraction of the missing 30% of ψ' decays.

APPENDIX A: SHOWER COUNTER EFFICIENCY

The shower counters were included in the hardware trigger requirement in order to suppress triggers on low energy background. This led to the introduction of a momentum bias in triggering and to the necessity for a correction due to shower counter inefficiencies. Two types of efficiency are important; for high energy minimum ionizing particles, such as μ pairs, the shower counter inefficiency is due to losses in counter edges and by loss of the light through attenuation. This efficiency was measured using high energy cosmic rays as a source of minimum-ionizing particles. Cosmic ray data were collected during special runs where the shower counters were removed from the hardware trigger requirement. The shower counter efficiency was then determined simply according to whether the counter struck by a cosmic ray was latched or not. Figure A1 shows the shower counter efficiency as a function of the z position at which the particle struck the counter, averaging over all 24 shower counters. Figure A2 shows the shower counter efficiency versus z for cosmic rays hitting within the $\pm$ 45% of a counter width from the center in azimuthal position -- that is, cosmic rays striking near the azimuthal edges of the counters were not used. These two plots show a clear z dependence, due to the attenuation of the scintillation light, and a correlation of inefficiency with the azimuthal edges. This last effect is clearer in Fig. A3, which plots shower counter efficiency versus azimuthal position in the shower counter; data from all 24 counters have been folded together and cosmic rays with z position in the shower counter $< \pm$ 1.5 meters were used. The loss at the edges is dramatic; interpreting the drop in efficiency at the edges as complete inefficiency over some region of thickness Δ at each edge and $\sim$ 100% efficiency elsewhere implies $\Delta \cong 0.28$ inches, consistent with the expected

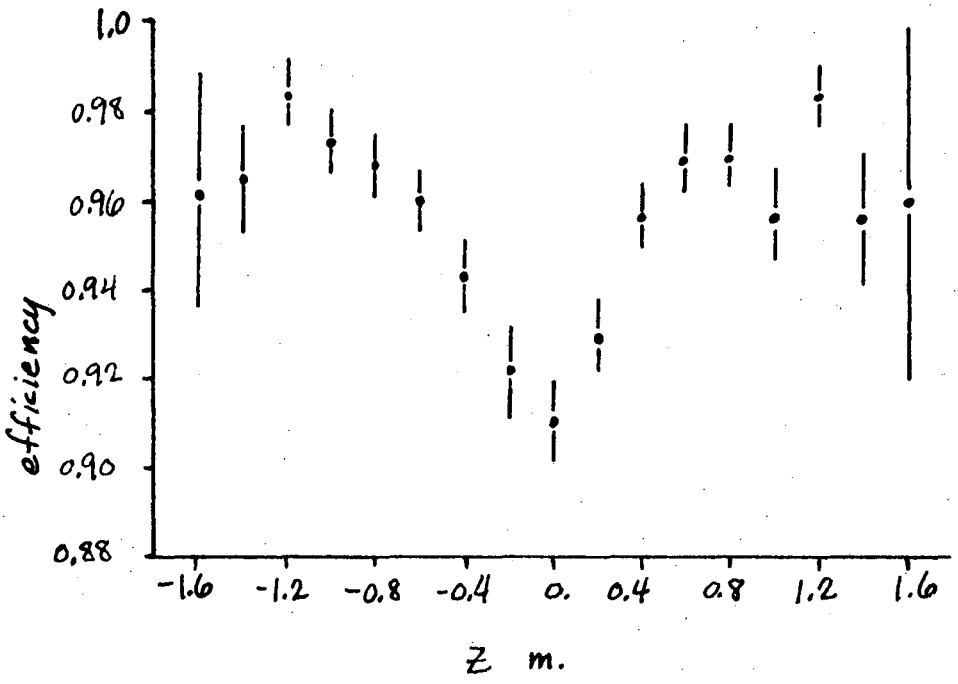

Fig. A1. Shower counter cosmic ray efficiency versus z, for the full counter width.

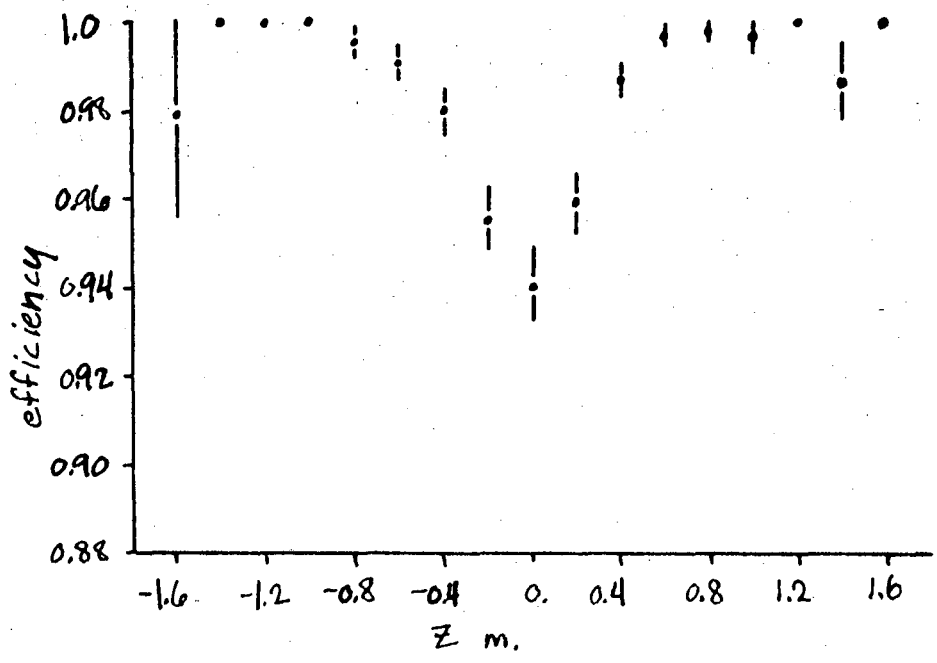

XBL 769-10475

Fig. A2. Shower counter cosmic ray efficiency versus z, excluding 5% of the counter width at each azimuthal edge.

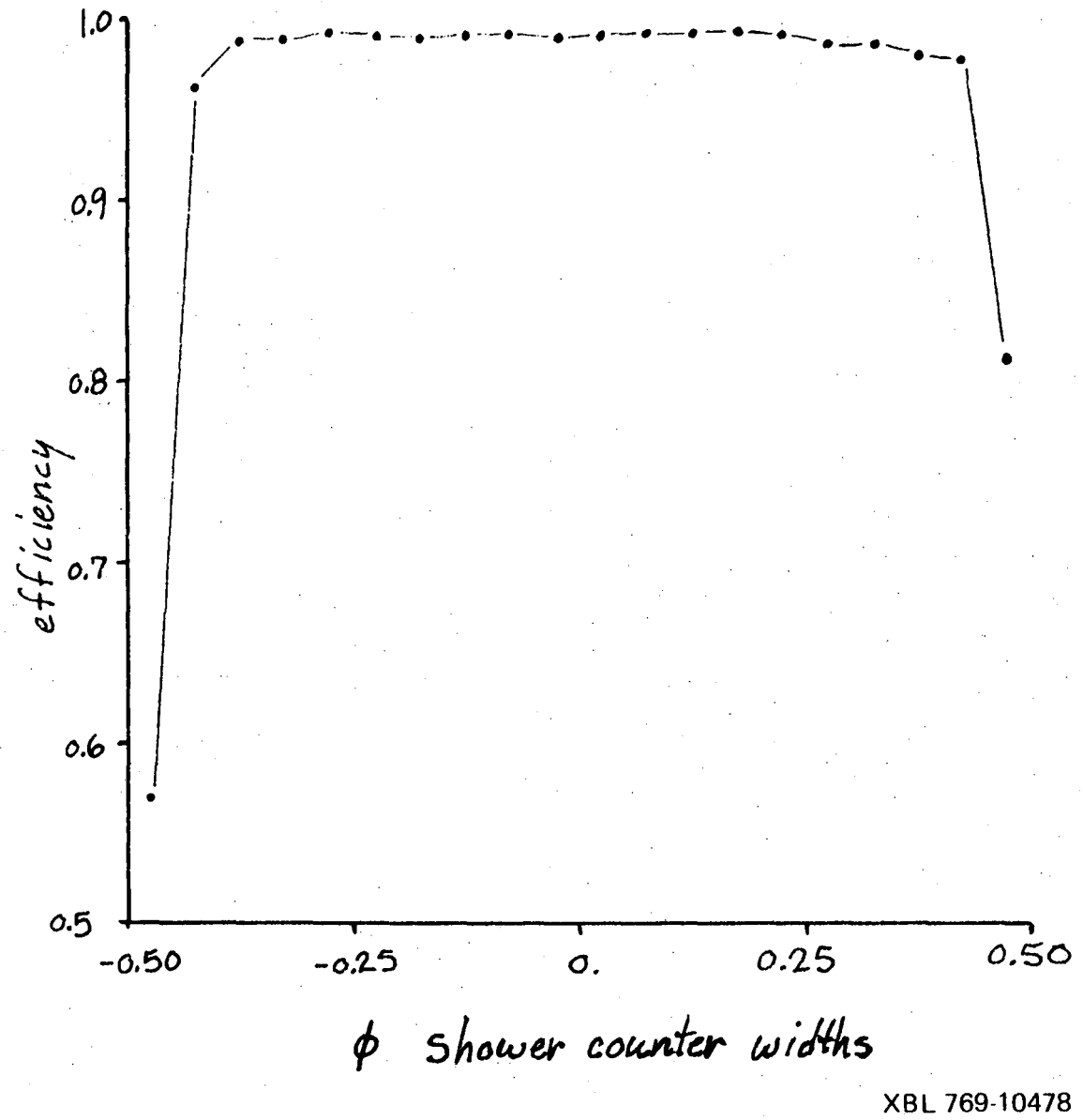

Fig. A3. Shower counter cosmic ray efficiency versus azimuthal position on the counter.

dead region due to the walls of the counters. If the difference in the high-φ and low-φ edge inefficiencies is ascribed to a rotation of the cylinder of shower counters relative to the coordinate system of the spark chambers, so that the wrong counter is sometimes interrogated, then this rotation is $\sim 0.1^{\circ}$.

The hadronic prongs of multihadron events have a different kind of shower counter inefficiency. Low momentum particles can range out in the ~ 1 radiation length thick solenoid; low or high momentum hadrons may interact before reaching the shower counters and be back-scattered or stopped. Thus it was necessary to measure the shower counter efficiency for hadrons as a function of momentum. Specifically, the important quantity was the TASH efficiency, where a TASH is defined in the trigger hardware as the latching of the trigger counter and one or both of the two closest shower counters. The TASH efficiency was measured from the data, using the following algorithm to correct for the two-TASH hardware requirement:

(1) events with three or more prongs were used;

(2) events where two or more particles struck the same counters or would use the same counters in a TASH were excluded;

(3) in events where only two particles had TASH's, particles without TASH's were tallied as inefficient;

(4) in events where three or more particles had TASH's, each particle with a TASH was counted as efficient and each particle without a TASH was counted as inefficient.

The TASH efficiency as a function of momentum for all prongs in multiparticle events is plotted in Fig. A4. The arrow in Fig. A4 marks the accidental TASH rate; this was measured by looking at the latching rate for shower counters far from any charged particles and assuming the

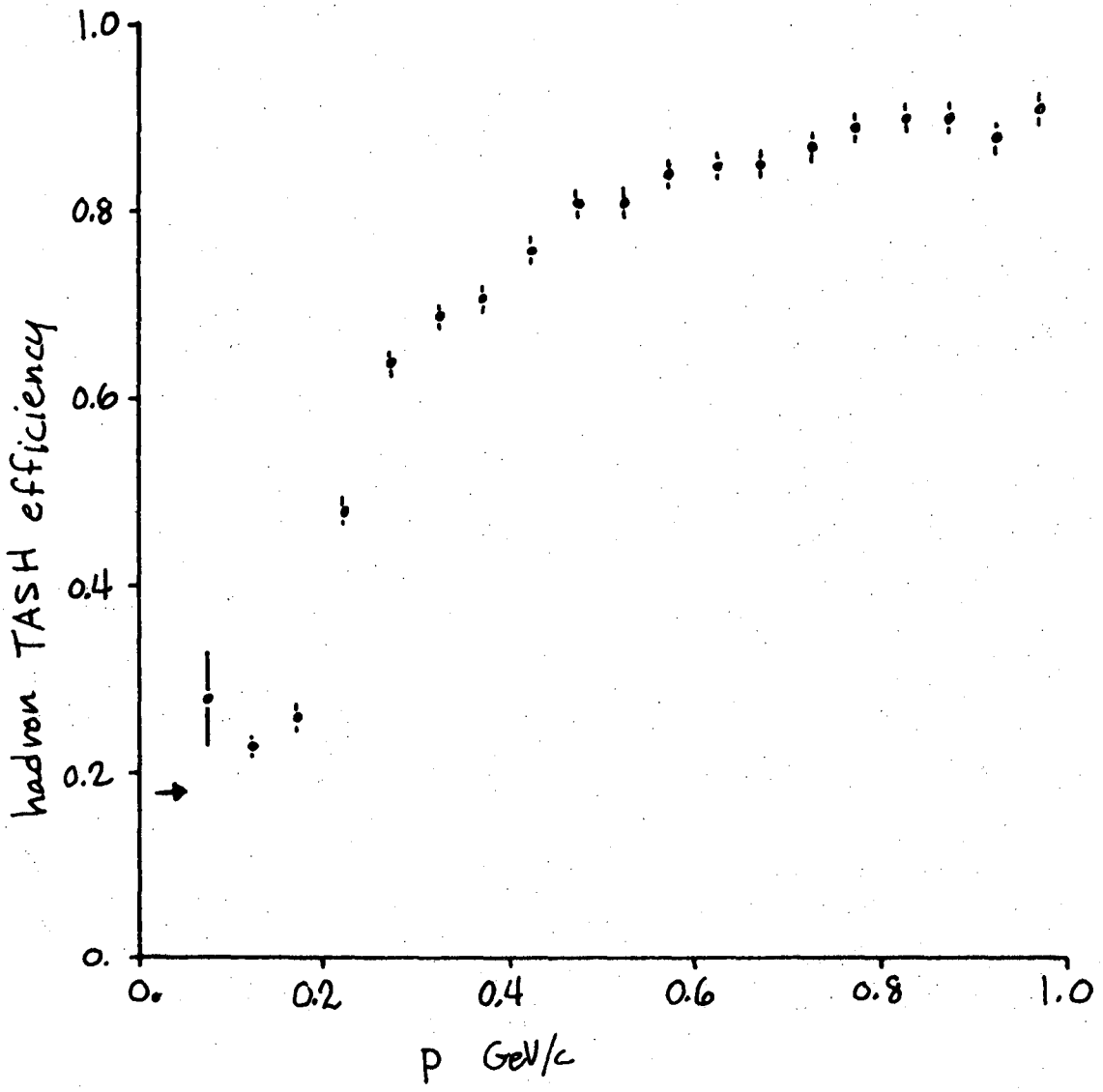

XBL 769-10477

Fig. A4. TASH efficiency for prongs in multiprong events. The arrow indicates the accidental rate.

counters near charged particles have the same "accidental" latch rate. These latches are presumably due to photons from hadron decay, since this accidental rate is negligible in muon-pair events. The TASH efficiency is consistent with the accidental rate for low momentum and rises with momentum as particles gain more penetrating power.

Figure A5 shows the TASH efficiency versus momentum for electrons and positrons in "hadronic" events. The electrons and positrons were identified as part of a conversion pair; a cut of 0.0003 GeV^2 was imposed on the mass-squared of the pair to reduce accidental hadron contamination to $< 10\%$. The TASH efficiency for electrons rises much more rapidly and reaches a slightly higher asymptotic value than for "hadron" prongs, as expected due to the showering of the electrons.

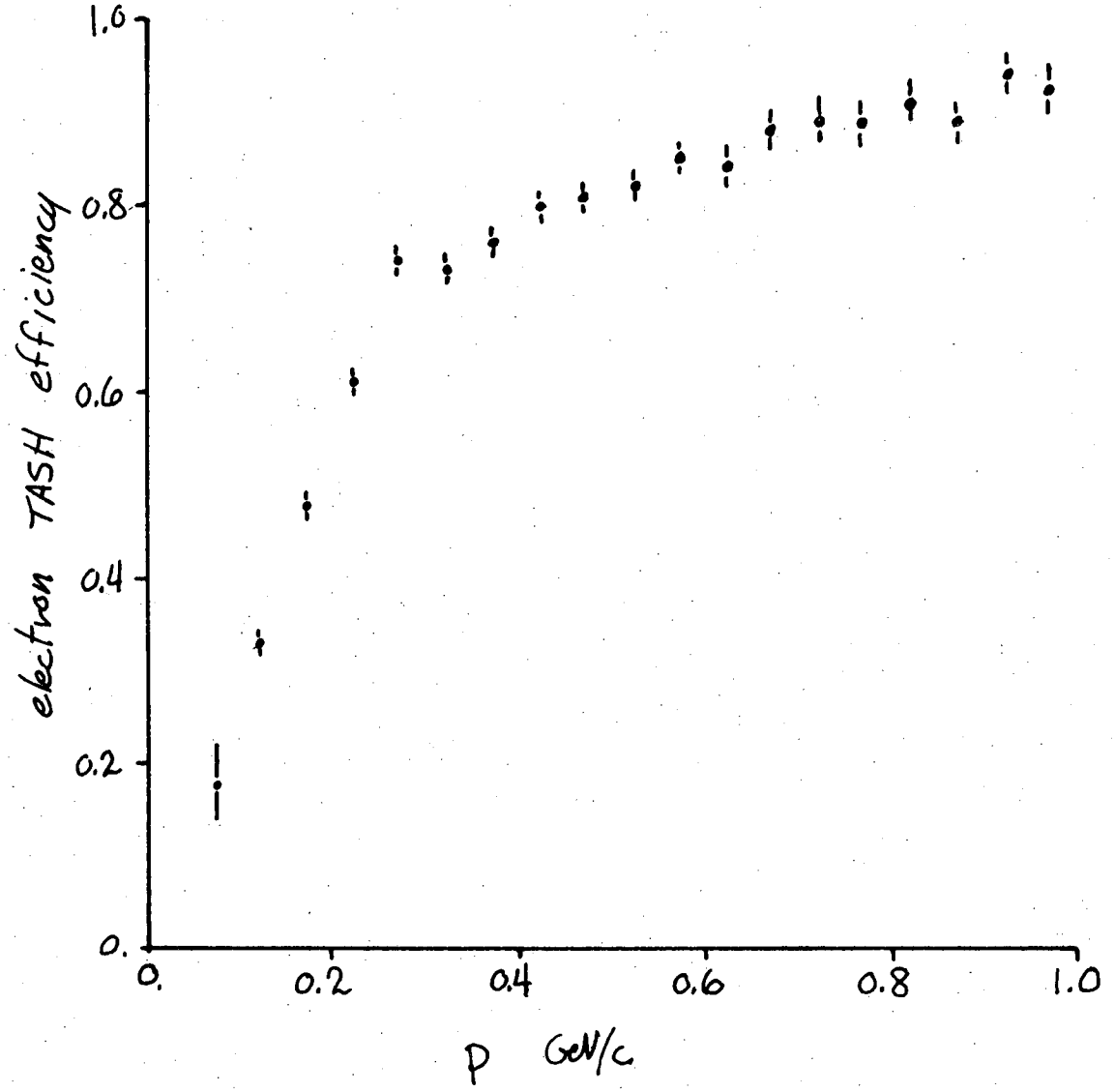

XBL 769-10476

Fig. A5. TASH efficiency for electrons, identified as part of conversion pairs.

REFERENCES AND FOOTNOTES

1. J.-E. Augustin et al., Phys. Rev. Lett. 33, 1406 (1974).
2. J. J. Aubert et al., Phys. Rev. Lett. 33, 1404 (1974).
3. G. S. Abrams et al., Phys. Rev. Lett. 33, 1453 (1974).
4. S. L. Glashow, J. Iliopoulos, L. Miani, Phys. Rev. D2, 1285 (1970).
5. T. Appelquist and H. D. Politzer, Phys. Rev. Lett. 34, 43 (1975).
6. A. De Rújula and S. L. Glashow, Phys. Rev. Lett. 34, 46 (1975).
7. Parallel arguments don't apply for ρ, ω, and φ: the lower masses of the u, d, and s quarks lead to stronger $q\bar{q}$ coupling, invalidating the perturbative approach.
8. T. Appelquist, A. De Rújula, H. D. Politzer, and S. L. Glashow, Phys. Rev. Lett. 34, 365 (1975).
9. E. Eichten et al., Phys. Rev. Lett. 34, 369 (1975).
10. J. Borenstein and R. Shankar, Phys. Rev. Lett. 34, 619 (1975).
11. E. Eichten et al., Phys. Rev. Lett. 36, 500 (1976).
12. H. Harari, SLAC Report SLAC-PUB-1589, unpublished (1974).
13. F. J. Gilman, SLAC Report SLAC-PUB-1600, unpublished (1975).
14. W. Tanenbaum et al., Phys. Rev. Lett. 35, 1323 (1975).
15. R. J. Hollebeek, Ph.D. Thesis, LBL Report LBL-3874 (1975).
16. J. E. Zipse, Ph.D. Thesis, LBL Report LBL-4281 (1975).
17. D. E. Fries, SLAC Report SLAC-99.
18. J.-E. Augustin et al., Phys. Rev. Lett. 34, 764 (1975).
19. G. J. Feldman et al., Phys. Rev. Lett. 35, 821 (1975).
20. These results have been presented in Gerson Goldhaber's paper in the Proceedings of the International Conference on the Production of Particles with New Quantum Numbers (University of Wisconsin, Madison, Wisconsin, 1976) and in Francois Pierre's paper submitted to the XVIIIth International Conference on High Energy Physics, Tbilisi,

USSR, July 15 - 21, 1976.

21. J. H. Hubbell, Photon Cross Sections, Attenuation Coefficients, and Energy Absorption Coefficients from 10 keV to 100 GeV, National Bureau of Standards publication NSRDS-NBS29, August 1969.

22. J. A. Wheeler and W. E. Lamb, Phys. Rev. 55, 858 (1939).

23. W. Heitler, The Quantum Theory of Radiation (Oxford University Press, 1954), p. 259.

24. G. Goldhaber et al., Phys. Rev. 120, 300 (1960).

25. Berger and Seltzer, NASA SP-3012, Table of Energy Losses and Ranges of Electrons and Positrons, p. 55.

26. B. Rossi, High Energy Particles (Prentice-Hall, Inc., New York, 1952), p. 52.

27. H. A. Bethe and W. Heitler, Proc. Roy. Soc. A146, 83 (1934).

28. N. M. Kroll and W. Wada, Phys. Rev. 98, 1355 (1955).

29. D. W. Joseph, Nuovo Cimento XVI, 2021 (1960).

30. M. S. Chanowitz, Phys. Rev. D12, 918 (1975).

31. L. B. Okun and M. B. Voloshin, ITEP-95 (1976).

32. J. W. Simpson et al., Phys. Rev. Lett. 35, 699 (1975).

33. A. Liberman, invited talk in Proceedings of the 1975 International Symposium on Lepton and Photon Interactions at High Energies, W. T. Kirk, editor (Stanford Linear Accelerator Center, Stanford, 1976).

34. D. H. Badke et al., paper submitted to the XVIIIth International Conference on High Energy Physics, Tbilisi, USSR, July 15 - 21, 1976.

35. W. Tanenbaum et al., Phys. Rev. Lett. 35, 1323 (1975).

36. W. Tanenbaum et al., Phys. Rev. Lett. 36, 402 (1976).

37. M. Chanowitz and F. Gilman, to be published in Physics Letters B.

38. B. Wiik and J. Heintze, invited talks in the Proceedings of the 1975 International Symposium on Lepton and Photon Interactions at High

Energies, W. T. Kirk, editor (Stanford Linear Accelerator Center, Stanford, 1976).

39. B. Wiik, Summer Institute on Particle Physics, SLAC, August 1976.

40. B. Jean-Marie et al., Phys. Rev. Lett. 36, 291 (1976).

41. A. M. Boyarski et al., SLAC Report SLAC-PUB-1599, LBL Report LBL-3897 (1975).

TECHNICAL INFORMATION DIVISION
LAWRENCE BERKELEY LABORATORY
UNIVERSITY OF CALIFORNIA
BERKELEY, CALIFORNIA 94720